

Multilayer Photonic Circuits for Efficient Optical Switching

PhD Thesis

Adnan Ghumro

Institute of Photonics

Department of Physics

University of Strathclyde, Glasgow

October 17, 2026

Declaration of Authorship

This thesis is the result of the author's original research. It has been composed by the author and has not been previously submitted for examination which has led to the award of a degree.

The copyright of this thesis belongs to the author under the terms of the United Kingdom Copyright Acts as qualified by University of Strathclyde Regulation 3.50. Due acknowledgement must always be made of the use of any material contained in, or derived from, this thesis.

Signed: AA

Date: 17/10/2026

Abstract

Photonic integrated circuits (PICs) are becoming increasingly important for applications such as optical communications, sensing, and signal processing. However, the continued scaling of PIC technology requires platforms that combine low optical loss, compact device footprints, electro-optic functionality, and compatibility with large-scale manufacturing. Conventional device fabrication methods often rely on etched waveguides, which requires dedicated semiconductor processing tools. This thesis explores alternative fabrication approaches and integration strategies to enable compact and scalable photonic integrated circuits.

First, passive etchless lithium niobate devices based on bound states in the continuum (BICs) were designed, fabricated, and characterised. Ring resonators with bend radii below 100 μm achieved a loaded quality factor of 4.17×10^4 for TM polarisation, with insertion losses as low as $\sim$ 6 dB. These results demonstrate low-loss and compact optical confinement without direct etching of the lithium niobate layer. Second, the etchless lithium niobate platform was extended to realise electro-optic modulators. A compact resonator modulator achieved tuning efficiency of 0.49 pm/V , while a Mach–Zehnder interferometer operating with TE polarisation demonstrated tuning efficiency of 14.69 pm/V. To the best of our knowledge, this represents the first tunable compact resonator based on the BIC principle. Third, heterogeneous integration of GaN membranes on silicon nitride photonic circuits was investigated. This work included the design, fabrication, and characterisation of both GaN and SiN photonic devices, together with the experimental demonstration of transfer printing of GaN membranes onto SiN waveguides. This work identifies the key fabrication challenges associated with the GaN membrane fabrication and establishes a foundation for a future tunable hybrid GaN-on-SiN photonic platform. Finally, inverse-designed polymer vertical couplers were developed to achieve compact optical interconnects with significantly reduced footprints compared with conventional approaches. This work included the design, fabrication, and flip-chip transfer printing of polymer devices. Optical coupling to the bottom waveguide layer was demonstrated, whereas coupling to the top layer was not achieved. The key challenges preventing successful top-layer coupling are discussed.

Acknowledgements

First of all, I would like to sincerely thank my supervisor, Prof. Michael Strain, for providing me with the opportunity to do research under his supervision. His continuous guidance, support, and insightful discussions throughout my PhD have helped me grow as a researcher far beyond the scope of this thesis.

I am also thankful to my industrial supervisor, Loyd McKnight, for his support and for allowing me access to the Fraunhofer facilities whenever required. I would like to thank Dr Jack Smith for his extensive support throughout my PhD journey, from initial training to close collaboration. His knowledge and experience helped me avoid many challenges that would otherwise have taken significant time to resolve. I am also grateful to Dr Benoit Guilhabert and Dr Yunzhou Cheng for sharing their cleanroom expertise, which helped me better understand fabrication challenges. I would like to thank Dr Sean Bommer for his support with flip-chip transfer printing. I also thank all members of IoP for creating a positive and collaborative environment that encouraged growth and support.

I would like to extend my thanks to Ronnie for maintaining the cleanroom facility, which greatly helped in fabricating devices. I also acknowledge the administrative team at IoP, whose efforts ensured that we could focus on research without being overwhelmed by administrative tasks.

I am deeply grateful to my friends and family for their continuous support during difficult times and for cheering my happy moments. I would especially like to thank my parents for allowing me to choose my own path and for their unwavering encouragement; although my father, a medical doctor, had hoped I would follow him into medicine, above all he wanted his children to pursue higher education, and I have worked hard to honour that belief by achieving this doctorate.

Finally, I am extremely thankful to my wife, Aisha Kanwal, for her constant support, trust, and encouragement during the most challenging phases of my PhD. Her belief in me has been a significant source of motivation, and a great deal of credit for this achievement goes to her.

Contents

Declaration of Authorship i

Abstract ii

Acknowledgements iii

List of Figures vi

List of Tables xviii

1 Introduction 1

1.1 Motivation 1

1.2 Electro-optic modulation and material platforms 3

1.2.1 Mathematical description of the electro-optic effect 8

1.3 Heterogeneous and multilayer photonic integration 13

1.4 Thesis organisation 18

2 Passive thin-film lithium niobate devices 20

2.1 Introduction 20

2.2 Fundamentals of optical waveguides and bound states in the continuum 22

2.2.1 Optical waveguides 22

2.3 Bound states in the continuum for photonic waveguides 23

2.4 Optical simulations 25

2.4.1 Simulation software 25

2.4.2 Waveguide geometry 26

2.4.3 Mode profiles . . . 27
2.4.4 FDTD simulation of straight waveguides . . . 29
2.4.5 Bend loss . . . 31
2.4.6 Directional coupler . . . 35
2.4.7 Design finalisation . . . 37
2.4.8 Microfabrication of strip-loaded waveguides . . . 38
2.5 Optical characterisation setup . . . 39
2.6 Straight waveguides . . . 40
2.7 S-bends . . . 43
2.8 Waveguide crossing and four-channel routing device . . . 46
2.9 Mach–Zehnder interferometer . . . 50
2.10 Racetrack resonator . . . 53
2.11 Summary . . . 58

3 Active strip-loaded devices 60
3.1 Introduction . . . 60
3.2 Strip-loaded lithium niobate for EO modulation . . . 63
3.3 Design of strip-loaded devices . . . 65
3.4 Fabrication of active devices . . . 68
3.4.1 Strip-loaded LN metallisation . . . 68
3.5 Electro-optic characterisation . . . 71
3.6 DC tuning . . . 72
3.6.1 Mach–Zehnder interferometer . . . 72
3.6.2 Racetrack resonator . . . 74
3.7 Bandwidth measurements . . . 75
3.8 Summary . . . 78

4 Hybrid integration of GaN and SiN 80
4.1 Introduction . . . 80
4.2 Receiver chip . . . 82
4.2.1 Simulation . . . 82

4.2.2 Fabrication 84
4.3 Donor chip 85
4.3.1 Simulation 85
4.3.2 Design 89
4.3.3 Fabrication of free-standing GaN membranes 91
4.4 Hybrid integration through micro-transfer printing 93
4.4.1 Transfer printing system 93
4.4.2 Transfer printing process 95
4.5 Optical characterisation 97
4.6 Summary 99

5 Inverse-designed polymer devices 101
5.1 Introduction 101
5.2 Inverse design 103
5.2.1 Density-based topology optimisation 104
5.2.2 Adjoint method 106
5.3 Inverse design of polymer devices 107
5.3.1 Bends 108
5.3.2 Multilayer vertical coupler 110
5.4 Chip layout of inverse-designed compact devices 114
5.5 Fabrication of inverse-designed devices 117
5.6 Flip-chip transfer printing of the SU-8 vertical coupler 119
5.7 Optical transmission 121
5.8 Summary 125

6 Conclusion 127
6.1 Future work 129

Bibliography 130

List of Figures

1.1 Moore's law vs the data explosion, 1970–2030. 2

1.2 Schematic representation of a photonic integrated circuit (PIC), illustrating optical signal generation from a laser source, guided propagation through waveguides, wavelength-selective filtering using a ring resonator, electro-optic modulation via a Mach–Zehnder interferometer, and subsequent photodetection for electrical signal output. 3

1.3 Schematic illustration of the electro-optic effect. 4

1.4 Schematic illustration of the Smart-Cut process for LNOI wafers. 6

1.5 Index ellipsoid of an anisotropic material. 10

1.6 Schematic illustration of LN crystal orientation. 11

1.7 (a) Schematic of a heterogeneously integrated GaN-on-SiN photonic platform, where an optical signal propagates in a passive SiN waveguide and interacts with an active GaN region via evanescent coupling. (b) Cross-section of the GaN-on-SiN stack on a SiO_2/Si substrate. 15

1.8 Schematic of the SU-8 fabrication process, illustrating spin-coating, patterning using a direct laser writer (DWL), post-exposure bake (PEB), development, and a final hard bake step to enhance structural stability. 17

1.9 TE mode profile of an SU-8 strip-loaded waveguide on a SiO_2 substrate 1.55 μm. 17

2.1 Strip-loaded BIC waveguide on an etchless lithium niobate platform. . . 24

2.2 Effective index (n_{eff}) of the strip-loaded SU-8-on-LN waveguide modes at $\lambda = 1.55\,\mu$m. (a) Effective index as a function of waveguide width for a fixed SU-8 height of $2\,\mu$m. (b) Effective index as a function of SU-8 height for a fixed waveguide width of $2\,\mu$m. Solid lines represent the TE modes, while dashed lines represent the TM modes. 27

2.3 Mode profiles of modes of strip-loaded waveguides. (a) TE, (b) TE slab mode, (c) TM, and (d) vertical line intensity plot of both polarisation. . 28

2.4 Schematic of the FDTD simulation for a straight waveguide, showing the mode source used to excite the mode and the flux monitor used to measure the transmitted optical power. 30

2.5 Wavelength-dependent propagation loss of straight waveguides with widths from 1.0 to $4.5\,\mu$m (a) TE and (b) TM polarisation, and (c) plots the propagation loss for both polarisations at 1550 nm. 31

2.6 Electric field magnitude of straight waveguides. (a) BIC straight waveguide with width $2.1\,\mu$m (b) non-BIC straight waveguide with width $3\,\mu$m. 31

2.7 Schematic of the FDTD simulation for a circular bend, showing the mode source used to excite the mode and the flux monitor used to measure the transmitted optical power. 32

2.8 Bend loss of a 90° circular waveguide bend. (a) and (b) show the simulated bend loss for a 2 μm waveguide width as a function of bend radius, varied from 40 to 121 μm in 3 μm increments, for the TE and TM polarisations, respectively. (c) and (d) show the corresponding bend loss for a 3 μm waveguide width for the TE and TM polarisations, respectively. 33

2.9 Electric field magnitude distribution of circular bend waveguides. (a) Non-BIC circular bend with a bend radius of $40\,\mu$m. (b) BIC circular bend with a bend radius of $100\,\mu$m. The BIC condition demonstrates significantly lower radiative loss compared to the non-BIC case. 34

2.10 Bend loss of a 90° circular waveguide bend at $\lambda = 1.55\,\mu$m. (a) and (b) show the bend loss for 2 and 3 μm waveguide widths as a function of bend radius for TE and TM polarisation, respectively. Zoomed view of (b) shows the low loss region of TM mode for waveguide widths of 2 and 3 μm. (c) FDE bend loss simulation of TE polarisation for 2 μm waveguide width as a function of bend radius, where bend radius varies from 100 μm to 400 μm. Inset depicts the low–loss region. 35

2.11 Schematic of the FDE simulation for a directional coupler. Each SU-8 waveguide has width and height of 2 μm, separated by a coupling gap of 1 μm. 36

2.12 Power distribution in each waveguide as a function of coupling length L_c, after launching 1 unit of power into waveguide 1, computed using Equation 2.6 for both polarisations. 37

2.13 Fabrication process of passive strip-loaded devices: (a) LNOI sample, 300 nm X-cut, (b) SU-8 resist is spun, (c) waveguides are patterned using photolithography. 38

2.14 Optical microscope images of strip-loaded waveguides: (a) straight waveguides, (b) S-bends, (c) waveguide crossing, (d) directional coupler, (e) racetrack resonator, (f) Mach–Zehnder interferometer, (g) spiral waveguides, and (h) 4-input/4-output optical coupler implemented using waveguide crossing. 39

2.15 Optical transmission setup used for characterisation of waveguides. DUT: device under test; PBS: polarisation beam splitter; BS: beam splitter; PD: photodetector 40

2.16 Measured insertion loss of straight waveguides as a function of wavelength for different waveguide widths: (a) TE polarisation and (b) TM polarisation. 41

2.17 Measured insertion loss spectra of straight waveguides for TE and TM polarisations as a function of wavelength for different waveguide widths: (a) TE, 2 μm; (b) TE, 3 μm; (c) TM, 2 μm; and (d) TM, 3 μm. 42

2.18 Measured insertion loss of S-bends as a function of wavelength for different bend radii: (a) TE polarisation and (b) TM polarisation. 44
2.19 FDE mode simulation of a strip-loaded waveguide with a 3 μm waveguide width and a 94 μm bend radius. (a) TE bend mode in the LN layer. (b) TE bend mode in the SU-8 layer. (c) TM bend mode in the SU-8 layer. 45
2.20 Measured insertion loss spectra of S-bend at $\lambda = 1.55$ μm for different bend radii: (a) TE polarisation (b) TM polarisation. 45
2.21 Schematic of the waveguide crossing with a waveguide width of $W = 2\,\mu$m and a crossing length of $L = 200\,\mu$m. 47
2.22 Measured transmission of the waveguide crossing for light coupled into (a) input 1 and (b) input 2, and (c) the corresponding crosstalk. Data show the mean across n nominally identical devices ($n = 2$ for input 1 and $n = 3$ for input 2), with error bars indicating the standard deviation. 48
2.23 Schematic of the four-port routing device. The waveguide width is $W = 2\,\mu$m. Each directional coupler is defined by a coupling length of $L_c = 80\,\mu$m and a uniform coupling gap of $G = 1\,\mu$m. The waveguide crossing length is $L = 200\,\mu$m, and the bend radius is $R = 350\,\mu$m. 49
2.24 Measured normalised transmission spectra of the 4×4 optical coupler for light coupled into (a) input 1, (b) input 2, (c) input 3 and (d) input 4, showing the response of all four output ports. 49
2.25 Schematic of the unbalanced MZI. The waveguide width is $W = 2\,\mu$m. Each directional coupler is designed with a coupling length of $L_c = 100\,\mu$m and a constant coupling gap of $G = 1\,\mu$m. The horizontal length of the upper arm is $L_{h1} = 2500\,\mu$m, while the lower arm is shortened by 410 μm, giving $L_{h2} = L_{h1} - 410\,\mu$m. The lower arm includes vertical segments of length $L_v = 150\,\mu$m. The bends are implemented with a bend radius of $R = 350\,\mu$m. The upper arm uses a bend angle of $\pi/4$, whereas the lower arm uses a $\pi/2$ bend. These parameters result in a total optical path length difference of $\Delta L = 990\,\mu$m. 51

2.26 Transmission spectra of the Mach–Zehnder interferometer. (a) Measured response at both output ports. (b) Zoomed-in view of the interference fringes for the two ports. 52

2.27 (a) Free spectral range of the MZI. (b) Corresponding group index. Both plots include the fitted straight line. 52

2.28 Schematic of the racetrack resonator. The waveguide width is $W = 2\,\mu$m, straight section lengths are $L_s = 1\,\text{mm}, 1.5\,\text{mm}, 2.5\,\text{mm}$, coupling gap is $G = 0.75\,\mu$m, and coupling length is $L_c = 100\,\mu$m, and the bend radius $R = 94\,\mu$m. 53

2.29 TM-mode transmission of strip-loaded micro-racetrack resonators. (a), (c), and (e) correspond to devices with straight waveguide sections of 1.0 mm, 1.5 mm, and 2.5 mm, respectively. (b), (d), and (f) show the associated fitted resonances at $\lambda = 1588.27\,\text{nm}$, 1588.26 nm, and 1588.25 nm, respectively. Here Q denotes the loaded quality factor and FWHM the full width at half maximum. 55

2.30 TE-mode transmission of strip-loaded micro-racetrack resonators. (a), (c), and (e) correspond to devices with straight waveguide sections of 1.0 mm, 1.5 mm, and 2.5 mm, respectively. (b) and (d) show the fitted resonances of the devices in (a) and (c) at $\lambda = 1588.26\,\text{nm}$ and 1588.27 nm, respectively. Here Q denotes the loaded quality factor and FWHM the full width at half maximum. 57

2.31 FDE mode simulation of a strip-loaded waveguide with a $2\,\mu$m waveguide width and a $94\,\mu$m bend radius. (a) TE bend mode in the LN layer. (b) TE bend mode in the SU-8 layer. 58

3.1 Overview of electro-optic modulation mechanisms and integrated photonic modulator architectures. 61

3.2 Schematic of active strip-loaded devices: (a) MZI and (b) racetrack, where W is the electrode width, G is the electrode gap from the waveguide, L_t and L_b are the lengths of the top and bottom MZI electrodes, respectively, and L is the length of the racetrack electrode. 67
3.3 Fabrication process of active strip-loaded devices (a) LNOI sample, 300 nm X-cut, (b) SU-8 resist is spun, (c) waveguides are patterned using photolithography, and (d) metal deposition. 68
3.4 Schematic of the single layer metal deposition process: (a) spin coating of photoresist on LNOI substrate, (b) photolithography to define and open metal regions, (c) deposition of a 50 nm Ti adhesion layer followed by a 200 nm Au layer, and (d) metal lift-off. 69
3.5 Optical microscope images of MZI electrode at different fabrication stages: (a) electrode openings defined after photolithography, (b) metal deposited within the electrode openings, (c) magnified view of the straight section of the bottom electrodes, (d) magnified view of the straight section of the top electrodes showing metal remaining on top of the waveguide, and (e) enlarged view of the bent sections highlighting metal on the waveguide. 70
3.6 Schematic of the bilayer metal deposition process: (a) spin coating of LOR followed by photoresist on the LNOI substrate, (b) photolithographic patterning of the bilayer resist stack, (c) deposition of a 50 nm Ti adhesion layer followed by a 200 nm Au layer, and (d) metal lift-off. . 71
3.7 Optical microscope images of metal electrodes fabricated using a bilayer lift-off process, illustrating different electrode–waveguide gaps: (a) electrode openings defined after photolithography, where the dark outline around the electrodes corresponds to the resist undercut, (b) metal electrodes deposited on a ring resonator with a 5 μm gap from the waveguide, (c) electrodes on a racetrack resonator with a 4 μm gap, and (d) push–pull electrode configuration with a 4 μm gap on each side of the waveguide. 71

3.8 Optical transmission setup used for characterisation of tunable strip-loaded devices. For electro-optic measurements, 20 MHz function generator was used to supply a sine waveform. PD: photodetector 72
3.9 (a) Transmission spectra of the Mach–Zehnder interferometer under different applied voltages, showing a progressive redshift of the interference fringes. (b) Zoomed view of two adjacent resonances highlighting the wavelength tuning behaviour. 73
3.10 Wavelength shift of the Mach–Zehnder interferometer resonance as a function of the applied DC voltage, showing a linear electro-optic response. The extracted tunability from the linear fit is 14.67 ± 0.64 pm/V. 73
3.11 (a) Transmission spectra of the racetrack resonator under different applied voltages, showing a progressive redshift of the interference fringes. (b) Zoomed view of two adjacent resonances highlighting the wavelength tuning behaviour. 74
3.12 Wavelength shift of the racetrack resonator resonance as a function of the applied DC voltage, showing a linear electro-optic response. The extracted tunability from the linear fit is 0.49 ± 0.01 pm/V. 75
3.13 (a) Electrical 1 kHz sine-wave signal applied to the Mach–Zehnder interferometer and (b) the corresponding optical response. (c) Electrical 5 MHz input signal and (d) the corresponding optical response. 76
3.14 (a) Electrical 1 kHz sine-wave signal applied to the racetrack resonator and (b) the corresponding optical response. (c) Electrical 5 MHz input signal and (d) the corresponding optical response. 77
3.15 Peak-to-peak amplitude response of active strip-loaded devices, normalised to its maximum value. (a) Mach-Zehnder interferometer, (b) Racetrack resonator. PD:Photodetector 78

4.1 Schematic diagram of SiN waveguide, where W is the waveguide width (varied from $1 - 5\,\mu$m) and H is the fixed height of 300 nm. 83

4.2 Mode effective indices for TE and TM polarisations as a function of waveguide width, with the SiN layer thickness fixed at 300 nm. 83
4.3 Fabrication process of SiN waveguides: (a) solvent cleaning of the substrate, (b) spin coating of the photoresist, (c) waveguide patterning and development, and (d) transfer of the pattern into the SiN layer via RIE. Here, W denotes the waveguide width and Δx represents the trench width. 84
4.4 Optical microscope images of fabricated SiN receivers with waveguide widths ranging from 1 to 3 μm, including zoomed-in views of 1 μm and 2 μm waveguides. 85
4.5 Schematic diagrams of the hybrid GaN-on-SiN waveguide structures: (a) fully etched GaN waveguide and (b) partially etched GaN waveguide. The waveguide width W is varied from 0.5 μm to 2 μm for the GaN layer. H_{G} denotes the GaN layer height, H_{A} the aluminium nitride (AlN) layer height, H_{slab} the GaN slab height in partially etched devices, and H_{S} the SiN layer height. 86
4.6 Effective mode index as a function of the GaN waveguide width for the hybrid GaN-on-SiN waveguides shown in Fig. 4.5. The GaN width is varied from 0.5 μm to 2 μm by adjusting the slab thickness. Two SiN waveguide widths are considered: 1.0 μm and 1.5 μm. The left column corresponds to a SiN width of 1.0 μm for the following cases: (a) GaN height of 200 nm with a slab height of 600 nm; (c) GaN and slab heights of 400 nm; (e) GaN height of 600 nm with a slab height of 200 nm; and (g) fully etched GaN down to the AlN layer. The right column shows the corresponding structures for a SiN width of 1.5 μm, labelled as (b), (d), (f), and (h), respectively. 87
4.7 Mode profiles of both TE and TM polarisations for hybrid GaN-on-SiN waveguide at 1550 nm, for SiN waveguide widths of (a, b) 1.0 μm and (c, d) 1.5 μm. 88
4.8 GaN suspended membranes: (a) isolated ring with two anchors, and (b) bus-coupled ring with four anchors. 89

4.9 GDS mask of GaN membranes, highlighting the detailed membrane geometries implemented with two and four anchor supports. 90

4.10 Schematic illustration of the fabrication process for a suspended GaN membrane: (a) GaN-on-silicon sample; (b) SiO_2 deposition followed by resist spin coating; (c) ring pattern definition and RIE; (d) ICP etching of the ring structures; (e) membrane pattern definition and RIE; (f) ICP etching of the membrane layer; and (g) silicon etching, followed by protective silica deposition and KOH under-etching to release the suspended GaN membrane. 92

4.11 Optical microscope images of GaN membrane devices: (a) lithography and RIE of ring device; (b) ICP etching of ring devices; (c) lithography and RIE of the membrane layer; (d) ICP etching of the membrane layer; (e) silica etching; and (f) KOH under-etching resulting in suspended GaN membranes. All scale bars correspond to 50 μm. 93

4.12 Transfer printing setup. 94

4.13 Micro-transfer printing process of a suspended GaN membrane onto a SiN waveguide. 96

4.14 Micro-transfer-printed suspended GaN membrane integrated on a SiN waveguide. (a) Suspended GaN membrane with a bend radius of 60 μm and a waveguide width of 1.6 μm (b) Zoomed-in view of the suspended GaN membrane. 97

4.15 Optical transmission spectra of the SiN waveguide for TE polarisation, measured before and after the transfer printing process. 98

4.16 Evanescent field decay of the SiN bus mode. (a) Mode profile of a 1 μm-wide SiN waveguide at $\lambda = 1550$ nm, with the GaN underside indicated by dashed lines for air gaps of 100, 200, and 300 nm. (b) Normalised field intensity at the GaN membrane as a function of the air gap. 99

5.1 Flowchart illustrating optical device design approaches: (a) forward design; (b) inverse design. 104

5.2 Density-based topology optimisation parametrisation showing (a) the design region, (b) the corresponding pixel grid, and (c) an example density field ρ, where each pixel is assigned a continuous value between air ($\rho = 0$) and core material ($\rho = 1$) before the design converges. 105

5.3 Adjoint-method visualisation of gradient computation. (a) Forward-field intensity $|\mathbf{E}_{\mathrm{fwd}}|^2$ obtained from an FDTD simulation with the source placed at the input port. (b) Adjoint-field intensity $|\mathbf{E}_{\mathrm{adj}}|^2$ from a second FDTD simulation with a virtual source placed at the output monitor. (c) Pixel-wise overlap $\mathrm{Re}[\mathbf{E}_{\mathrm{fwd}} \cdot \mathbf{E}_{\mathrm{adj}}]$ corresponds to the gradient $\partial J/\partial \varepsilon(\mathbf{r})$ at each pixel. 106

5.4 Inverse design process of the compact S-bend: (a) design region, (b) optimised device layout, and (c) simulated electric field distribution of the optimised S-bend. 109

5.5 $|E|$ of the three SU-8 inverse-designed 90° bends at $\lambda = 1.55\,\mu$m: (a) 74 % and (b) 72 % in a 15×15 μm^2 design region; (c) 69 % in a 40×40 μm^2 region. 109

5.6 Schematic of a multilayer SU-8 vertical coupler with the input and Output 1 in the bottom layer, and Output 2 in the top layer. 111

5.7 Finalised mask of multilayer vertical coupler after optimisation. (a) SU-8 bottom layer, (b) SU-8 top layer. 112

5.8 $|E|$ of the multilayer vertical coupler at $\lambda = 1.55\,\mu$m: (a) SU-8 bottom-layer mid-plane ($z = -1\,\mu$m); (b) SU-8 top-layer mid-plane ($z = 1\,\mu$m); (c) $y-z$ cross-section at $x = 25\,\mu$m. 112

5.9 Misalignment tolerance for the vertical coupler in x and y, showing the normalised transmission (dB) of the top and bottom ports versus layer-to-layer offset: (a) x offset and (b) y offset. The dashed horizontal line depicts the -3 dB level. 113

5.10 Normalised transmission (dB) of the top and bottom ports as a function of the interlayer gap between the vertical-coupler layers. The dashed horizontal line depicts the -3 dB level. 114

5.11 (a) GDS layout of inverse-designed SU-8 90° bends; (b) zoomed-in view of 69 % bend; (c) zoomed-in view of 72% bend; and (d) zoomed-in view of 74 % bend. 115
5.12 GDS layout of inverse-designed multilayer vertical couplers: (a) bottom layer chip of the vertical coupler; (b) zoomed-in view of the bottom coupler; (c) top layer chip of the vertical coupler; and (d) zoomed-in view of the top coupler. 115
5.13 Overlay of the top and bottom layers of the multilayer vertical coupler chips. 116
5.14 Optical microscope images of fabricated SU-8 compact bends: (a) 69%, (b) 72% and (c) 74% , with the corresponding zoomed-in images shown in (d), (e) and (f) respectively. 117
5.15 Optical microscope images of the fabricated vertical coupler layers: (a) bottom layer, (b) enlarged view of bottom layer, (c) top layer, and (d) enlarged view of top layer. 118
5.16 Flip-chip transfer printing of the two layer SU-8 vertical coupler. 119
5.17 (a) Optical microscope image of the bonded vertical coupler, (b) E-comb alignment marker, (c) vernier marker with horizontal bars, and (d) vernier marker with vertical bars. 120
5.18 Insertion-loss spectra of the inverse-designed compact bends (best device of each design) and the straight-waveguide reference (mean of five devices, with shaded region indicating the minimum and maximum). . . 121
5.19 Measured bend efficiency of the inverse-designed compact bends (best highlighted). The shaded band spans simulated single-mode transmission (solid) and total flux (dashed). 122
5.20 Measured insertion loss of the transfer-printed multilayer vertical-coupler chip. The shaded region in the waveguide transmission indicates the minimum and maximum insertion loss. 123
5.21 IR image of the multilayer vertical coupler, showing no light at the top port while the bottom port guides the light. 124

List of Tables

1.1 Electro-optic modulator material platforms at a glance. 8

2.1 Optical mode confinement for the fundamental TE_0 and TM_0 modes. . . 29

3.1 Comparison of lithium niobate platforms for electro-optic modulators. . 66

4.1 Optical power confinement in different material layers for the fundamental TE_0 and TM_0 modes of the hybrid GaN-on-SiN waveguides. 89

5.1 Inverse-designed SU-8 90° bends. 110

Dedicated to

My father, Dr Ghulam Rasool Ghumro,
my mother, Farazana Rasool,
and my wife, Aisha Kanwal.

Without your love, encouragement, sacrifices,
and unwavering belief in me, this journey would not have been possible.

With all my love and gratitude.

Chapter 1

Introduction

1.1 Motivation

Over the past decade, the emergence of technologies such as cloud computing, artificial intelligence, sensing, and high-speed communication has led to an exponential growth in data generation [1, 2]. This rapid increase in data traffic demands systems capable of providing high bandwidth and energy-efficient performance. This demand is further intensified by the increasing reliance on data centres and high-performance computing systems, where interconnect bandwidth and energy efficiency are critical limiting factors [3]. However, conventional electronic circuits are approaching fundamental limitations, as the continued scaling predicted by Moore's law becomes increasingly challenging [4]. Modern electronic systems suffer from limited bandwidth, significant resistive losses, and high power consumption, particularly as device dimensions continue to shrink to nanometre scale size [3]. The limitations emerge from transistor scaling, power dissipation, and thermal management have motivated to explore complementary technologies that can overcome these challenges to meet the requirements of modern communication and information processing systems.

To overcome these challenges, photonic integrated circuits (PICs) have emerged as key complementary technology to electronic systems [7, 8]. Instead of replacing integrated electronic circuits, PICs enable high bandwidth, energy-efficient data transfer and signal processing particularly in applications such as interconnects, signal routing, and

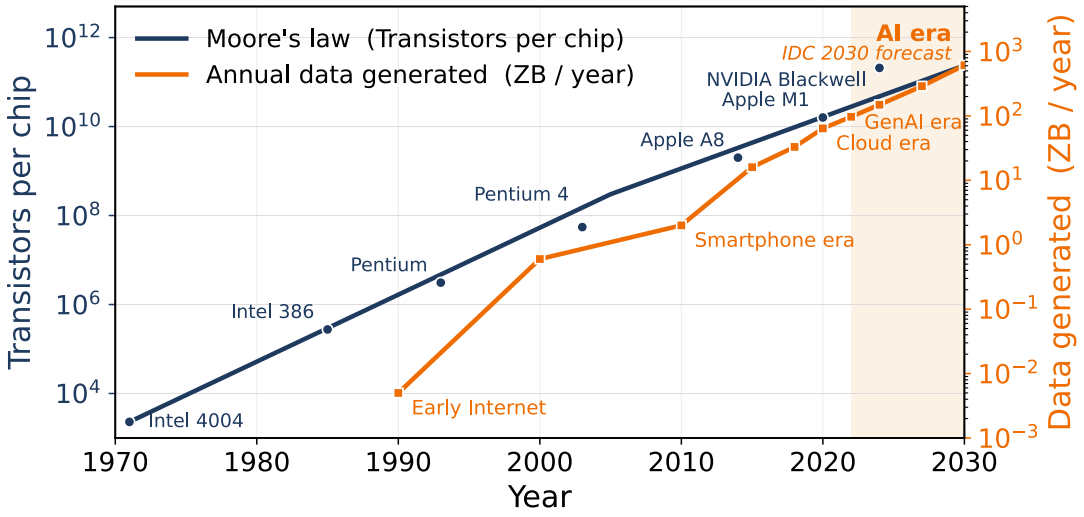

Figure 1.1: Moore's law vs the data explosion, 1970–2030. Transistor count per chip follows Moore's prediction [4] with the compiled trend from [5] and a clear slowdown after the end of Dennard scaling [6]. Annual data generated worldwide combines the historical record [1] with IDC's Global DataSphere forecast [2].

optical computing tasks. In a typical PIC [9], light is generated using lasers and guided through waveguides, which are analogous to electrical wires. Modulators are used to encode information onto optical signals, and filters are used for wavelength selection, while photodetectors convert optical signals back into the electrical domain. Additional components such as splitters and combiners are employed to route within the circuit as shown in Figure 1.2. By integrating these components, PICs enable compact, scalable, and energy-efficient systems with high bandwidth and low propagation losses [10, 11]. As a result, PICs are widely considered as a key technology for applications including optical communication [9, 12], LiDAR [13], optical neural networks [14], optical sensing [15, 16], and quantum information processing [17].

Despite significant progress across a wide range of applications, PICs still face several key challenges that limit their scalability and large scale integration. First, efficient and compact electro-optic (EO) functionality remains challenging. EO modulators are essential components for high-speed signal encoding and switching in photonic circuits; however, platforms that provide strong electro-optic effects often suffer from fabrication complexity or require relatively large device footprints. Second, PICs require multi-

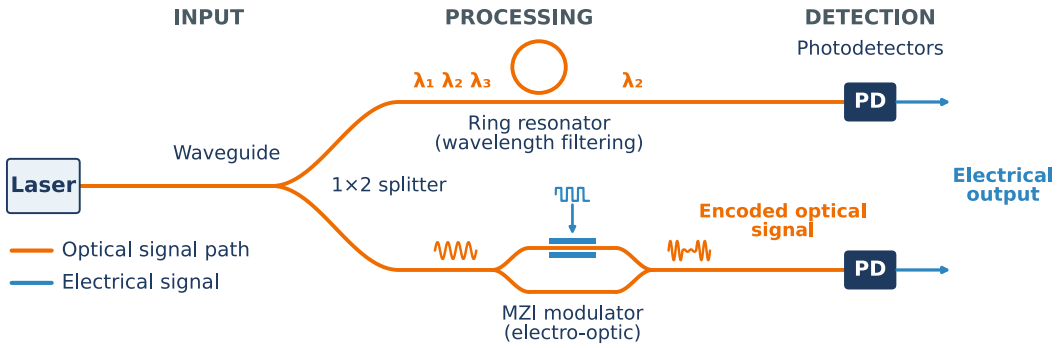

Figure 1.2: Schematic representation of a photonic integrated circuit (PIC), illustrating optical signal generation from a laser source, guided propagation through waveguides, wavelength-selective filtering using a ring resonator, electro-optic modulation via a Mach–Zehnder interferometer, and subsequent photodetection for electrical signal output.

ple functional components to meet the demands of diverse applications. However, no single material platform can provide all required functionalities, making it necessary to explore integration strategies that combine complementary materials. Finally, as data traffic continues to increase, conventional planar PIC architectures are limited in scalability due to routing congestion and restricted integration density. This motivates the need for multilayer photonic architectures, where vertical coupling between stacked waveguide layers enables more efficient routing and higher integration density. These challenges motivate the development of simplified fabrication processes and advanced integration strategies, towards achieving compact and scalable photonic integrated circuits.

1.2 Electro-optic modulation and material platforms

As discussed earlier, electro-optic (EO) devices are fundamental building blocks in integrated photonics. EO modulators and switches are widely used for controlling optical signals in applications such as optical communication [18], microwave photonics [19], programmable photonics [20], optical neural networks [21], and quantum photonic systems [22].

Electro-optic modulation is achieved by applying an electric field to a material, which

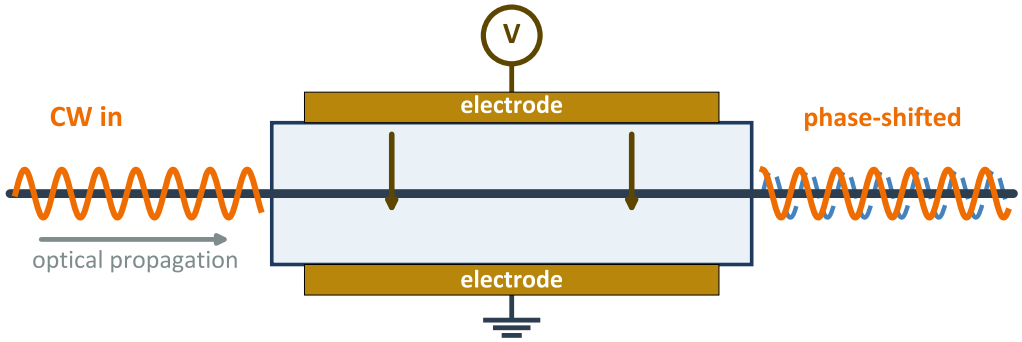

Figure 1.3: Schematic illustration of the electro-optic effect.

induces a change in its refractive index and consequently modifies the phase of the propagating optical signal, as illustrated in Figure 1.3. The underlying physical mechanism of this effect is discussed in more detail in Subsection 1.2.1.

When developing an electro-optic modulator, several key performance metrics must be considered, including modulation efficiency ($V_\pi L$), insertion loss, modulation bandwidth, optical propagation loss, power consumption, device footprint, and fabrication complexity. Optimising these parameters simultaneously remains a major challenge, as improvements in one metric often come at the expense of another. Consequently, significant research effort has focused on developing material platforms and device architectures that provide strong electro-optic interaction while maintaining compact footprints, low optical loss, and scalable fabrication processes. Common device architectures include Mach–Zehnder interferometers (MZIs) and micro-ring resonators [23]. MZI-based modulators typically exhibit large device footprints, but offer broadband operation and high linearity, making them suitable for high-speed applications [24]. In contrast, micro-ring resonators provide compact footprints and enhanced modulation efficiency; however, their operation is inherently narrowband and sensitive to wavelength and temperature variations [25, 26]. Therefore, the choice of architecture depends on which of these requirements is prioritised for the targeted application.

Existing EO modulator platforms exhibit fundamental trade-offs between performance, integration, and fabrication complexity. Silicon photonics is a highly mature platform due to its compatibility with CMOS fabrication and its high refractive index, which

enables dense integration. However, silicon lacks a second-order nonlinearity ($\chi^{(2)}$), limiting its ability to realise intrinsic electro-optic modulation. Consequently, silicon modulators rely on the plasma dispersion effect, which involves carrier injection or depletion to modify the refractive index. While this approach can achieve high-speed modulation [27, 28], it is associated with limited modulation efficiency and increased optical loss.

Organic polymer-based modulators offer large electro-optic coefficients and low driving voltages, making them attractive for compact and high-speed devices [29, 30]. However, their practical implementation is limited by long-term material reliability, thermal instability, and fabrication inconsistency [31]. The electro-optic response relies on molecular alignment (poling), which gradually relaxes over time, leading to performance degradation.

Other platforms, including plasmonic modulators and ferroelectric materials such as barium titanate (BTO), have also been explored. Plasmonic devices enable ultra-compact footprints and very high modulation bandwidths due to strong light–matter interaction, but suffer from high optical losses [32, 33]. BTO offers large electro-optic coefficients and compatibility with silicon integration [34], but challenges related to material quality and fabrication complexity limit its widespread adoption [35].

Among the various electro-optic materials, lithium niobate (LN) has emerged as one of the most promising platforms due to its superior properties that includes strong Pockels coefficient ($r_{33} \sim 31$ pm/V), wide transparency window ($0.4\,\mu$m to $5\,\mu$m), and low optical loss [36]. The development of thin-film lithium niobate on insulator (LNOI) as shown in Figure 1.4, is achieved using the Smart Cut process. A bulk lithium niobate (LN) donor wafer is first implanted with He^+ ions, where the implantation depth defines the thickness of the transferred LN layer. The implanted LN wafer is then bonded to a polished SiO_2 wafer. Following thermal annealing, splitting occurs along the implanted layer, transferring a thin LN film onto the SiO_2 substrate. The transferred film is subsequently planarised using chemical mechanical polishing (CMP) to improve the surface quality and obtain a high-quality LNOI wafer. Commercially available Smart-Cut LNOI wafers are typically supplied with LN film thicknesses rang-

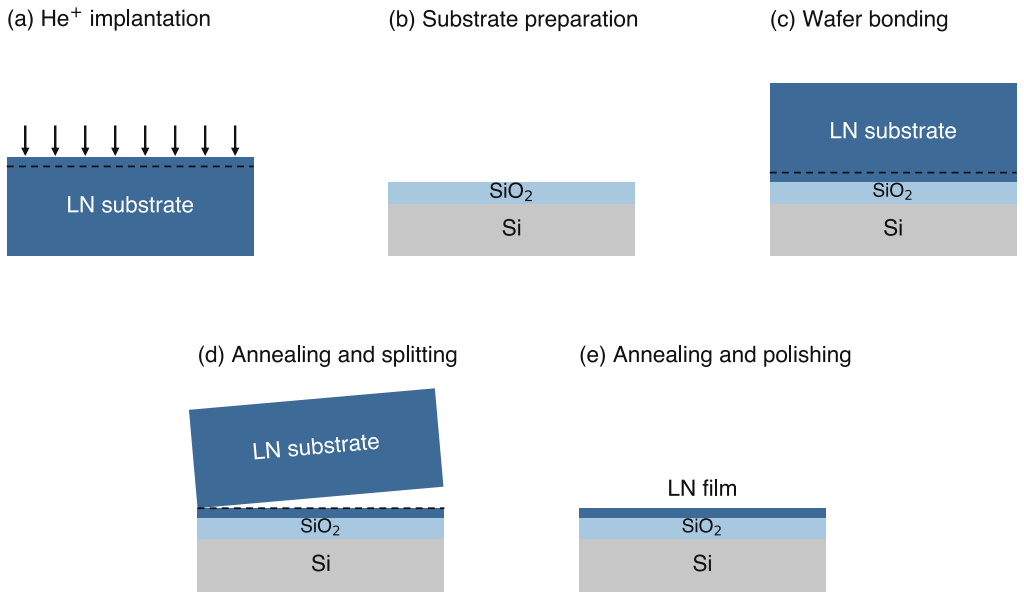

Figure 1.4: Schematic illustration of the Smart-Cut process for LNOI wafers, reproduced from [36].

ing from approximately 300 nm to 900 nm. The LNOI platform enables high refractive index contrast and strong optical confinement, which have facilitated the development of high-performance electro-optic modulators with low driving voltages and high bandwidths [37, 38, 39] .

To realise optical waveguides, the thin-film LN layer must be patterned through etching. ICP-RIE is widely used for the fabrication of LN photonic devices owing to its ability to produce anisotropic and high-resolution features. It combines chemical etching with physical ion bombardment to achieve anisotropic material removal. In an ICP-RIE system, a high-density plasma is generated by an inductively coupled RF source, while a separate RF bias applied to the substrate controls the ion energy. This independent control of plasma density and ion bombardment enables higher etch rates and improved sidewall profiles. However, unlike materials that form volatile chemical etch products, the dry etching of LN relies predominantly on physical sputtering due to the limited formation of volatile reaction products. Consequently, LN etching typically requires Ar^+ plasma in an ICP-RIE system [40]. During this process, LN etching can contaminate the ICP chamber, limiting the use of the equipment for other materials and

reducing compatibility with CMOS fabrication processes [41]. In addition, Ar^+-based etching often results in relatively low etch rates, poor selectivity with respect to lithography resists, and non-vertical sidewalls due to the redeposition of etch by-products such as LiF. Consequently, achieving sufficiently deep etches while maintaining smooth and near-vertical sidewalls remains challenging, with reported sidewall angles typically ranging from 40° to 80° depending on the etch conditions. However, combining Ar with fluorine-based gases can improve the sidewall profile [42], while post-etch wet cleaning can help reduce redeposition, contamination, and overall sidewall roughness [43, 44]. Furthermore, CMP can be employed to further smooth the LN surface and minimise scattering losses [45]. Despite these challenges, low-loss LN waveguides with propagation losses as low as a few dB/m have been demonstrated [46, 47, 48, 49].

As an alternative to dry etching, LNOI can be wet etched using a solution of H_2O_2, NH_4OH, and H_2O mixed in a ratio of 2:2:1 at 85 °C, yielding waveguides with propagation losses of 0.2–0.3 dB/cm. Although this approach is CMOS compatible and offers the potential for higher fabrication throughput and reduced cost, the etching behaviour depends strongly on the crystal orientation of LN, leading to different etch profiles and sidewall angles for different wafer cuts. Furthermore, significant lateral etching can limit dimensional control and produce non-vertical, asymmetric sidewalls [41, 50]. To address some of these challenges, techniques such as transfer printing and heterogeneous integration have been explored to incorporate LN onto silicon and silicon nitride platforms [51, 52, 53]. In some cases, thin-film LN membranes still require etching processes, increasing fabrication complexity. Therefore, there is a need to develop alternative approaches that exploit the electro-optic properties of LN while avoiding complex fabrication steps.

In addition to LN, lithium tantalate (LT) has also emerged as a potential electro-optic material due to its improved resistance to photorefractive effects and more stable operation under high optical power [54, 55]. However, LN remains more widely explored and better established within integrated photonics platforms. For these reasons, LN is selected as the primary electro-optic material system in this thesis.

However, the complexity of the etching process and the need for specialised semicon-

Table 1.1: Electro-optic modulator material platforms at a glance.

Platform	**Key advantage**	**Key limitation**
Silicon [27, 28].	Mature, low-cost CMOS	No Pockels effect
EO polymer [29, 30, 31]	Very high r_{33}, wide BW	Thermal stability, material reliability
BTO [34, 35]	Large Pockels coefficient	Challenging epitaxial growth
Plasmonic [32, 33]	Ultra-compact, THz BW	High losses
Lithium niobate [37, 38, 39]	Strong Pockels effect, high BW, low loss	Challenging fabrication (etching) and cost
Transfer-printed LN [51, 52, 53]	Enables EO on Si/SiN	Alignment/interface loss, integration process complexity
Lithium tantalate [54, 55]	Low DC drift and photorefractive effect	Challenging fabrication; less mature
Etchless LN [56, 57]	Low loss, no etching	Lower optical confinement

ductor processing tools, together with the limitations of existing electro-optic material platforms summarised in Table 1.1, motivate the need for alternative approaches. Etchless techniques, such as strip-loaded waveguides, have been explored to exploit the excellent electro-optic properties of lithium niobate without requiring complex fabrication processes. While these approaches enable low-loss waveguide propagation and simplified fabrication, they typically result in reduced optical confinement and larger device footprints.

In this thesis, these limitations are addressed by combining etchless lithium niobate with bound states in the continuum (BIC) to realise compact and low-loss electro-optic devices. This approach directly addresses the trade-off between fabrication simplicity and device footprint, and is investigated in detail in Chapters 2 and 3.

1.2.1 Mathematical description of the electro-optic effect

The electro-optic (EO) effect describes the modification of the refractive index of a material under an applied electric field. In nonlinear optical media, this phenomenon

arises from the field-dependent polarisation response, which can be expressed as:

$$\mathbf{P} = \varepsilon_0 \left(\chi^{(1)}\mathbf{E} + \chi^{(2)}\mathbf{E}^2 + \chi^{(3)}\mathbf{E}^3 + \cdots \right), \tag{1.1}$$

where $\chi^{(1)}$ is the linear susceptibility, $\chi^{(2)}$ is the second-order non-linear susceptibility, and $\chi^{(3)}$ is the third-order susceptibility. The linear electro-optic (Pockels effect) emerges from the $\chi^{(2)}$ term and occurs only in non-centrosymmetric materials such as lithium niobate [58].

The Pockels effect arises from the same second-order non-linear susceptibility, $\chi^{(2)}$, responsible for other non-linear optical processes such as second-harmonic generation. Specifically, the Pockels effect can be regarded as a special case of the second-order non-linearity in which one of the interacting fields is a slowly varying (DC or RF) electric field rather than a second optical field. In electro-optic materials, this low-frequency limit of the second-order nonlinearity is commonly described using the electro-optic tensor r_{ij}, which relates the applied electric field to the induced change in refractive index. The change in refractive index can be described using the dielectric impermeability tensor $\eta = 1/n^2$:

$$\Delta \left(\frac{1}{n^2} \right)_i = \sum_j r_{ij} E_j, \tag{1.2}$$

where r_{ij} denotes the electro-optic tensor coefficients and E_j is the applied electric field. This linear dependence of refractive index on the applied field is known as the Pockels effect [59].

To further understand the change in refractive index of anisotropic materials, the optical properties can be described using the index ellipsoid [60]:

$$\frac{x^2}{n_x^2} + \frac{y^2}{n_y^2} + \frac{z^2}{n_z^2} = 1. \tag{1.3}$$

When an electric field is present, the coefficients of the ellipsoid are modified according to the electro-optic tensor, resulting in deformation of the ellipsoid and consequently

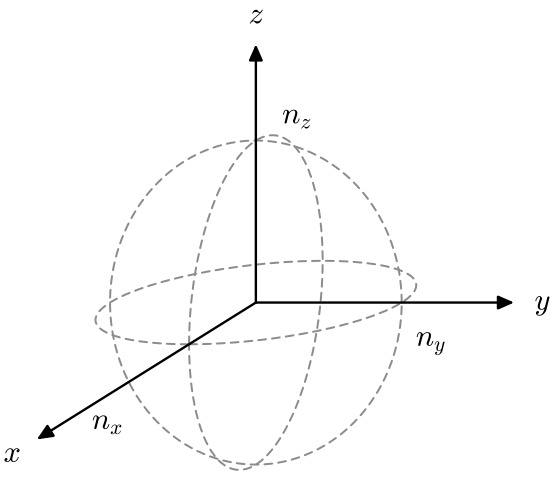

Figure 1.5: Index ellipsoid of an anisotropic material.

altering the principal refractive indices. The change in refractive index is given by:

$$\Delta n = -\frac{1}{2} n^3 r_{ij} E, \tag{1.4}$$

which shows that the refractive index change scales with both the cube of the refractive index and the electro-optic coefficient.

Lithium niobate is a negative uniaxial crystal, with ordinary and extraordinary refractive indices defined as $n_x = n_y = n_o$ and $n_z = n_e$, where $n_e < n_o$. The electro-optic response is anisotropic, and the tensor contains several non-zero components [60], which can be expressed as:

$$r_{\mathrm{LN}} = \begin{pmatrix} 0 & -r_{22} & r_{13} \\ 0 & r_{22} & r_{13} \\ 0 & 0 & r_{33} \\ 0 & r_{51} & 0 \\ r_{51} & 0 & 0 \\ -r_{22} & 0 & 0 \end{pmatrix}, \qquad \begin{aligned} r_{33} &\approx 30.8 \text{ pm/V}, \\ r_{51} &\approx 28 \text{ pm/V}, \\ r_{13} &\approx 8.6 \text{ pm/V}, \\ r_{22} &\approx 3.4 \text{ pm/V}, \end{aligned} \tag{1.5}$$

where the columns correspond to the applied electric field components (E_x, E_y, E_z) in the crystal coordinate system.

In equation (1.5), the electro-optic tensor is explained using contracted Voigt notation, the row index corresponds to the optical polarisation, while the column index represents the direction of the applied electric field . These indices (xx, yy, zz, yz, xz, xy) represent the components of the dielectric impermeability tensor, describing how the refractive index is modified along or between different crystal axes. Therefore, the electro-optic interaction is determined by the specific combination of optical mode polarisation and electric field orientation in the device.

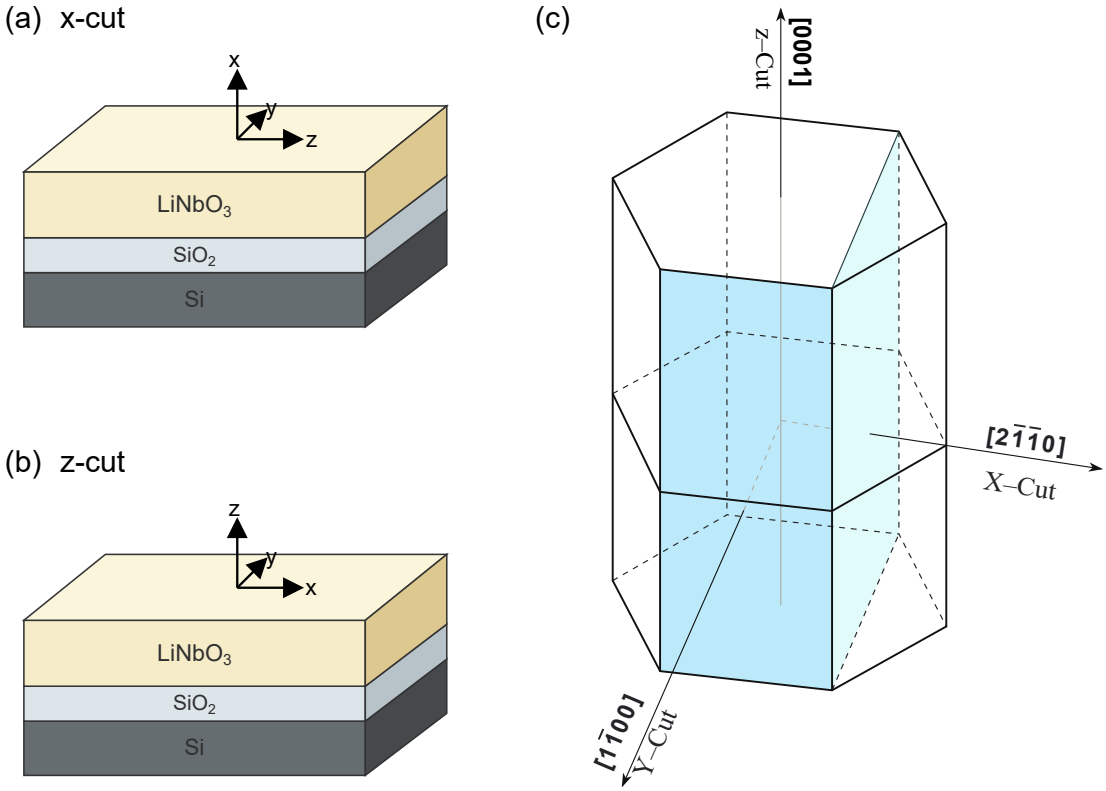

Figure 1.6: Schematic illustration of LN crystal orientation: (a) x-cut and (b) z-cut, indicating the orientation of the crystallographic axes relative to the substrate plane, and (c) hexagonal representation of the LN crystal showing the X-, Y- and Z-cut directions along the $[2\bar{1}\bar{1}0]$, $[1\bar{1}00]$ and [0001] crystallographic axes, respectively. Panel (c) adapted from [61].

Among these coefficients, r_{33} has been used almost exclusively in the literature to realise integrated electro-optic modulators in x-cut lithium niobate. In an x-cut wafer the crystal is cleaved with its surface normal along the crystallographic x-axis, so the lithium niobate film extends in the y–z plane and the optic axis z lies in the wafer plane as

depicted in Figure 1.6(a). Coplanar signal–ground electrodes patterned parallel to the waveguide produce a transverse driving field whose dominant component is E_z [36, 24]. The fundamental TE mode of an in-plane ridge waveguide has its dominant optical electric field along the same z, so the two fields meet on r_{33} and the extraordinary index shifts by $\Delta n_e \approx -\frac{1}{2}\, n_e^3\, r_{33}\, E_z$. The TM mode of the same waveguide instead has its optical field along x, out of the wafer plane; with the same in-plane drive field the dominant tensor element drops to r_{13}, roughly three times smaller, and the modulator pays the corresponding penalty in voltage–length product.

In a z-cut wafer the crystal surface is cleaved normal to the optic axis, so z now points out of the wafer plane while the x- and y-axes lie in-plane as shown in Figure 1.6(b). Similar to the x-cut configuration, z-cut modulators can also exploit the large diagonal electro-optic coefficient r_{33} by applying a strong electric field along the out-of-plane z-direction. TM-polarised modes are typically employed, as their dominant optical electric field component is aligned along the z-axis, enabling efficient interaction through the r_{33} coefficient. This requires electrode configurations capable of generating a strong vertical electric field, where electrodes are positioned either on top of the optical waveguide with ground electrodes placed beside it, or on top of and underneath the waveguide. Such geometries generally increase fabrication complexity compared with conventional coplanar electrode designs. Alternatively, the z-cut configuration can be used to access the off-diagonal coefficient $r_{51} \approx 28$ pm/V, where coplanar electrodes are patterned to apply in-plane electric field along the z-direction change [36, 24]. This field activates the off-diagonal r_{51} electro-optic coefficient, introducing coupling between the x- and z-components of the refractive index. For TM-polarised modes, where the optical field is primarily aligned along the z-axis, this interaction results in a rotation of the index ellipsoid in the x–z plane. Consequently, this leads to polarisation mixing rather than a simple refractive index change. Polarisation mixing arises from coupling between the TE and TM modes due to the rotation of the index ellipsoid [60]. As a result, part of the optical power may be transferred to the orthogonal polarisation state, reducing the effective phase modulation efficiency of the desired mode. The refractive index modulation induced by the electro-optic effect results in a phase shift of an optical wave

propagating along a waveguide (see Figure1.3), which is given by:

$$\Delta\phi = \frac{2\pi}{\lambda}\Delta n\, L, \tag{1.6}$$

where λ is the optical wavelength and L is the electrode length. This phase modulation forms the basis of electro-optic devices such as Mach–Zehnder interferometers and micro-ring resonators, where a voltage-induced phase shift is converted into intensity modulation.

1.3 Heterogeneous and multilayer photonic integration

Etchless lithium niobate combined with BIC enables compact and low-loss electro-optic devices. However, further improvements are required for applications demanding higher integration density and enhanced compactness. As the functionality of photonic integrated circuits continues to increase, the number of required components also grows, making compact and scalable integration increasingly important. To achieve compact electro-optic devices with adequate performance, complementary material platforms and integration approaches are required.

Gallium nitride (GaN) has emerged as a promising candidate for such applications due to its excellent optical and electronic properties. It is a wide bandgap semiconductor that has been extensively used in applications such as blue light-emitting diodes (LEDs) [62], high-power electronics [63], and optoelectronic devices [64], making its fabrication processes relatively well established compared to lithium niobate. GaN also exhibits a wide optical transparency range, spanning approximately $0.365\,\mu$m to $7\,\mu$m, enabling operation from the near-ultraviolet to the mid-infrared regime [65, 66]. In addition, GaN exhibits a second-order non-linear response, with reported electro-optic coefficients of ~ 2 pm/V [67], which although lower than that of lithium niobate, is sufficient for enabling electro-optic functionality in applications where compact integration and moderate EO is required. Furthermore, GaN demonstrates excellent thermal and electrical properties, including high breakdown voltage, high power handling capability, and robustness under high optical power, making it suitable for integrated

photonic applications operating in demanding conditions [68].

However, monolithic GaN waveguides have been demonstrated with propagation losses of a few dB/cm [69, 70], monolithic GaN photonic platform remain limited in scalability due to the high cost of bulk substrates and difficulties in achieving defect-free epitaxial growth. To overcome these limitations, GaN can be integrated heterogeneously with passive photonic platforms, including silicon and silicon nitride, which are widely used for their low optical loss and suitability for high-density photonic integration. Integrating GaN onto these platforms enables the introduction of complementary functionalities, such as electro-optic modulation and optical switching.

While silicon offers high refractive index contrast, it suffers from two-photon absorption and a limited transparency range [27]. In contrast, silicon nitride provides low optical loss, a broad transparency window extending into the visible regime, and negligible non-linear absorption [71, 72]. As a result, monolithic SiN waveguides have become a widely adopted passive photonic platform for low-loss optical routing and non-linear photonic applications [73, 74]. Moreover, for efficient electro-optic interaction, strong optical mode overlap within the GaN layer is essential. Although a monolithic GaN waveguide would maximise the optical mode overlap within the GaN layer, the challenges associated with monolithic GaN photonic platform, discussed above, limit their suitability for large-scale photonic integration. Due to the large refractive index contrast between GaN and silicon, the optical mode remains primarily confined in silicon, leading to weak interaction with GaN. Silicon nitride, with a refractive index closer to that of GaN, enables improved mode overlap and enhanced light–matter interaction. For these reasons, silicon nitride is selected as the passive waveguide platform for heterogeneous integration with GaN in this work as shown in Figure 1.7 enabling the development of compact and multifunctional photonic devices. This highlights the role of heterogeneous integration in overcoming the limitations of individual material platforms and enabling scalable and compact photonic systems.

Although heterogeneous integration complements monolithic material platforms by introducing additional functionalities and enabling new applications, photonic integrated circuits remain fundamentally limited by planar routing constraints. As data traffic

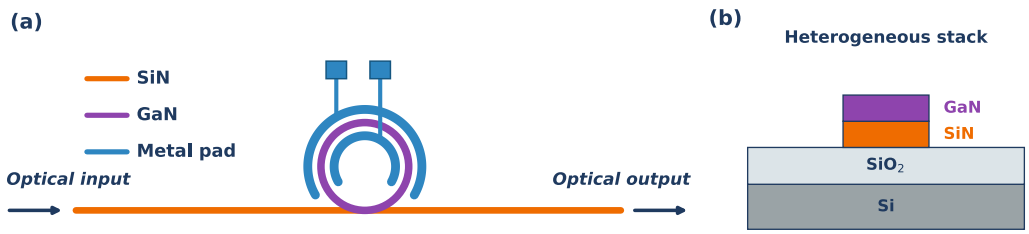

Figure 1.7: (a) Schematic of a heterogeneously integrated GaN-on-SiN photonic platform, where an optical signal propagates in a passive SiN waveguide and interacts with an active GaN region via evanescent coupling. (b) Cross-section of the GaN-on-SiN stack on a SiO_2/Si substrate.

continues to increase, routing congestion becomes a key bottleneck that cannot be efficiently addressed using conventional planar photonic architectures. Multilayer photonic integration has therefore emerged as a promising approach to address these challenges by enabling vertical routing of optical signals across multiple waveguide layers. This approach enhances overall integration density and alleviates routing bottlenecks in complex photonic systems [75, 76].

Existing multilayer photonic approaches have been mainly realised using silicon and silicon nitride platforms. These platforms employ both grating and evanescent coupling structures for interlayer power transfer. Grating couplers use diffraction to couple light out of one layer and into another [77, 78]. However, they are inherently wavelength-sensitive and can support multiple diffraction orders, leading to limited bandwidth and potential cross-talk between layers. In contrast, evanescent coupling enables vertical power transfer through the interaction of overlapping evanescent fields [79, 80, 81]. A common implementation of this approach is the use of adiabatic tapers, which can achieve low-loss coupling through gradual mode evolution between layers. However, such taper structures typically require long interaction lengths, resulting in large device footprints and increasing the overall size of the photonic chip. In addition, these approaches often involve high-temperature processing steps and stringent layer alignment requirements, which limit their scalability and CMOS compatibility.

Polymer photonic platforms offer an attractive alternative for multilayer integration due

to their low cost, fabrication simplicity, low-temperature processing, and compatibility with diverse substrates [82]. Common polymer materials used for photonic applications include polymethyl methacrylate (PMMA), Parylene, and SU-8, each offering distinct advantages and limitations. PMMA is widely used due to its low cost, ease of processing, and compatibility with flexible and scalable platforms. Its propagation losses can reach ~ 4 dB/cm at visible wavelengths [83]. In addition, its relatively low glass transition temperature ($\sim 105°$C) restricts its use in thermally demanding environments [84]. In contrast, Parylene offers a higher refractive index ($n \sim 1.6$–1.63) and improved mechanical stability, with reported propagation losses of 3–6 dB/cm [85], but requires more complex fabrication involving deposition and etching processes [86].

Considering these limitations, SU-8 has emerged as one of the most widely adopted polymer platforms for photonic applications due to its favourable optical, mechanical, and fabrication properties. SU-8 is an epoxy-based negative-tone photoresist that can be patterned using standard lithographic processes without the need for etching or high-temperature processing, enabling a simple and low-cost fabrication process [82]. SU-8 exhibits a refractive index of approximately $n \approx 1.57$ at $1.55\,\mu$m, along with a broad transparency window extending from the visible to the near-infrared region. When combined with a suitable low-index cladding such as air or oxide, it enables efficient light confinement and guiding. Propagation losses are typically in the order of a few dB/cm, making it suitable for short-range interconnects and integrated photonic circuits [87, 88, 89]. The fabrication process and corresponding optical mode profile are illustrated in Figure 1.8 and Figure 1.9, respectively. .

The simplicity of the SU-8 fabrication process significantly reduces both processing time and cost, but due to low index contract SU-8 based devices results in large device footprint which limits the achievable compactness of photonic circuits. To overcome this limitation, inverse design is employed, where computational optimisation algorithms are used to realise compact photonic structures. In this work, inverse design is utilised to develop compact SU-8-based vertical couplers, thereby addressing the large footprint limitations of polymer photonic devices and enabling efficient multilayer integration. This is discussed in detail in Chapter 5.

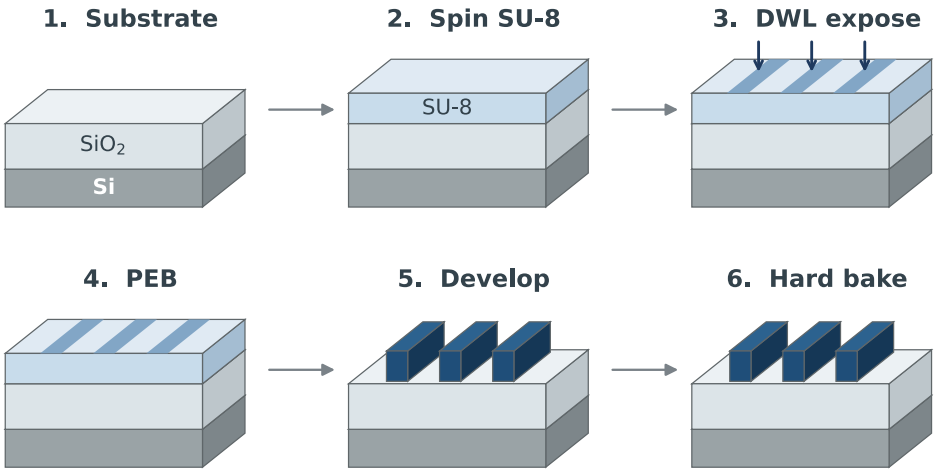

Figure 1.8: Schematic of the SU-8 fabrication process, illustrating spin-coating, patterning using a direct laser writer (DWL), post-exposure bake (PEB), development, and a final hard bake step to enhance structural stability.

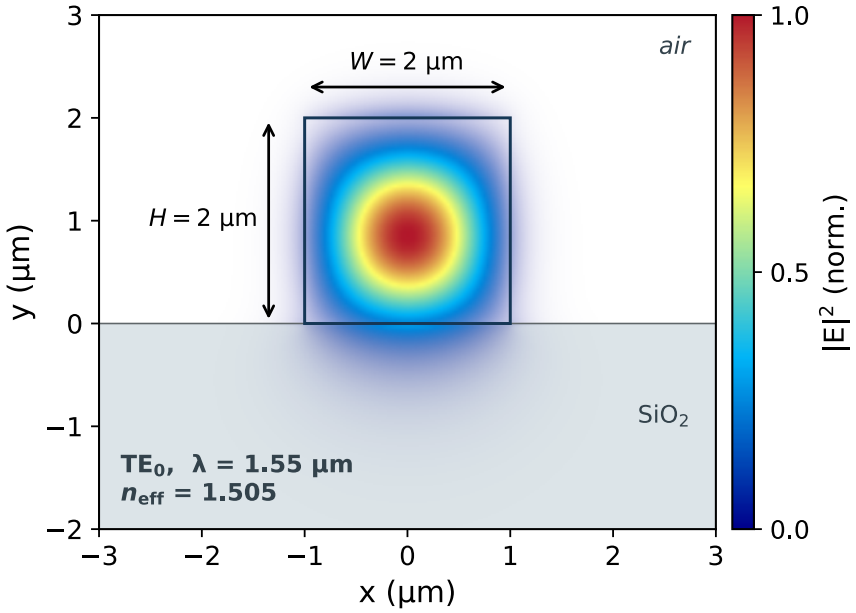

Figure 1.9: TE mode profile of an SU-8 strip-loaded waveguide on a SiO_2 substrate 1.55 μm.

1.4 Thesis organisation

The remainder of this thesis is organised to address key challenges in scalable photonic integration, including fabrication complexity in lithium niobate platforms, heterogeneous material integration, and multilayer routing constraints.

Chapter 2 presents approaches for realising etchless lithium niobate photonic devices. This chapter introduces the underlying theoretical concepts, including bound states in the continuum, and provides detailed optical simulations of waveguide devices. It further presents the fabrication and experimental characterisation of a range of passive devices, including waveguides, bends, waveguide crossing, multi-port couplers, ring resonators, and Mach–Zehnder interferometers.

Building on this, Chapter 3 focuses on active devices based on the etchless lithium niobate platform introduced in Chapter 2. This includes a tunable strip-loaded Mach–Zehnder interferometer exploiting the r_{33} electro-optic coefficient, as well as a compact tunable racetrack resonator based on TM bound-in-continuum modes utilising the r_{13} component. To the best of our knowledge, this work demonstrates one of the most compact active BIC-based tunable resonators reported on a lithium niobate platform. In particular, it also presents the development of both single-layer and bilayer metal deposition strategies for reliable electrode integration on etchless lithium niobate with thick guiding layer such as SU-8.

Chapter 4 explores the heterogeneous integration of GaN membrane resonators with silicon nitride (SiN) waveguides. It presents the design and fabrication of both SiN passive platforms and GaN membranes, and introduces a transfer printing approach for integration of these material systems.

Chapter 5 investigates multilayer photonic integration using polymer-based platforms. In particular, it focuses on the design and realisation of vertical couplers using inverse design techniques. The chapter presents the theoretical background of inverse design, including adjoint optimisation methods, and demonstrates the fabrication and integration of multi-layer SU-8 vertical coupler.

Finally, the thesis concludes with a summary of the key findings and discusses the

broader implications of this work for integrated photonics. Future research directions are also outlined, focusing on advancing compact, etchless, and multilayer photonic integration approaches explored in this thesis.

Chapter 2

Passive thin-film lithium niobate devices

This chapter presents the development of an etchless LN platform for PICs. It details the design, fabrication, and characterisation of a range of passive strip-loaded devices, such as straight waveguides, S-bends, waveguide crossings, directional couplers, race-track resonators, and Mach–Zehnder interferometers. These building blocks establish a robust etchless strip-loaded LN platform suitable for large-scale photonic integration.

2.1 Introduction

Thin-film lithium niobate (TFLN) is increasingly recognised as a prominent platform for integrated photonics, attributed to its exceptional optical properties. These include a broad transparency window ($0.4 - 5\,\mu$m), a high refractive index ($n_o = 2.21$ and $n_e = 2.14$ at 1550 nm), a strong linear electro-optic effect ($\gamma_{33} \sim 31$ pm/V), and a large third-order non-linear optical coefficient, making it suitable for both linear and non-linear applications [90]. Notably, the lithium niobate-on-insulator (LNOI) technology facilitates photonic integration at the sub-micron scale while retaining the primary advantages of bulk lithium niobate. LNOI is undergoing rapid advancements, with recent enhancements in the fabrication of LNOI wafers and low-loss lithium niobate waveguides through plasma etching. Waveguides fabricated using LNOI offer advantages over

those produced via titanium diffusion and proton exchange, which are characterised by large mode size, high bend radius, and lower refractive index contrast [36, 45].

Optical waveguides in LNOI are fabricated through either full or partial etching into the thin film, demonstrating exceptional performance with high-quality factor micro-rings ($> 10^6$) and low propagation loss [46, 48, 49]. However, the material presents challenges in etching, as the fabrication of waveguides necessitates the transfer of a lithographic mask into the lithium niobate material via inductively coupled plasma-reactive ion etching (ICP-RIE). This process requires optimisation for line-edge smoothness to minimise scattering losses [36, 90]. The lithium niobate etching process is generally considered as incompatible with other material platforms that share toolsets due to the risk of process chamber contamination, which can adversely affect subsequent processing [41]. As an alternative to dry etching, wet etching of LN has demonstrated low propagation loss and resonators with Q factors exceeding 10^6, while remaining compatible with CMOS processes. However, it induces lateral etching, which limits dimensional accuracy, and exhibits anisotropic, crystal-orientation-dependent etching, resulting in non-vertical and asymmetric sidewalls [41, 50].

In lieu of etched LN waveguides, several studies have demonstrated the efficacy of strip-loaded waveguiding on the LNOI platform using silicon nitride (SiN) [91, 92, 93, 94, 95], silicon (Si) [96, 97], titanium dioxide (TiO_2) [98, 99], and chalcogenide glass [100]. By patterning dielectric or polymer strips onto the LNOI, optical modes can be guided through effective refractive-index effects, with optical confinement to the LN material being maximised by employing low refractive index strip materials [101]. Although this method is etch-free, strip-loaded waveguides typically exhibit weak guiding, resulting in prohibitive radiative bend losses for radii below a few hundred microns. While this is adequate for long propagation length interferometric modulator geometries, it poses challenges for the production of compact on-chip optical devices.

To address these limitations, bound states in the continuum (BIC) have recently been investigated as a means to enhance optical confinement in dielectric waveguides [57]. BIC modes facilitate strong localisation of light within a waveguide without incurring significant radiation losses, thereby enabling strip-loaded structures to achieve com-

pact devices comparable to fully etched counterparts while maintaining fabrication simplicity, as evidenced by recent demonstrations of micro-resonators and modulators [102, 57, 103]. In this chapter, an overview of optical waveguiding using BICs is discussed, together with the simulation, fabrication, and experimental characterisation of strip-loaded waveguides. The devices developed in this work are fabricated on X-cut lithium niobate with a thickness of 300 nm, enabling the implementation of fully etchless strip-loaded waveguides on the lithium niobate platform.

2.2 Fundamentals of optical waveguides and bound states in the continuum

2.2.1 Optical waveguides

Planar waveguides are analogous to optical fibres and consist of a high refractive index core surrounded by a lower refractive index cladding. The optical confinement within the waveguide is determined by the refractive index contrast, $\Delta n = n_{\text{core}} - n_{\text{clad}}$, where a higher contrast leads of stronger confinement. Such waveguides support guided modes, which are solutions to Maxwell's equations. The wave equation for the electric field, derived from Maxwell's equations, is given by:

$$\nabla^2 \mathbf{E} + k_0^2 n^2(x, y)\mathbf{E} = \beta^2 \mathbf{E}, \tag{2.1}$$

where $k_0 = 2\pi/\lambda$ is the free-space wave number, $n(x, y)$ is the refractive index distribution, and β is the propagation constant. The effective refractive index of a mode is defined as

$$n_{\text{eff}} = \frac{\beta}{k_0}, \tag{2.2}$$

which must satisfy $n_{\text{clad}} < n_{\text{eff}} < n_{\text{core}}$. A waveguide can support multiple guided modes satisfying $k_0 n_{\text{clad}} < \beta < k_0 n_{\text{core}}$. When $\beta < k_0 n_{\text{clad}}$, the optical field is no longer confined by total internal reflection and becomes a radiation mode.

2.3 Bound states in the continuum for photonic waveguides

The concept of BICs originates from quantum mechanics and was first introduced by von Neumann and Wigner in 1929 [104]. They demonstrated that localised eigenstates can exist within the radiation continuum while remaining perfectly confined. In photonics, a BIC refers to an optical mode that lies within the radiation continuum yet does not radiate due to symmetry protection or destructive interference. Such states enable ultra low-loss confinement and extremely high quality factors, which have made them attractive for integrated photonic applications [105]. In PICs, BICs can be realised by patterning a low-refractive-index waveguide on a high-refractive-index substrate [57, 102]. This approach is particularly valuable for materials such as lithium niobate and diamond, which are difficult to etch and often suffer from scattering losses caused by sidewall roughness [102]. By avoiding etching of the high-index film and instead patterning only a low-index polymer layer, the supported optical mode remains confined within the high-index substrate region beneath the guiding layer, allowing low-loss optical guiding while preserving the full advantages of the material platform.
Consider a strip of low-index polymer with width W deposited on a high-index substrate such as lithium niobate, as illustrated in Figure 2.1. According to conventional wisdom, light guided by such a polymer strip should strongly leak into the substrate continuum. However, a BIC can be engineered so that the radiation leakage cancels, transforming a leaky mode into a lossless guided mode. In this structure, the substrate supports a continuum of TE modes, and the TM bound mode supported by the polymer waveguide can couple to these TE continuum channels. The leakage occurs at both edges of the waveguide, where the TM mode couples into right-propagating (channels 2 and 4) and left-propagating (channels 1 and 3) TE continuum modes. If the leakage contributions through channels 1 and 3 cancel by destructive interference and simultaneously those through channels 2 and 4 cancel, then the net coupling of the TM bound mode to the continuum becomes zero. This yields a lossless TM mode corresponding to the BIC condition. The destructive interference depends on the phase

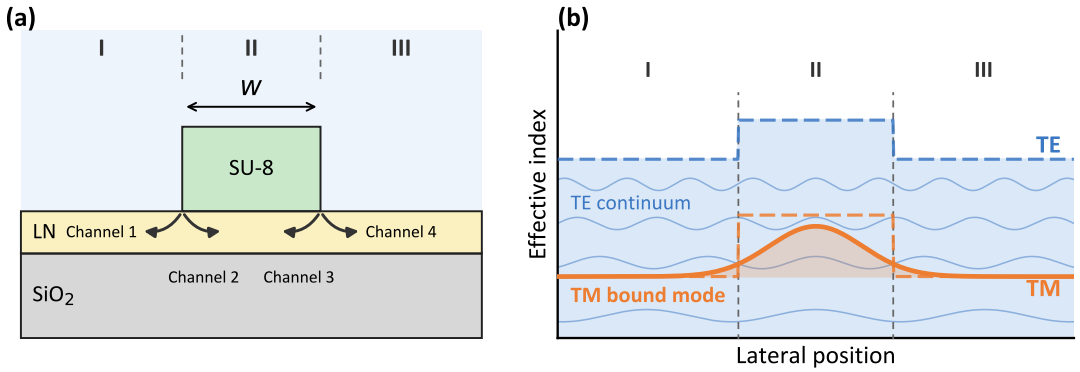

Figure 2.1: Strip-loaded BIC waveguide on an etchless lithium-niobate platform. (a) SU-8 strip of width W on LN slab. Regions I and III correspond to the bare LN slab, while region II denotes the strip-loaded section. Channels 1–4 represent TE radiation channels. (b) Effective-index distribution showing a guided TE mode (blue) and a TM bound mode (orange) embedded in the TE continuum. Adapted from [106].

difference accumulated across the waveguide width, and therefore the BIC condition for straight waveguides can be obtained by optimising waveguide width, W [106]. For a straight waveguide, the propagation length L (or equivalently, the inverse propagation loss) of the TM bound mode as a function of waveguide width can be expressed using Equation 2.3:

$$L \propto \frac{W^2}{\sin^2\left(\frac{k_y W}{2}\right)} \tag{2.3}$$

where k_y is the transverse wave-vector component of the TE continuum mode that is phase-matched to the TM bound mode. The BIC occurs at the zeros of the sine term, where destructive interference eliminates radiation loss, yielding theoretically infinite propagation length. This distinguishes a BIC from a conventionally guided mode. A guided TE mode is confined in the LN slab beneath the SU-8 strip by effective-index guiding and, lying above the TE slab continuum, cannot couple to radiation modes. The TM mode, in contrast, lies within the TE continuum and can therefore radiate into TE slab modes. Although increasing the waveguide width reduces this radiation loss, it does not eliminate it and eventually results in a multimode waveguide. At the BIC condition, the radiation leakage is instead cancelled completely by destructive interference at a specific width, enabling lossless guiding in strip-loaded waveguides. In

this work, the TM mode was used to form the BIC. TE BICs have also been reported, but they require more complex multilayer structures, such as two coupled waveguide layers in which the BIC condition is sensitive to the separation between the layers [107], or an etched Si_3N_4 waveguide combined with a bonded $LiNbO_3$ layer [108]. The TM BIC was therefore chosen because it requires only a single patterned polymer layer on an unetched LN slab.

For bent waveguides, the leakage of the TM mode depends not only on the width W but also on the bend radius R. A practical design strategy is to first determine the low-loss width for straight sections and then adjust the bend radius to achieve the BIC condition in curved regions to realise high-Q racetrack or ring resonators without etching the LN substrate. This enables ultra low-loss integrated photonic components while fully leveraging the electro-optic, non-linear, and piezoelectric properties of LN.

2.4 Optical simulations

2.4.1 Simulation software

Numerical simulations were carried out using Tidy3D, a cloud-based electromagnetic solver that leverages graphical processing unit (GPU) acceleration to efficiently perform computationally intensive calculations [109]. Both the finite-difference eigenmode (FDE) and finite-difference time-domain (FDTD) solvers were employed for the simulations presented in this work. The FDE solver is a fully vectorial Maxwell's equations solver based on the method of Zhu and Brown [110]. In this approach, the cross section of the optical waveguide is discretised into a mesh, and Maxwell's equations are solved in the frequency domain to obtain the guided modes. The FDE method provides the spatial mode profiles, effective refractive indices, and associated losses of the waveguide modes. Alternatively, the FDTD method is a comprehensive three-dimensional, full-wave electromagnetic solver extensively used for modelling complex materials and optical structures [111]. This method discretises the simulation domain into a spatial and temporal grid, solving Maxwell's equations at each grid point over time. As a time-domain technique, FDTD facilitates broadband analysis and enables precise modelling

of arbitrarily shaped, dispersive, and sub-wavelength structures. These attributes make it well-suited for the simulation of photonic integrated devices with high index contrast and intricate geometries.

2.4.2 Waveguide geometry

The FDE simulations were carried out for strip-loaded waveguides. Figure 2.1(a) illustrates the waveguide's geometry, where the SU-8 polymer has a height of $2\,\mu$m on a 300 nm thick layer of LNOI. These simulations utilised the frequency-dependent refractive index data for LN [112], SiO_2, and SU-8, and were performed at a wavelength of $1.55\,\mu$m, corresponding to the central wavelength of most experimentally measured transmission sweeps, where the refractive indices were $n \approx 2.21$ for LN, $n \approx 1.44$ for SiO_2, and $n \approx 1.57$ for SU-8. The thickness of the LN and the height of the SU-8 polymer were kept constant, while the waveguide width was varied from $1 - 5\,\mu$m. As the width of the waveguide increases, it can accommodate more modes. Figure 2.2(a) presents the effective refractive index of the waveguide as a function of its width, with solid lines indicating TE modes and dashed lines representing TM modes. Since strip-loaded waveguides adhere to the effective index guiding principle, the polymer's height is not a significant factor, once it exceeds $1\,\mu$m, where the effective index saturates as shown in Figure 2.2(b). This occurs because the optical field decays evanescently within the SU-8 layer, so additional polymer height beyond $1\,\mu$m has a negligible effect on the modal effective index. Therefore, a height of $2\,\mu$m was used for all simulations. Notably, the effective indices of TM modes are considerably lower compared to TE modes, indicating that TM modes are less confined. The waveguide width is treated as a variable parameter and should be selected to be greater than the resolution limit of the lithography method used for waveguide fabrication. A waveguide width of $2\,\mu$m can easily support a single TE mode and TM mode. However, other modes are also present, which have an effective refractive index close to that of the slab, where the mode is guided in the slab, resulting in poor confinement and high substrate leakage losses.

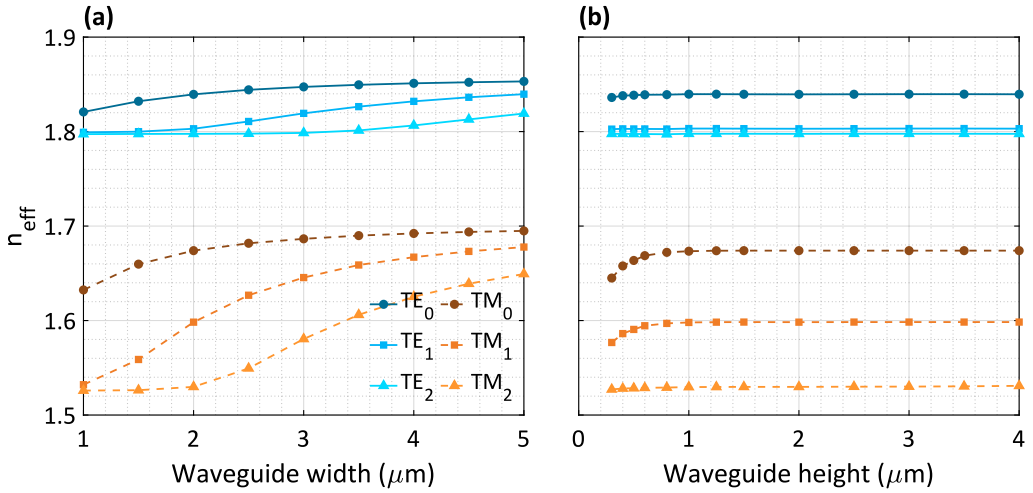

Figure 2.2: Effective index (n_{eff}) of the strip-loaded SU-8-on-LN waveguide modes at $\lambda = 1.55\,\mu$m. (a) Effective index as a function of waveguide width for a fixed SU-8 height of $2\,\mu$m. (b) Effective index as a function of SU-8 height for a fixed waveguide width of $2\,\mu$m. Solid lines represent the TE modes, while dashed lines represent the TM modes.

2.4.3 Mode profiles

The mode profiles for both polarisations supported by strip-loaded waveguides are illustrated in Figure 2.3. The effective refractive index for TE polarisation is comparatively higher than that for TM polarisation. The strip-loaded geometry also supports slab TE modes as shown in Figure 2.3(b). The electric field intensity is concentrated in the higher index layer, LN, and partially extends into lower regions. Additionally, the electric field components remain parallel to the substrate, enabling TE to achieve stronger mode confinement in the LN layer. Conversely, the TM effective index is lower than that of the fundamental TE mode because the TM mode lies below the TE continuum supported by the LN layer, Figure2.3(b) show an slab TE mode. As discussed in the previous section, destructive interference among radiation channels (Slab TE modes) at the waveguide edge can suppress radiation leakage, resulting in a TM bound mode for specific waveguide widths, where phase matching among radiation channels leads to negligible loss. The dominant electric field component of the TM bound mode has a vertical orientation, resulting in weaker confinement in the LN layer, with the tail extending into the adjacent polymer and substrate region. TE polarisation experi-

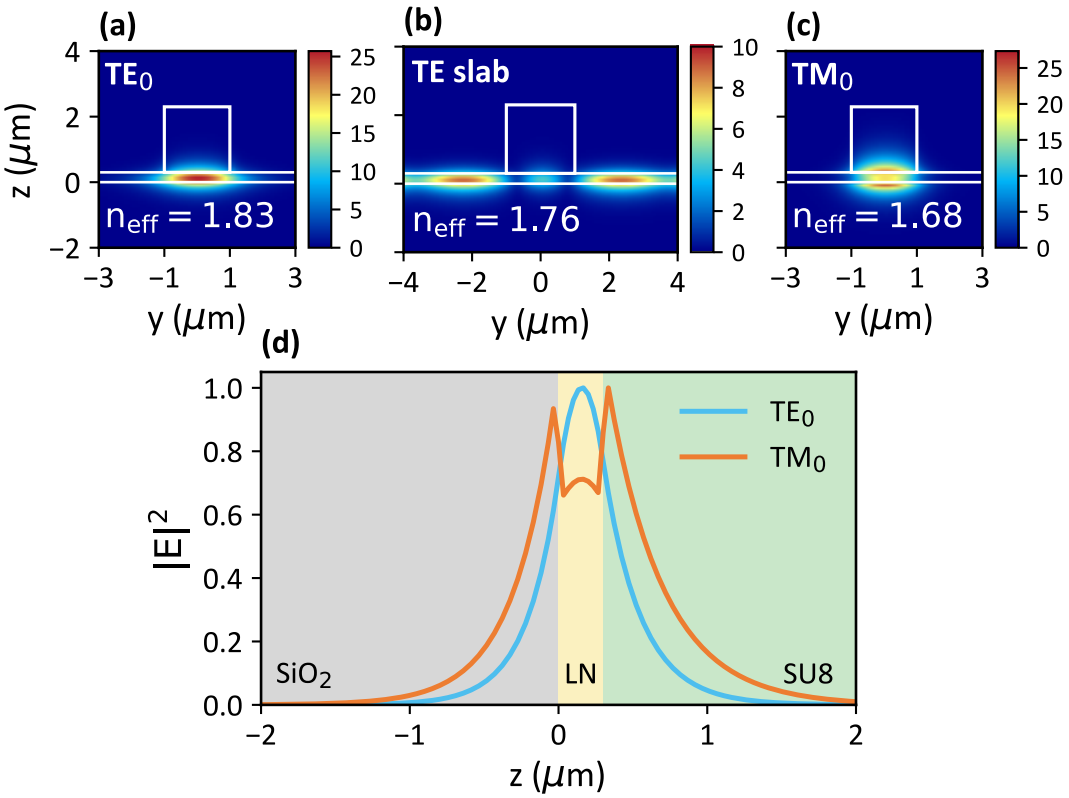

Figure 2.3: Mode profiles of modes of strip-loaded waveguides. (a) TE, (b) TE slab mode, (c) TM, and (d) vertical line intensity plot of both polarisation.

ences $\sim 53\%$ confinement in the LN layer, while TM exhibits $\sim 30\%$ confinement, as summarised in Table 2.1. The mode confinement factor, Γ, is defined as

$$\Gamma = \frac{\iint_{\text{LN}} |E|^2 \, dA}{\iint_{\text{total}} |E|^2 \, dA} \times 100\%. \tag{2.4}$$

where the numerator represents the integrated electric field intensity within the LN region and the denominator represents the total integrated field intensity across the simulation domain. For electro-optic modulation, confinement in the LN layer plays an important role in achieving low-voltage operation. However, TE uses the r_{33} tensor component, resulting in a stronger electro-optic effect, whereas TM relies on the weaker r_{13} component for X-cut LN, as discussed in the previous chapter

Table 2.1: Optical mode confinement for the fundamental TE_0 and TM_0 modes.

Mode	SiO_2 (%)	LN (%)	SU-8 (%)
TE_0	20.84	52.97	26.18
TM_0	29.45	29.96	40.51

2.4.4 FDTD simulation of straight waveguides

The FDTD simulations were conducted to determine the loss in a strip-loaded straight waveguide. Figure 2.4 illustrates the schematic of the FDTD simulation for the straight waveguide, where a 2 μm thick SU-8 layer on a 300 nm thick LN substrate was used, similar to the FDE simulation setup. The same frequency-dependent refractive index data for LN, SiO_2, and SU-8 were used, ensuring that material dispersion was included across the simulated wavelength range. The waveguide widths were adjusted from 1 to 4.5 μm in increments of 100 nm. Perfectly matched layer (PML) absorbing boundary conditions comprising 12 layers were applied on all sides of the simulation region to minimise reflections and accurately capture propagation losses. A Gaussian pulse mode source was used to excite the mode, with TE and TM polarisations simulated separately. The excited mode propagated along the waveguide, and a flux monitor positioned at the opposite end was used to measure the power of the propagating mode. The propagation loss of the waveguide was calculated using Equation 2.5, where P_{in} represents the input power recorded by the mode monitor, and P_{out} denotes the transmitted power measured by the flux monitor.

$$\text{Loss (dB)} = -10 \log_{10} \left(\frac{P_{\text{out}}}{P_{\text{in}}} \right) \tag{2.5}$$

The Figure 2.5 depicts the loss of strip-loaded straight waveguide for both TE and TM polarisation. The propagation loss is calculated using Equation 2.5. The polarisation loss increases gradually with waveguide width, though the absolute loss remains low. By contrast, the TM mode exhibits sharp reductions in loss at specific widths, corresponding to conditions where the TM mode transitions into a bound state by decoupling from the TE continuum as shown in Fig. 2.5(b). This phenomenon corresponds to the formation of a BIC. Wider waveguides exhibit low TM loss due to weak coupling to

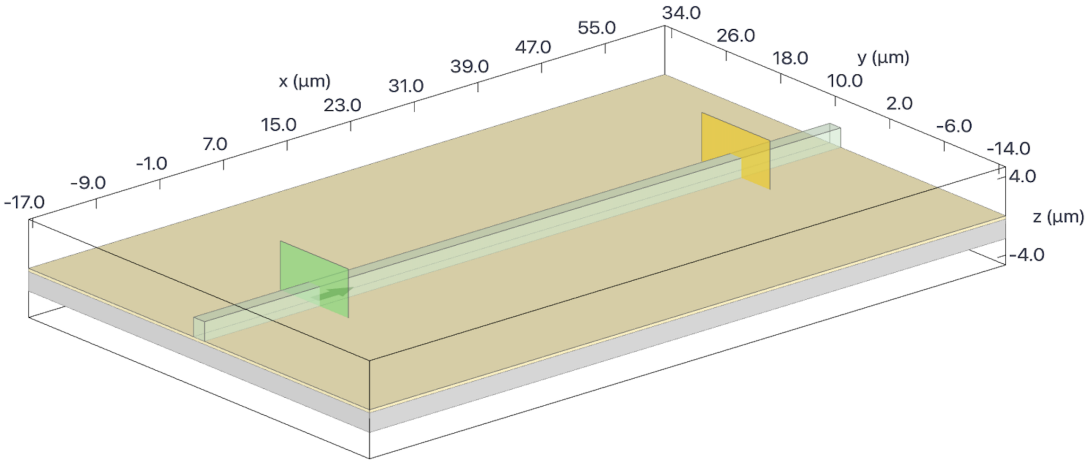

Figure 2.4: Schematic of the FDTD simulation for a straight waveguide, showing the mode source used to excite the mode and the flux monitor used to measure the transmitted optical power.

the TE continuum [57]. However, this comes at the cost of looser optical confinement, with the mode spread over a larger area, and support for higher-order modes. The Figure 2.5(c) presents the loss for TE and TM at 1550 nm, TE losses remain < 1 dB/cm for all simulated widths, but the TM mode has low loss at ~ 2 and $4\,\mu$m waveguide widths, corresponding to the BIC condition. Importantly, the tolerance for maintaining low loss, on the order of 2 dB/cm, spans nearly 400 nm which is readily attainable with standard nanofabrication processes. Figure 2.6 shows the simulated electric field magnitudes of the TM mode in a straight waveguide at two different widths. At a waveguide width of $2.1\,\mu$m, where the BIC condition is satisfied, the leakage into the TE continuum is cancelled, so the light remains confined within the waveguide with no observable radiation, resulting in low loss. In contrast, at a width of $3\,\mu$m, where the BIC condition is not satisfied, significant field leakage into the surrounding slab is observed, resulting in increased loss. The optical loss in straight waveguides has contributions from scattering and radiation losses resulting from mode overlap of the guided modes with the sidewall roughness of the SU-8 rib structure, in addition to the coupling between the bound guided mode and the continuum of radiative modes in BIC guiding conditions [57]

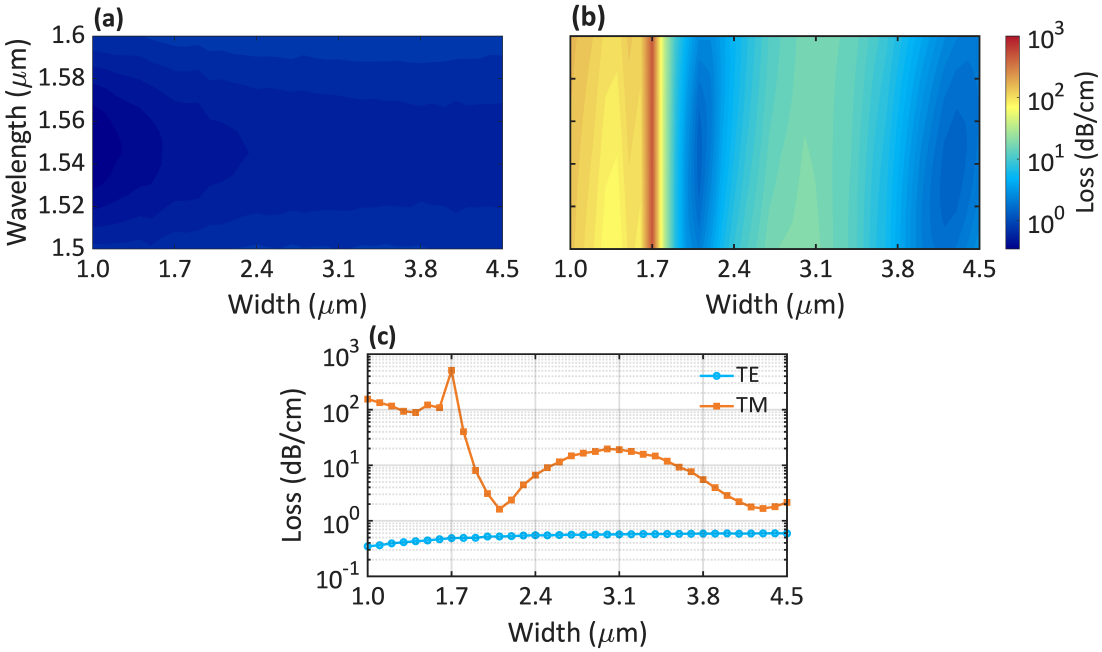

Figure 2.5: Wavelength-dependent propagation loss of straight waveguides with widths from 1.0 to 4.5 μm (a) TE and (b) TM polarisation, and (c) plots the propagation loss for both polarisations at 1550 nm.

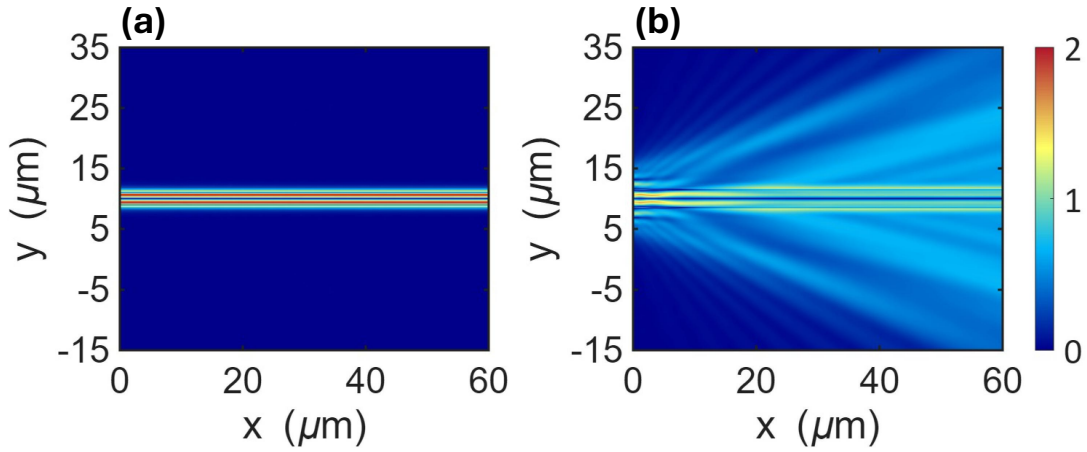

Figure 2.6: Electric field magnitude of straight waveguides. (a) BIC straight waveguide with width 2.1 μm (b) non-BIC straight waveguide with width 3 μm.

2.4.5 Bend loss

The bend loss FDTD simulation for strip-loaded waveguides was conducted in a similar way to straight waveguides, and the schematic of the simulation is shown in Figure 2.7.

Waveguide widths of 2 and 3 μm were used for both TE and TM polarisations. The 2 μm width was selected based on the straight waveguide analysis presented in above section, where the BIC condition satisfied at 2.1 μm; however, the low-loss region spans a broad tolerance ($\sim$ 400 nm), and 2 μm lies well within this range. In contrast, the 3 μm width corresponds to non-BIC condition, where increased coupling to TE continuum results in higher propagation loss, and is therefore used as a reference to highlight the impact of BIC-guided confinement. The bend radius was varied from 40 μm to 121 μm with a step size of 3 μm.

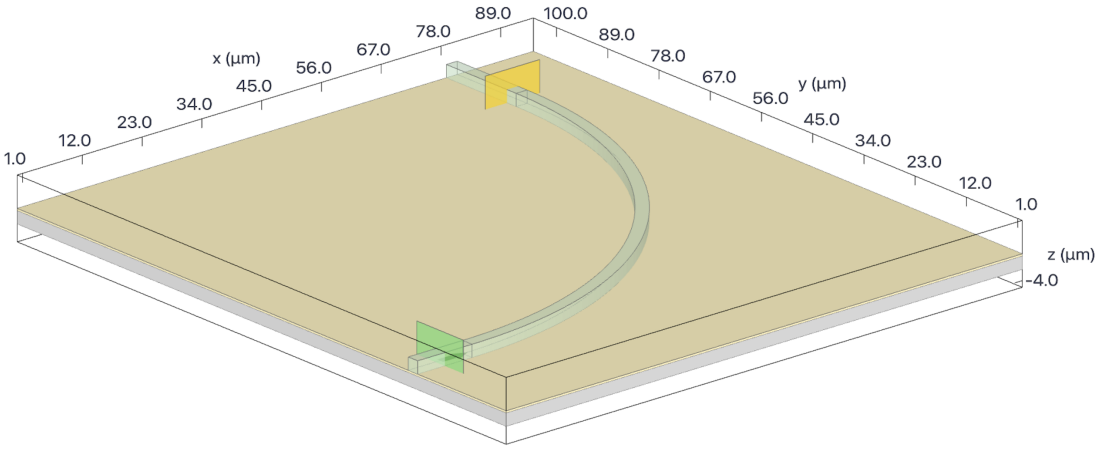

Figure 2.7: Schematic of the FDTD simulation for a circular bend, showing the mode source used to excite the mode and the flux monitor used to measure the transmitted optical power.

Similar to straight sections, the interaction between the bound TM mode and the TE continuum depends on the waveguide cross-sectional geometry, but in bent waveguides it is also influenced by the bend radius [57]. Figure 2.8(a) and (c) presents the bend loss of the TE mode as a function of bend radius for waveguide widths of 2 μm and 3 μm, respectively. The bend loss behaves like a conventional guided mode, decreasing exponentially for both waveguide widths and achieving low loss for radii of several hundreds of microns. In contrast, the TM mode exhibits distinct regions of suppressed bend loss, as shown in Figure 2.8(b) and (d) for waveguide widths of 2 μm and 3 μm, respectively, where losses can fall below 5 dB/cm. It can be observed that the TM BIC modes at a waveguide width of 2 μm experience lower loss compared to a waveguide width of 3 μm

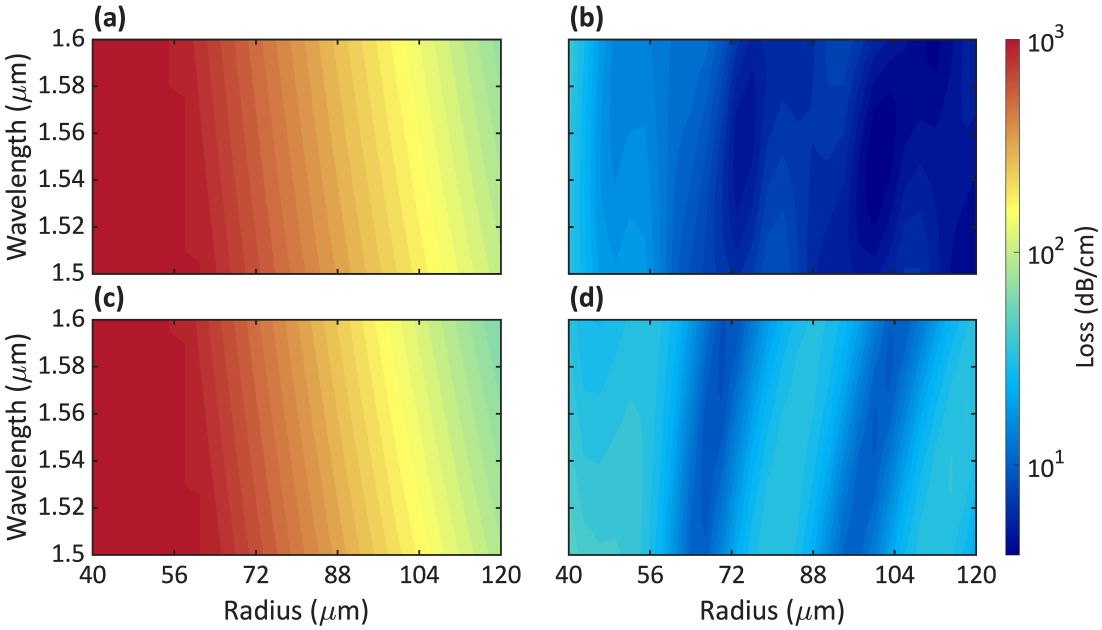

Figure 2.8: Bend loss of a 90° circular waveguide bend. (a) and (b) show the simulated bend loss for a 2 μm waveguide width as a function of bend radius, varied from 40 to 121 μm in 3 μm increments, for the TE and TM polarisations, respectively. (c) and (d) show the corresponding bend loss for a 3 μm waveguide width for the TE and TM polarisations, respectively.

for all bend radii because the 2 μm waveguide width satisfies BIC condition, whereas the 3 μm waveguide width does not satisfy the BIC condition and therefore exhibits higher loss, which is consistent across radii. Figure 2.9 shows the electric field distribution of the circular bends at 40 μm and 100 μm for a 2 μm waveguide width. Figure 2.9(a) illustrates the non-BIC regime, where destructive interference does not occur between the TM mode and the TE continuum, leading to light leakage from the bend. For a 100 μm bend radius, destructive interference occurs, resulting in light confinement within the bend, thereby forming a BIC mode.

Figure 2.10(a) presents the bend loss for waveguide widths of 2 and 3 μm at $\lambda = 1550$ nm for TE modes. For both widths, the TE modes exhibit an exponential decrease in bend loss, consistent with the typical behaviour of bent waveguides. The FDE bend loss simulation for a 2 μm waveguide width was performed as a function of bend radius, as shown in Figure 2.10 (c), to identify the low-loss region. It is evident that the loss decreases exponentially as anticipated, becoming significantly lower beyond a bend radius

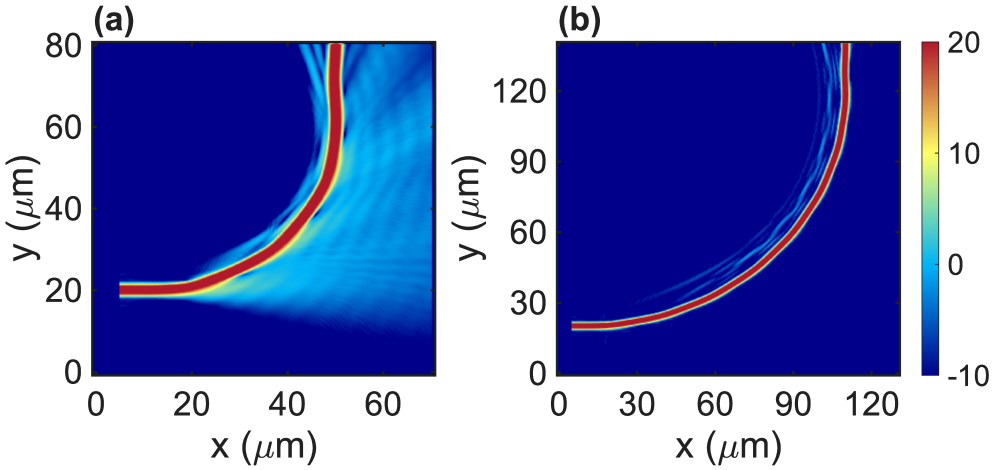

Figure 2.9: Electric field magnitude distribution of circular bend waveguides. (a) Non-BIC circular bend with a bend radius of 40 μm. (b) BIC circular bend with a bend radius of 100 μm. The BIC condition demonstrates significantly lower radiative loss compared to the non-BIC case.

of 350 μm, as highlighted in the inset region. Figure 2.10(b) depicts the bend loss of TM mode for waveguide widths of 2 and 3 μm at $\lambda = 1550$ nm. The TM modes show sharp reductions in loss at specific radii, corresponding to the fulfilment of the BIC condition. Notably, the 2 μm waveguide bend exhibits shallower transitions compared to the 3 μm case, where the difference between the low-loss and high-loss peaks spans nearly three orders of magnitude. This stronger contrast in the 3 μm waveguide width arises from its higher propagation loss in the straight section. Therefore, careful selection of the straight waveguide width is essential to achieve relatively low bend losses. For instance, the 2 μm waveguide maintains losses below 7 dB/cm over a bend radius range from approximately 70 μm to 120 μm, with a minimum loss of $\sim$ 5 dB/cm. This indicates that, when the waveguide width satisfies the straight waveguide BIC condition, low bend loss can be maintained over a wide range of bend radii, making the design robust and tolerant to bend-radius variations. The optical loss for bent waveguides includes contributions from scattering and radiation losses similar to straight waveguides, in addition to the coupling between the bound guided mode and the continuum of radiative modes in BIC guiding conditions [57] for both waveguide cross-section and bend radius. In practical applications, the sensitivity of the BIC condition to geometric variations

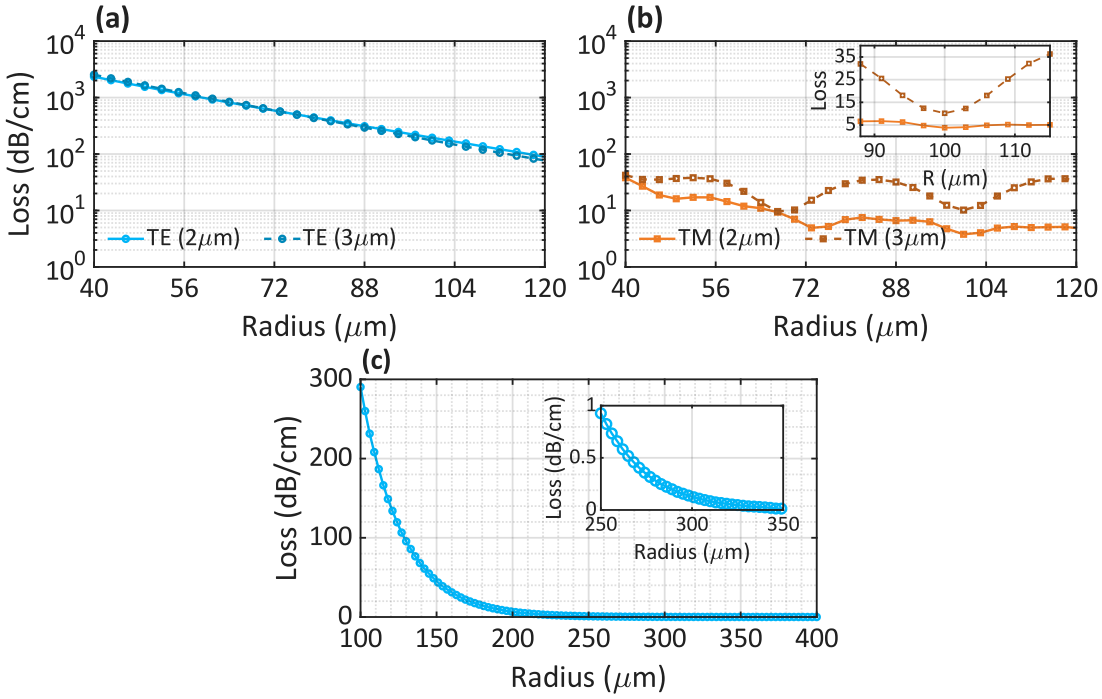

Figure 2.10: Bend loss of a 90° circular waveguide bend at $\lambda = 1.55\,\mu$m. (a) and (b) show the bend loss for 2 and 3 μm waveguide widths as a function of bend radius for TE and TM polarisation, respectively. Zoomed view of (b) shows the low loss region of TM mode for waveguide widths of 2 and 3 μm. (c) FDE bend loss simulation of TE polarisation for 2 μm waveguide width as a function of bend radius, where bend radius varies from 100 μm to 400 μm. Inset depicts the low–loss region.

leads to residual radiation loss, such that the minimum achievable propagation loss is determined by fabrication tolerances and residual leakage.

2.4.6 Directional coupler

The final set of simulations focuses on evaluating the power coupling between adjacent strip-loaded waveguides. Power exchange between waveguides arises from the interaction of their evanescent fields, referred to as directional coupling. This coupling can be analysed using coupled-mode theory or by examining the supermodes of a dual-waveguide system [113]. FDE simulation is performed on two identical strip-loaded waveguides separated by a 1 μm gap, as shown in Figure 2.11. This separation is selected because it can be fabricated reliably using the selected photolithography method. The simulations reveal symmetric and antisymmetric supermodes for both TE and TM

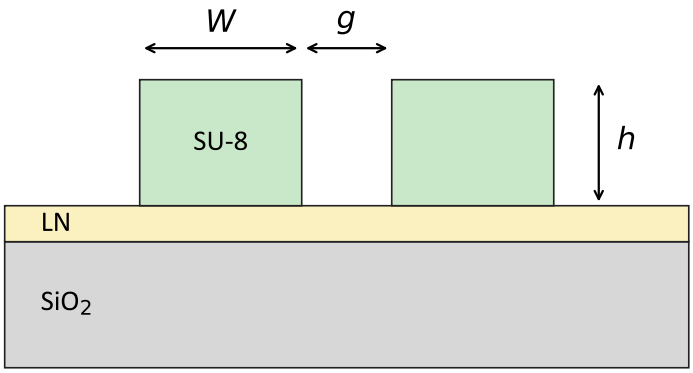

Figure 2.11: Schematic of the FDE simulation for a directional coupler. Each SU-8 waveguide has width and height of 2 μm, separated by a coupling gap of 1 μm.

polarisations. The effective indices of the symmetric and antisymmetric TE supermodes are 1.8355 and 1.8316, respectively, while the corresponding TM supermodes exhibit effective indices of 1.6799 and 1.6785. As expected, the symmetric mode exhibits a higher effective index than the antisymmetric mode. When light propagates through the coupled-waveguide structure, interference between these two supermodes leads to periodic power beating between the waveguides. Complete power transfer occurs after one beat length. The power coupled into waveguide 2 when launching an input power P_1 into waveguide 1 is given by [113]:

$$P_2(L_c) = P_1 \sin^2\left(\frac{\pi\,\Delta n\,L_c}{\lambda}\right), \tag{2.6}$$

where $\Delta n = n_{\text{sym}} - n_{\text{anti}}$ is the effective-index difference between the symmetric and antisymmetric modes, L_c is coupling length and λ is the operating wavelength. Figure 2.12 shows the calculated power coupling for both TE and TM polarisations using Equation 2.6. The TE mode exhibits a stronger coupling per unit length than the TM mode, primarily due to its larger effective-index separation between symmetric and antisymmetric supermodes.

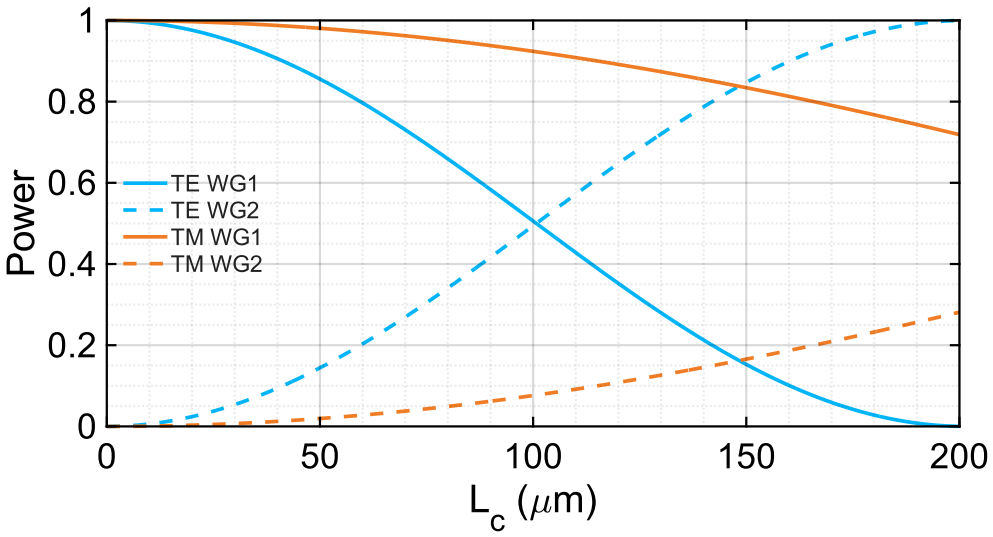

Figure 2.12: Power distribution in each waveguide as a function of coupling length L_c, after launching 1 unit of power into waveguide 1, computed using Equation 2.6 for both polarisations.

2.4.7 Design finalisation

After performing extensive simulations for strip-loaded waveguides, it was decided to validate these simulations for both polarisations. Initially, straight waveguides were fabricated with widths ranging from 1 - 3 μm incremented by 100 nm and five replicas of each waveguide width were fabricated. Subsequently, an S-bend chip was fabricated with radii ranging from 40 - 370 μm to validate against both TE and TM polarisations. For radii from 40 - 121 μm microns, a 3 μm step size was used, and from 130 - 370 μm, a 30 μm spacing was employed. After finalising the straight waveguide and bend radius, directional couplers were fabricated with varied coupling lengths to optimise for 50:50 coupling. For TE polarisation, waveguide crossings were designed, along with a 4-channel coupler using crossovers and a Mach-Zehnder interferometer. For TM polarisation, racetrack resonators were designed, as TM utilises a compact bend radius due to BIC. The dimensions of each device are detailed in the respective section. The subsequent section will present the fabrication of strip-loaded devices and the characterisation of the mentioned devices.

2.4.8 Microfabrication of strip-loaded waveguides

A fabrication process for strip-loaded waveguides is outlined in Figure 2.13. The process started with cleaving a 4-inch 300 nm-thick X-cut LNOI wafer, sourced from NANOLN, into smaller samples. The samples were subsequently solvent-cleaned in an ultrasonic bath to remove surface contamination and particulate residues. SU-8 polymer resist was used as the strip-loading material. A 2 μm layer of SU-8 6002 resist was spin coated onto the LNOI samples using a three-step spin profile (300 rpm for 10 s, 2500 rpm for 30 s, and 4000 rpm for 30 s, each with an acceleration of 500 rpm/s). The waveguides were patterned using direct-write laser photolithography (Heidelberg DWL66+) on the SU-8 resist. Following exposure, the samples were baked at 110 °C for 3 min, developed in PGMEA, and rinsed in IPA for 10 s. After development, the waveguides were hard baked at 200 °C for 45 min. As SU-8 is an epoxy-based negative photoresist, UV exposure initiates cationic polymerisation. The reaction is not fully completed after development, and the subsequent hard-bake step further enhances the crosslinking of the polymer chains, resulting in improved mechanical robustness and chemical stability. The devices were designed as facet-coupled structures, and a thick layer of S1818 photoresist was subsequently spin coated to protect the devices during the cleaving process. Figure 2.14 presents optical images of the fabricated strip-loaded waveguides. These images include straight waveguides, S-bends, waveguide crossings, directional couplers, racetrack resonators, Mach-Zehnder interferometers, spirals, and 4-input/4-output optical couplers..

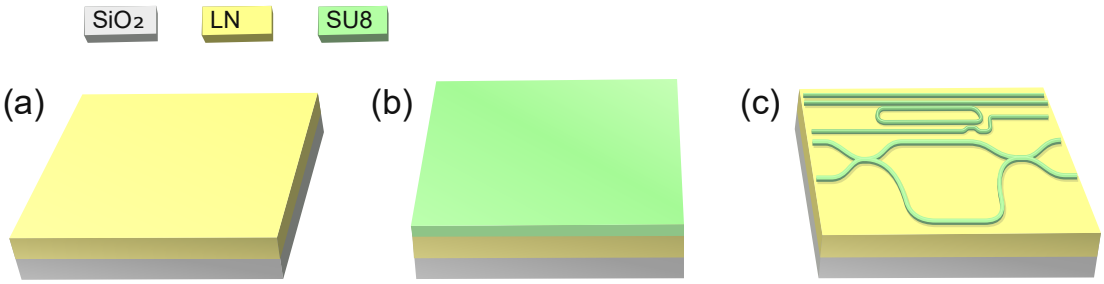

Figure 2.13: Fabrication process of passive strip-loaded devices: (a) LNOI sample, 300 nm X-cut, (b) SU-8 resist is spun, (c) waveguides are patterned using photolithography.

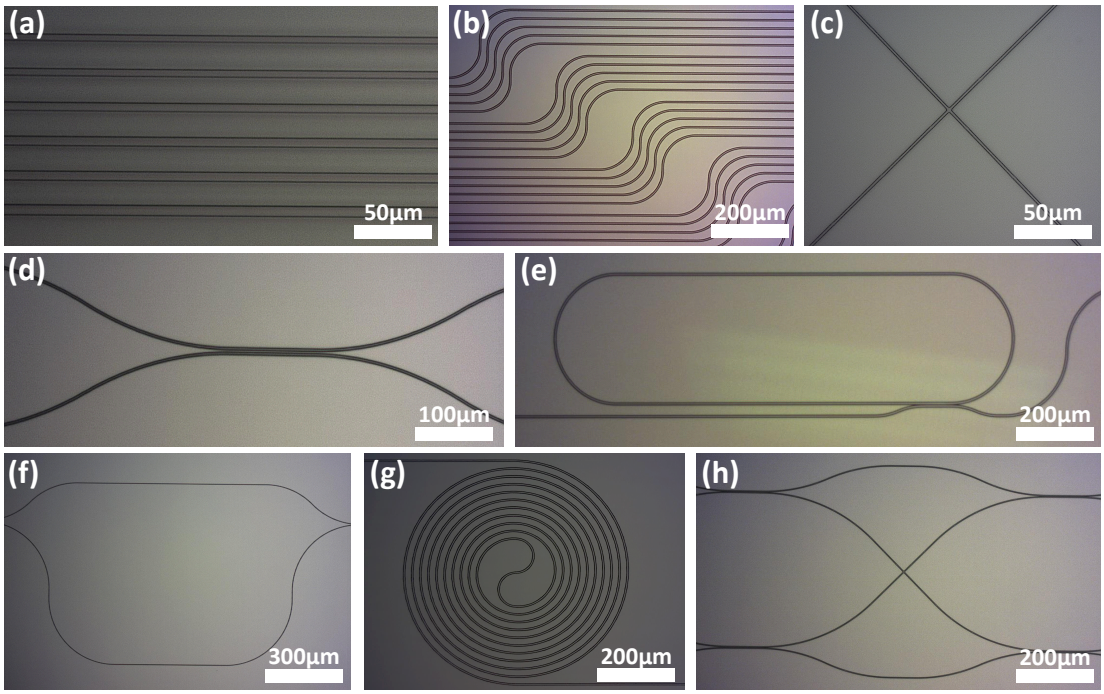

Figure 2.14: Optical microscope images of strip-loaded waveguides: (a) straight waveguides, (b) S-bends, (c) waveguide crossing, (d) directional coupler, (e) race-track resonator, (f) Mach–Zehnder interferometer, (g) spiral waveguides, and (h) 4-input/4-output optical coupler implemented using waveguide crossing.

2.5 Optical characterisation setup

The transmission spectrum of strip-loaded waveguide devices was taken using an end-fire optical injection setup, as shown in Figure 2.15. The optical setup includes a tunable laser source (Agilent-8164B) connected to a optical isolator, which is subsequently linked to a polarisation maintaining lensed fibre. The lensed fibre is utilised to focus the light into a spot with an approximate radius of 1.5 μm facilitating effective mode matching with the waveguides. The light transmitted through the waveguide was collected by an objective lens, followed by a polarisation beam splitter (PBS), and then focused onto a free space photodetector (Thorlabs PDA20C/M) and CCD camera through a beam splitter. The injection fibre and PBS are installed in rotating holders, allowing for the injection and collection of either TE or TM polarised modes. Transmission spectrum is constructed by simultaneously performing a wavelength sweep on the laser and time trace of the detector voltage with oscilloscope.

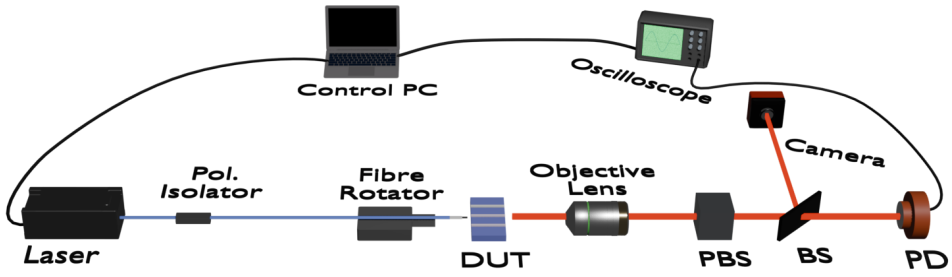

Figure 2.15: Optical transmission setup used for characterisation of waveguides. DUT: device under test; PBS: polarisation beam splitter; BS: beam splitter; PD: photodetector

2.6 Straight waveguides

Figure 2.16 presents the insertion loss of straight waveguides as a function of waveguide width for both TE and TM polarisations. For each width, five nominally identical devices were fabricated and measured. The mean insertion loss for the TE polarisation, shown in Figure 2.16(a), decreases with increasing waveguide width. This behaviour is expected, as wider waveguides support a larger effective core and therefore confine the optical mode more strongly, reducing its interaction with the sidewalls and lowering the associated scattering loss. Furthermore, the TE insertion loss remains relatively constant across the 100 nm wavelength. Figures 2.17(a) and (b) show the insertion loss of the 2 μm and 3 μm TE waveguides, where the error bars represent the standard deviation across the five identical devices, of approximately $\pm 0.5\,\mathrm{dB}$, arising from device-to-device fabrication variation and differences in fibre–chip coupling between measurements.

In contrast, the TM-polarised measurements shown in Figure 2.16(b) exhibit a fundamentally different loss behaviour, as expected from the BIC-driven response of the TM mode. As discussed in the simulation section, the TM mode displays alternating high- and low-loss regions as the waveguide width varies. These variations arise because the BIC condition is satisfied only for specific combinations of waveguide width and wavelength. When the guided TM mode becomes phase-matched to a radiation channel, destructive interference suppresses leakage into the continuum, resulting in a low loss.

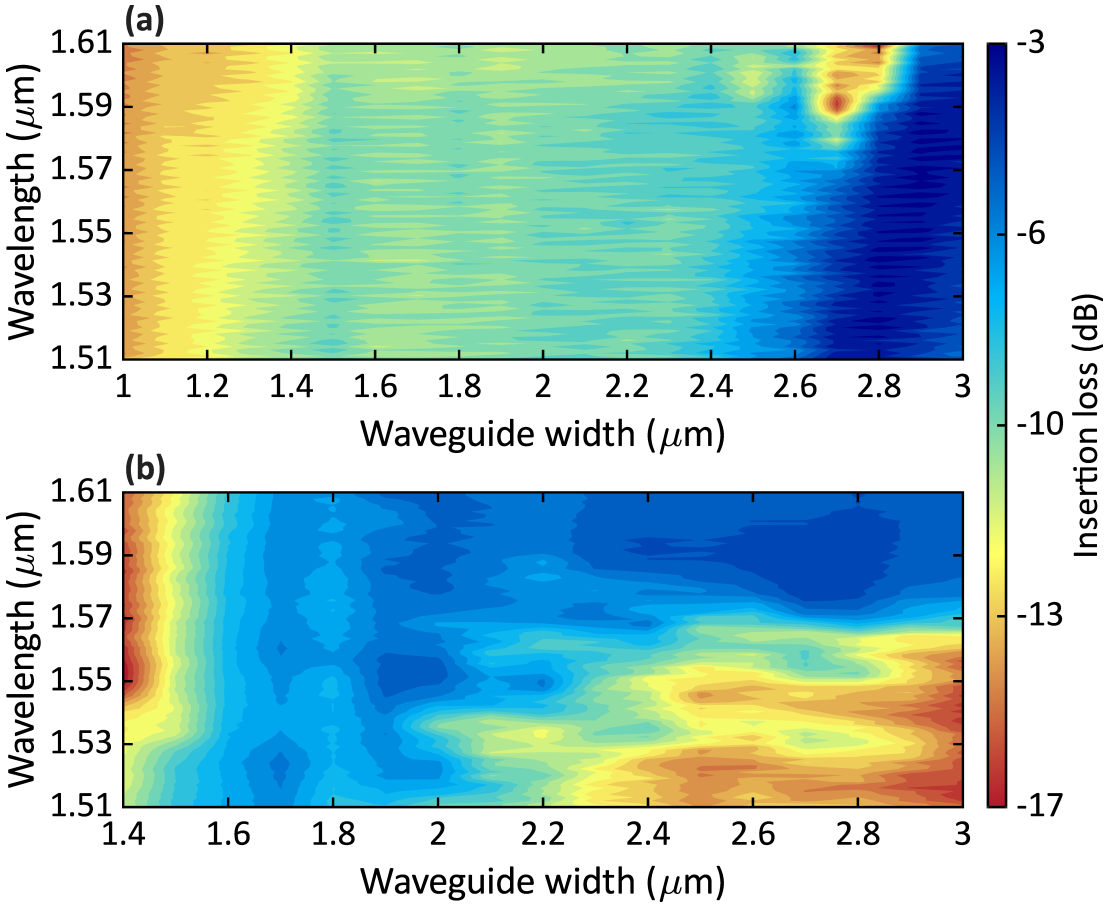

Figure 2.16: Measured insertion loss of straight waveguides as a function of wavelength for different waveguide widths: (a) TE polarisation and (b) TM polarisation.

Conversely, when the BIC condition is not fulfilled, this cancellation breaks down and the TM mode couples efficiently to the continuum, achieving high-loss . Consequently, the TM insertion loss becomes strongly wavelength dependent. Waveguide widths between 1 and 1.3 μm do not support guided TM modes, whereas larger widths show shallower low- and high-loss compared to thinner waveguide width due to weak coupling to the TE continuum. Notably, wavelengths in the 1510–1550 nm range exhibit significantly higher loss for waveguide widths above approximately 2.3 μm (lower-right region of Figure 2.16(b)), corresponding to a region where the TM mode strongly couples to leaky radiation channels. Wavelengths extending toward 1610 nm for widths between approximately 2 and 3 μm (upper region of Figure 2.16(b)), however, fall within a BIC-supported region where destructive interference suppresses leakage, re-

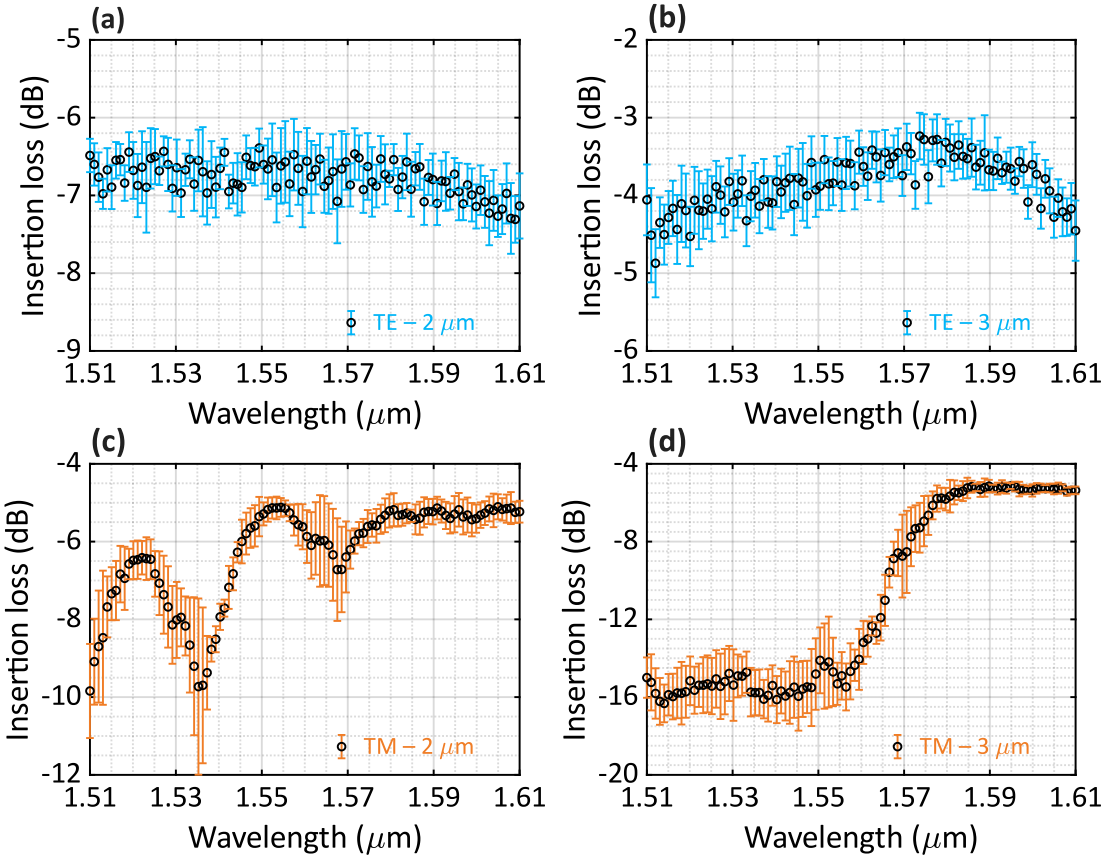

Figure 2.17: Measured insertion loss spectra of straight waveguides for TE and TM polarisations as a function of wavelength for different waveguide widths: (a) TE, 2 μm; (b) TE, 3 μm; (c) TM, 2 μm; and (d) TM, 3 μm.

sulting in reduced loss. Figures 2.17(c) and (d) show the TM insertion loss for 2 μm and 3 μm waveguides. The 2 μm waveguides largely follow the expected low-loss BIC behaviour, though some localised increases in loss are attributed to fabrication-induced width variations that shift the BIC condition. The 3 μm waveguides, for which simulations predict the absence of a BIC, are expected to exhibit high TM loss across the full wavelength range. Experimentally, this behaviour is observed in the 1510–1570 nm region, although the trend diverges from simulation at longer wavelengths. The resulting bandpass-like loss profile arises because the BIC condition depends on both waveguide width and wavelength. Consequently, small fabrication-induced width variations shift the wavelength at which the BIC condition is satisfied, producing the low-loss band observed at longer wavelengths. Such behaviour may be exploited for the development

of wavelength-selective filtering components. The propagation and fibre–chip coupling losses were estimated from the insertion-loss measurements of the straight waveguides. Based on these measurements, the propagation loss is estimated to be approximately 2 dB/cm for both TE and TM polarisations, while the fibre–chip coupling loss is estimated to be approximately 2 dB per facet for the 2 μm-wide waveguides. Overall, the measurements reproduce the key trends predicted by the simulations, with TE loss decreasing with waveguide width and the TM mode exhibiting alternating high- and low-loss regions associated with the BIC condition. The higher measured losses are attributed to sidewall scattering and material absorption, which are not included in the simulations, while shifts in the BIC wavelength are likely due to fabrication-induced width variations.

2.7 S-bends

From the contour plots of straight waveguides, the 3 μm waveguide width was initially identified as low-loss device. This motivated the use of the 3 μm width for investigating bend radii in order to determine low-loss bend configurations suitable for compact ring resonators on this platform. Figure 2.18 presents the mean insertion loss of the S-bend structures for both TE and TM polarisations, with five replica devices fabricated for each bend radius, similar to straight waveguides. Figure 2.18(a) shows the TE-polarised response. The TE mode is guided efficiently for bend radii below approximately 150 μm and, notably, exhibits low insertion loss at radii where simulation predicts that the TE mode should experience high loss or become unguided. At larger radii, the behaviour transitions to that of a conventional dielectric bend, remaining low loss up to approximately 370 μm. The presence of low loss regions at small bend radii is noteworthy, as TE confinement is not expected in this regime. To understand this behaviour, bent-waveguide FDE simulations were performed for the strip-loaded geometry at a width of 3 μm and a bend radius of 94 μm. These simulations revealed that, deeper in the mode spectrum, the 2 μm thick SU-8 strip layer can support both TE and TM guided modes within the polymer layer, as illustrated in Figure 2.19. When the fundamental

TE mode in the LN core becomes cut off, this SU-8 guided TE mode supports propagation, explaining the unexpectedly low insertion loss observed experimentally at small bend radii. The FDTD simulations discussed previously focused on the fundamental LN-confined TE mode and therefore did not capture this polymer-guided behaviour.

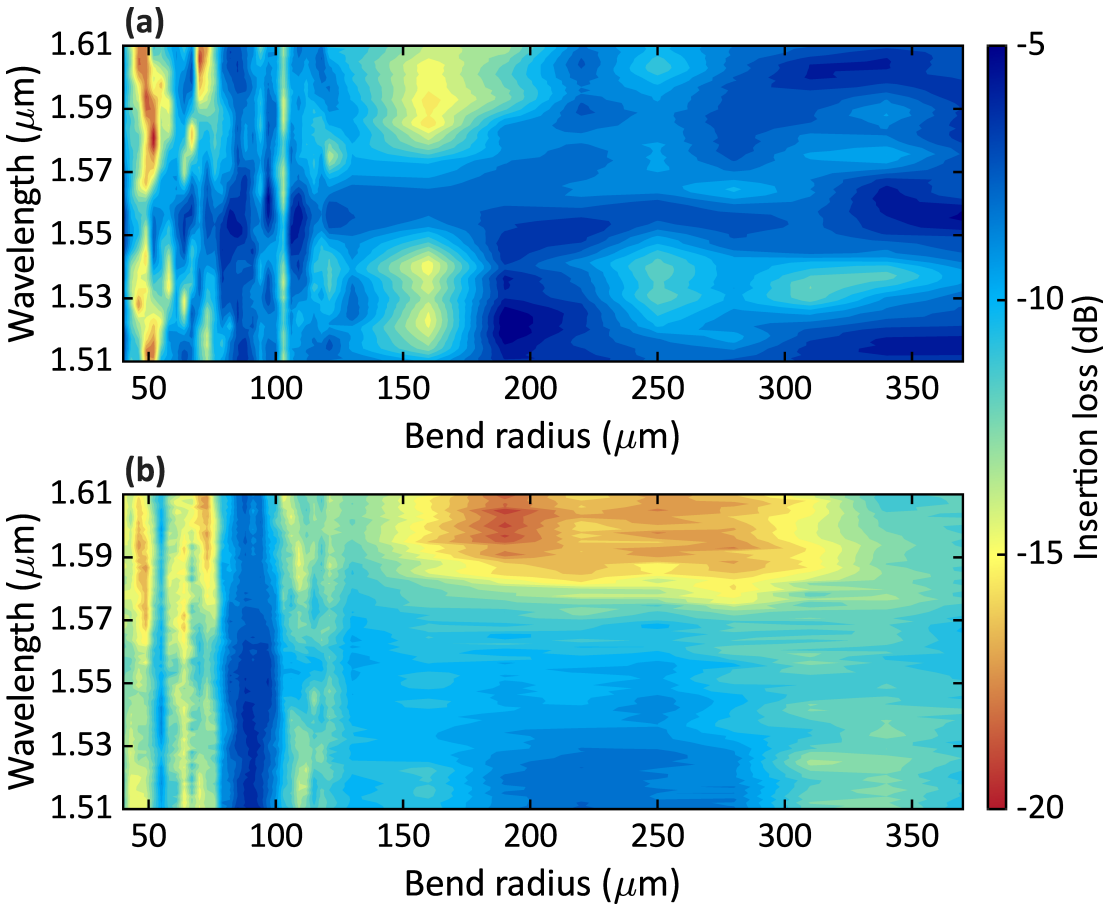

Figure 2.18: Measured insertion loss of S-bends as a function of wavelength for different bend radii: (a) TE polarisation and (b) TM polarisation.

For the TM polarisation, the S-bend response follows the expected BIC-driven loss behaviour. Alternating high- and low-loss regions are observed depending on whether the BIC condition is satisfied, in good agreement with simulations. As the bend radius increases beyond 120 μm, the TM loss decreases and approaches the behaviour of a conventional bend. The insertion loss at 1550 nm for both polarisations is summarised in Figure 2.20, with error bars of $\pm$1.05 dB for TE and $\pm$1.69 dB for TM. Error bars for TM polarisation are higher compared to TE because BIC modes are sensitive to

fabrication variation which is unavoidable. Both modes exhibit a low-loss region between 91 and 100 μm.

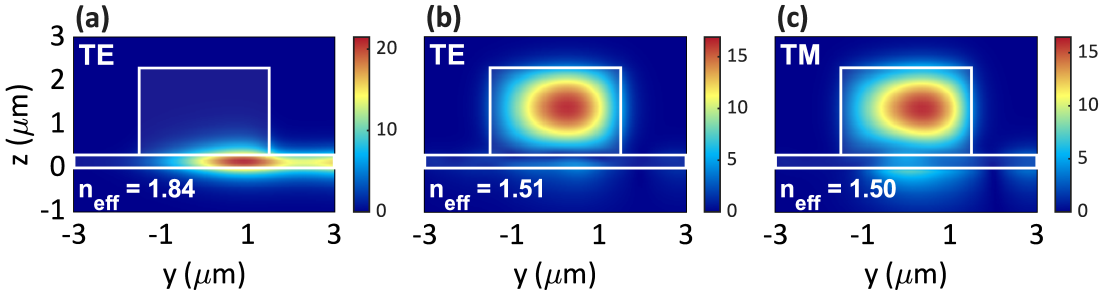

Figure 2.19: FDE mode simulation of a strip-loaded waveguide with a 3 μm waveguide width and a 94 μm bend radius. (a) TE bend mode in the LN layer. (b) TE bend mode in the SU-8 layer. (c) TM bend mode in the SU-8 layer.

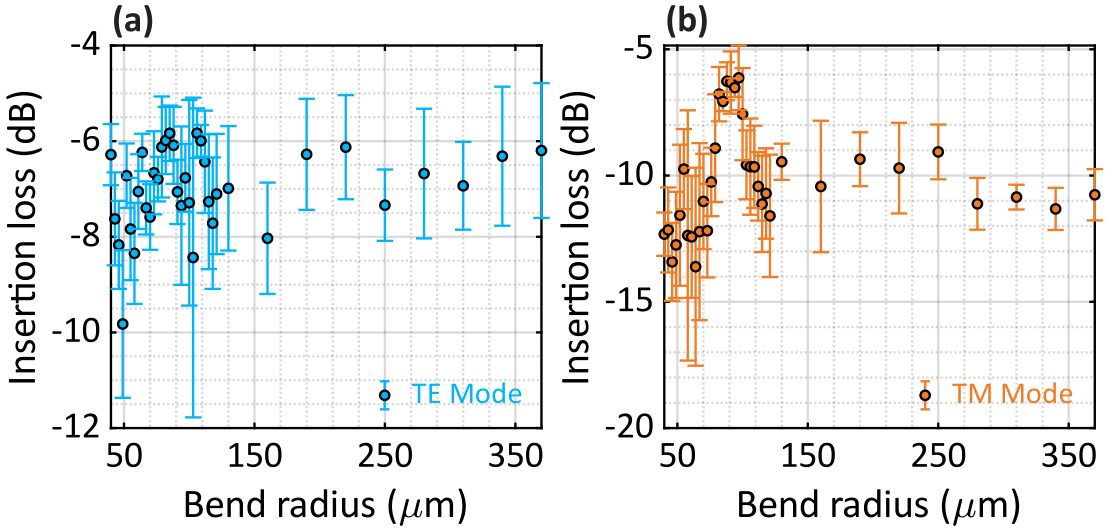

Figure 2.20: Measured insertion loss spectra of S-bend at $\lambda = 1.55$ μm for different bend radii: (a) TE polarisation (b) TM polarisation.

Although the 3 μm waveguides were initially selected for the bend loss experiment, simulations consistently predict that the 3 μm geometry exhibits higher overall loss particularly for the TM mode compared to the 2 μm width, and this trend is also reflected experimentally. Since the 2 μm and 3 μm widths exhibit similar BIC-induced low-loss windows, the 2 μm waveguide width is ultimately preferred. The thinner waveguide provides a smaller optical mode area, improving overlap with the applied electric field and enhancing modulation efficiency, which is especially important for active TM-polarised

devices relying on the weaker r_{13} electro-optic coefficient, in contrast to TE-polarised devices that utilise the stronger r_{33} coefficient. For BIC-based racetrack resonators, a bend radius of 94 μm and a 2 μm waveguide width are selected to realise compact, low-loss devices. For TE-polarised devices, a bend radius of 350 μm and a 2 μm waveguide width are chosen for the same reason, to minimise bend loss while maintaining high modulation efficiency.

2.8 Waveguide crossing and four-channel routing device

PICs are becoming increasingly complex, with the integration of devices on the same chip growing exponentially. This necessitates the routing of light across multiple devices. Waveguide crossings are implemented by positioning two waveguides perpendicular to each other, allowing signals to pass through the intersection with minimal loss and crosstalk. Waveguide crossings play a significant role in optical switching, optical neural networks, optical interconnects, and complex routing architectures, as signal routing among these applications is unavoidable [114, 115]. This underscores the importance of waveguide crossings in PICs. Waveguide crossings have primarily been implemented using multimode interference (MMI) [115, 116, 117] due to their fabrication tolerance, ease of design, and good performance. Several variants of MMI-based designs are utilised, such as inverse design [114], Gaussian beam synthesis [118], and sub-wavelength grating [119], to optimise waveguide crossing performance. These waveguide crossings have been realised on Si [115], SiN [116], polymer [117], and LNOI [120] platforms. Therefore, developing waveguide crossings for the etchless LN platform is essential for routing between devices. We employed MMI-based crossing with a 2-micron waveguide width to simplify the design and fabrication of the devices as shown in Figure 2.21.

Figure 2.22 shows the transmission response of the waveguide crossing for both input ports as a function of wavelength. The data show the mean of the measured devices, with error bars representing the standard deviation. Two devices were measured for input 1 and three for input 2. In Figure 2.22(a), the transmission at both output ports is plotted when light is injected into input 1. Most of the power remains in output 2,

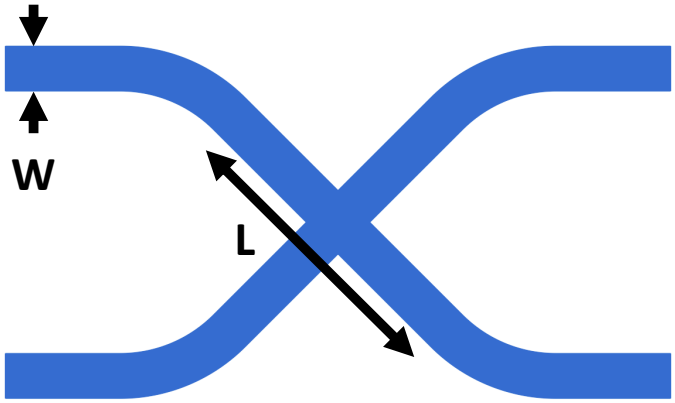

Figure 2.21: Schematic of the waveguide crossing with a waveguide width of $W = 2\,\mu$m and a crossing length of $L = 200\,\mu$m.

with a measured crosstalk of approximately -17 dB. The error bars are ± 0.52 dB for output 1 and ± 0.41 dB for output 2. When light is launched into input 2, the behaviour is reversed, as shown in Figure 2.22(b): output 1 receives the majority of the signal, while output 2 carries only a small portion. The error bars in this case are ± 3.14 dB for output 1 and ± 0.61 dB for output 2. This larger variation for input 2 mainly comes from one device that was damaged near input 2 during cleaving, which reduced its transmission. The crosstalk for both input ports is presented in Figure 2.22(c), where the crosstalk was calculated for each device and then averaged. The crosstalk for input 2 is higher than that of input 1 (-14.5 dB compared with -17.1 dB), again mainly because of the same device. Without this device, the crosstalk for input 2 is -16.2 ± 1.2 dB, which is comparable to input 1. Although the crosstalk of the crossing could be reduced further, doing so would require a more complex device design or additional fabrication steps, which were beyond the scope of this work.

A four-channel input–output routing device was designed to distribute optical power across four ports, implemented using a combination of directional couplers and waveguide crossings, as illustrated in Figure 2.23. The measured transmission spectra for all input–output combinations are shown in Figure 2.24. The device was originally designed to provide equal power splitting among the output ports; however, the experimental results indicate that the power is not evenly distributed. This deviation arises

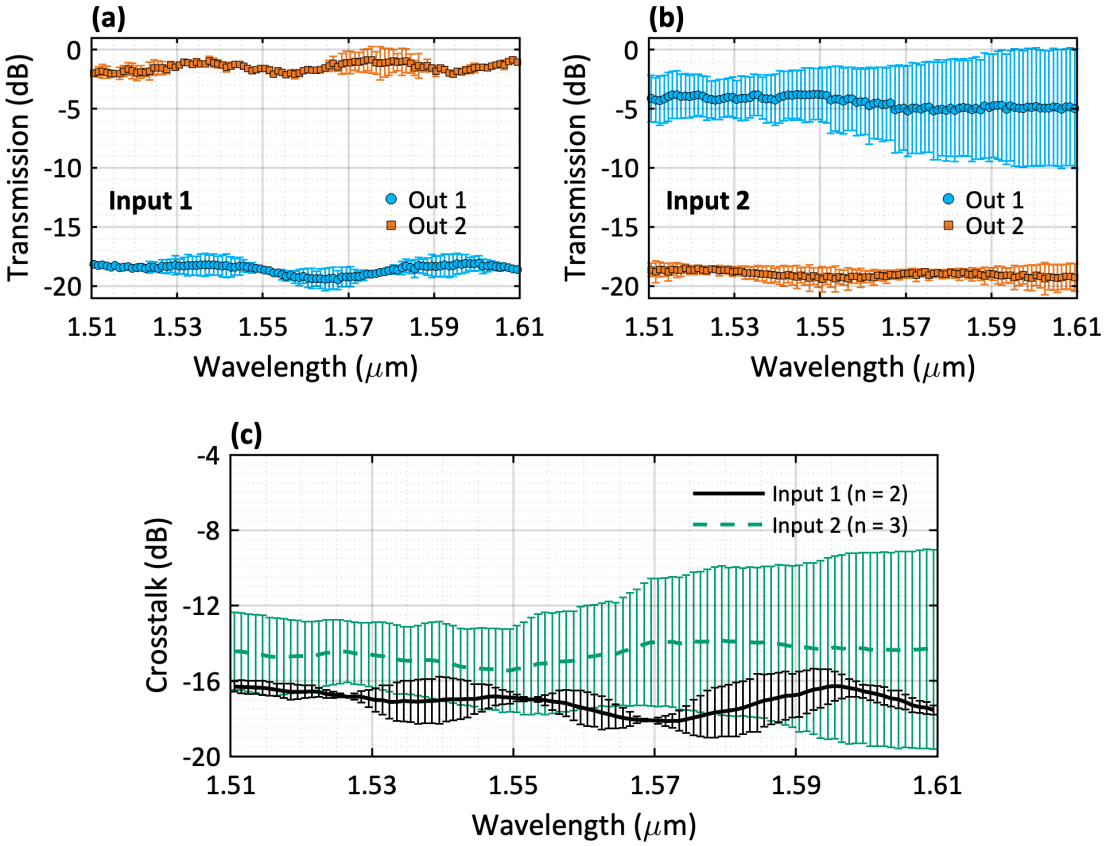

Figure 2.22: Measured transmission of the waveguide crossing for light coupled into (a) input 1 and (b) input 2, and (c) the corresponding crosstalk. Data show the mean across n nominally identical devices ($n = 2$ for input 1 and $n = 3$ for input 2), with error bars indicating the standard deviation.

from the directional couplers not achieving the intended 50:50 splitting ratio. Post-fabrication inspection using optical microscopy revealed that the waveguide gaps were smaller than the designed 1 μm separation, resulting in stronger coupling in one output and consequently altering the expected power distribution. As a result, when light is injected into port 1, the majority of the power is routed to output 4, with output 1 receiving the least power. A symmetric behaviour is observed for input 4, where output 1 becomes the dominant output. Similarly, for input 2 the highest transmission is observed at output 2, and for input 3 the maximum power appears at output 3. In each of these cases, the two remaining output channels exhibit nearly identical transmission levels. Directional couplers splitting ratios can be engineered by adjusting the coupling

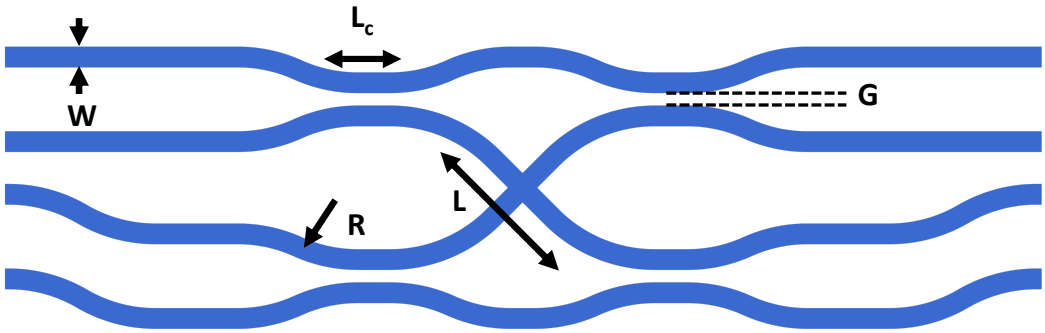

Figure 2.23: Schematic of the four-port routing device. The waveguide width is $W = 2\,\mu$m. Each directional coupler is defined by a coupling length of $L_c = 80\,\mu$m and a uniform coupling gap of $G = 1\,\mu$m. The waveguide crossing length is $L = 200\,\mu$m, and the bend radius is $R = 350\,\mu$m.

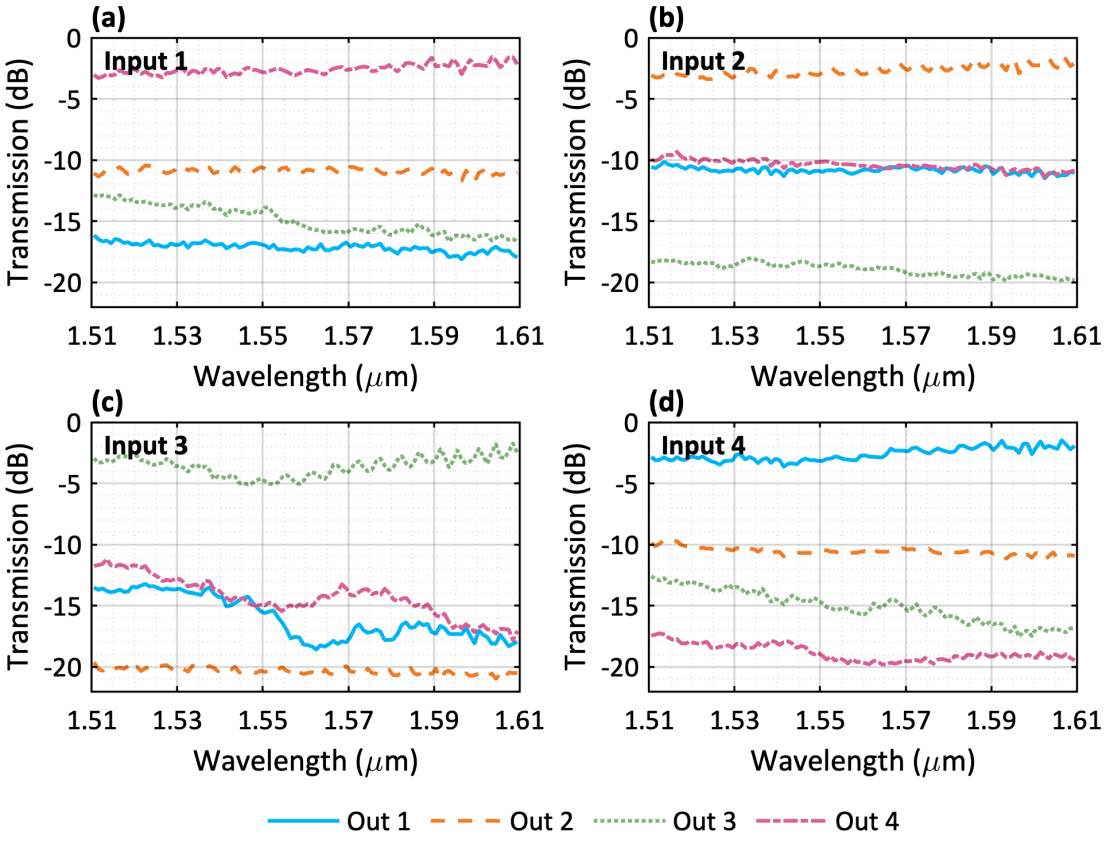

Figure 2.24: Measured normalised transmission spectra of the 4×4 optical coupler for light coupled into (a) input 1, (b) input 2, (c) input 3 and (d) input 4, showing the response of all four output ports.

length or the separation between the waveguides to realise different power-distribution schemes depending on the target application.
These results demonstrate that the four-channel device successfully routes optical power between ports through directional coupling and waveguide crossings, highlighting its potential for applications in multi-port routing, reconfigurable photonic interconnects, and integrated signal-distribution architectures.

2.9 Mach–Zehnder interferometer

A Mach-Zehnder interferometer (MZI) consists of two optical couplers connected by two waveguide arms. Light entering the first coupler is split between the two arms, accumulates a relative phase difference during propagation, and is recombined at the second coupler. The resulting interference determines the optical power distribution between the output ports. Figure 2.25 presents the schematic layout of the MZI, including all relevant device dimensions. The corresponding optical transmission spectra measured at both output ports of the MZI are shown in Figure 2.26. Output port 1 and 2 demonstrate complementary sinusoidal interference fringes originating from constructive and destructive interference during recombination due to the path difference introduced by ΔL between the two arms of MZI. When the phase difference results in constructive interference, the transmission at output 1 reaches its maximum, while the transmission at output 2 is minimised. Conversely, in the case of destructive interference, output 2 reaches its maximum, and the transmission at output 1 is minimised. However, the amplitude response at both ports is not ideal. This arise because the directional couplers in the MZI do not achieve an ideal 50 : 50 power splitting ratio, and their coupling varies with wavelength. Such behaviour is common in practical MZIs, as achieving a very small coupling gaps and perfectly uniform waveguide dimensions is challenging. These fabrication tolerances result in an imbalanced splitting ratio and wavelength-dependent performance.
The free spectral range (FSR) is the wavelength spacing between two adjacent transmission minima (or maxima) in the interference spectrum of the MZI. The FSR of the

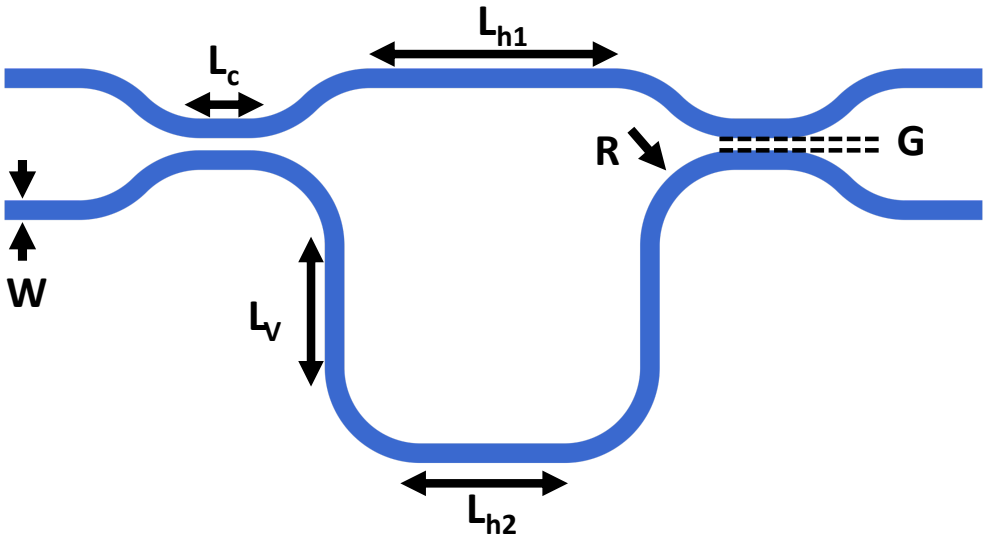

Figure 2.25: Schematic of the unbalanced MZI. The waveguide width is $W = 2\,\mu$m. Each directional coupler is designed with a coupling length of $L_c = 100\,\mu$m and a constant coupling gap of $G = 1\,\mu$m. The horizontal length of the upper arm is $L_{h1} = 2500\,\mu$m, while the lower arm is shortened by $410\,\mu$m, giving $L_{h2} = L_{h1} - 410\,\mu$m. The lower arm includes vertical segments of length $L_v = 150\,\mu$m. The bends are implemented with a bend radius of $R = 350\,\mu$m. The upper arm uses a bend angle of $\pi/4$, whereas the lower arm uses a $\pi/2$ bend. These parameters result in a total optical path length difference of $\Delta L = 990\,\mu$m.

MZI is extracted by detecting the dips at output port 2 and subsequently calculating the difference between the wavelengths of these detected dips. The FSR is shown as a function of wavelength in Figure 2.27(a). The extracted FSR is measured to be 1.1 nm at a wavelength of 1550 nm, with a path length difference $\Delta L = 990\,\mu$m. The FSR data exhibits a strong correlation with the fitted line. The small variation in the extracted FSR is primarily attributed to uncertainty in locating the exact positions of the transmission minima, due to jitter and noise in the recorded transmission spectrum. The FSR data was used to calculate the group index, n_g, of the waveguide using Equation 2.7, as illustrated in Figure 2.27(b). The extracted value of n_g is 2.19 at 1550 nm, which shows good agreement with the simulated n_g value of 2.22 at same wavelength. This further confirms the accurate realisation of the optical path between the two arms of the fabricated MZI. However, the n_g values appear to be scattered due

to the variance in FSR, which directly influence n_g.

$$n_g = \frac{\lambda^2}{\mathrm{FSR}\,\Delta L} \tag{2.7}$$

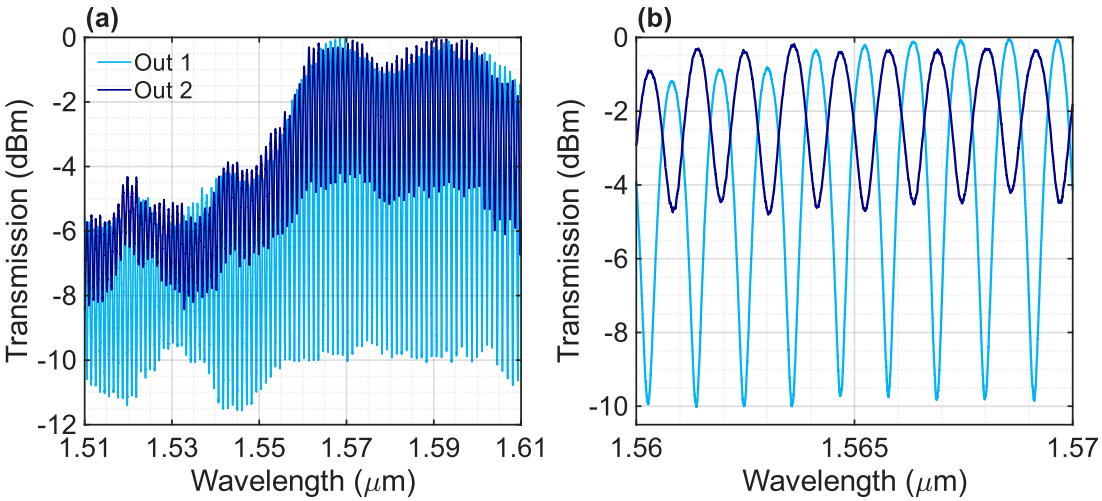

Figure 2.26: Transmission spectra of the Mach–Zehnder interferometer. (a) Measured response at both output ports. (b) Zoomed-in view of the interference fringes for the two ports.

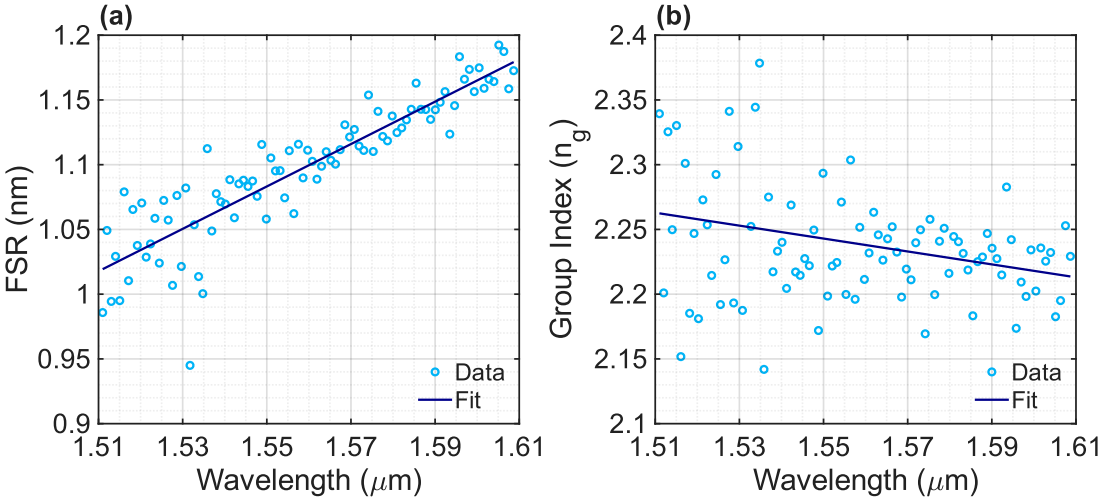

Figure 2.27: (a) Free spectral range of the MZI. (b) Corresponding group index. Both plots include the fitted straight line.

2.10 Racetrack resonator

Figure 2.28 shows the schematic of the racetrack resonator together with its detailed device dimensions. The corresponding normalised transmission spectra for strip-loaded BIC-based racetrack resonators with increasing straight-section lengths are presented in Figure 2.29. The measured free spectral ranges (FSRs) are 0.43 nm, 0.32 nm, and 0.21 nm for straight-section lengths of 1 mm, 1.5 mm, and 2.5 mm, respectively. As expected, the FSR decreases with increasing cavity length, consistent with the inverse relationship described by:

$$\mathrm{FSR} = \frac{\lambda^2}{n_g L}, \tag{2.8}$$

where λ is the wavelength, n_g is the group index, and $L = 2\pi R + 2L_s$ denotes the total cavity length, with R being the bend radius and L_s the straight-section length.

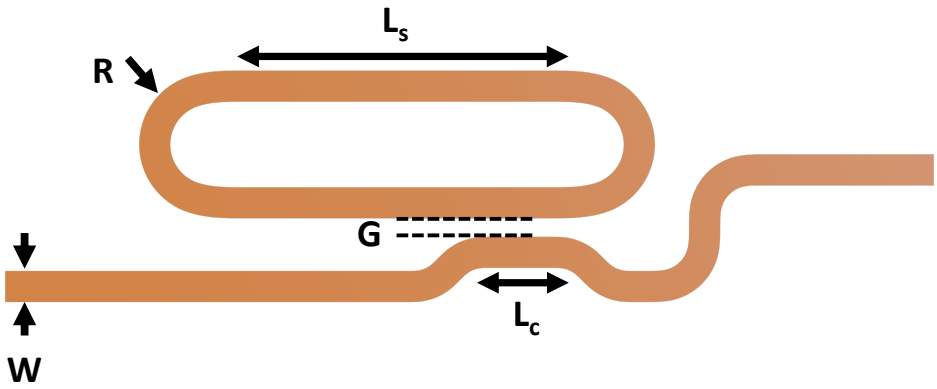

Figure 2.28: Schematic of the racetrack resonator. The waveguide width is $W = 2\,\mu$m, straight section lengths are $L_s = 1\,\mathrm{mm}, 1.5\,\mathrm{mm}, 2.5\,\mathrm{mm}$, coupling gap is $G = 0.75\,\mu$m, and coupling length is $L_c = 100\,\mu$m, and the bend radius $R = 94\,\mu$m.

Across the measured wavelength range, the racetrack resonators exhibit well-defined resonances with consistent spectral characteristics and an almost flat baseline transmission. A more detailed understanding of the resonator behaviour is obtained by fitting the transmission spectra using the analytical transfer function of an all-pass ring resonator. The field transmitted through the bus waveguide results from the interference between the directly transmitted field and the field coupled back from the ring resonator

after multiple round trips [26], giving:

$$T = \frac{a^2 - 2ar\cos(\phi) + r^2}{1 - 2ar\cos(\phi) + (ar)^2}, \tag{2.9}$$

where $\phi = \beta L$ is the accumulated round-trip phase, with β the propagation constant and L the total cavity length. The single-pass amplitude transmission a accounts for the round-trip losses in the resonator and is related to the power attenuation coefficient α through $a^2 = \exp(-\alpha L)$. The self-coupling coefficient r and cross-coupling coefficient k describe the directional coupler, where r^2 and k^2 represent the corresponding power splitting ratios and satisfy $r^2 + k^2 = 1$ for a lossless coupler. Together, the cavity losses and coupling conditions determine the shape and depth of the resonances. Resonance occurs when the round-trip phase is an integer multiple of 2π, leading to constructive interference of the circulating field within the ring. Under this condition, optical power builds up inside the cavity, producing dips in the transmission spectrum measured at the through port as shown in Figure 2.29.

The sharpness of each resonance is described by the quality factor (Q), defined as

$$Q = \frac{\lambda_{\text{res}}}{\text{FWHM}}, \tag{2.10}$$

where λ_{res} is the resonance wavelength and FWHM is the full width at half maximum of the resonance. A higher Q factor corresponds to lower optical losses and a longer photon lifetime within the cavity. Both the round-trip loss and the coupling to the bus waveguide contribute to the decay of the circulating field, broadening the resonance and reducing the measured Q. The Q obtained from a measured resonance is therefore the loaded quality factor, which includes losses associated with coupling to the bus waveguide and is consequently lower than the intrinsic (unloaded) quality factor of an isolated resonator [26]. Because a and r enter Equation 2.9 symmetrically, they cannot be uniquely distinguished from a single resonance, and the fitted resonances were therefore used to extract the loaded quality factor.

The extracted (Q) for the three racetrack geometries are 3.18×10^4 (FWHM: 49.9 pm), 2.75×10^4 (FWHM: 57.6 pm), and 4.17×10^4 (FWHM: 38 pm) at resonance wavelengths

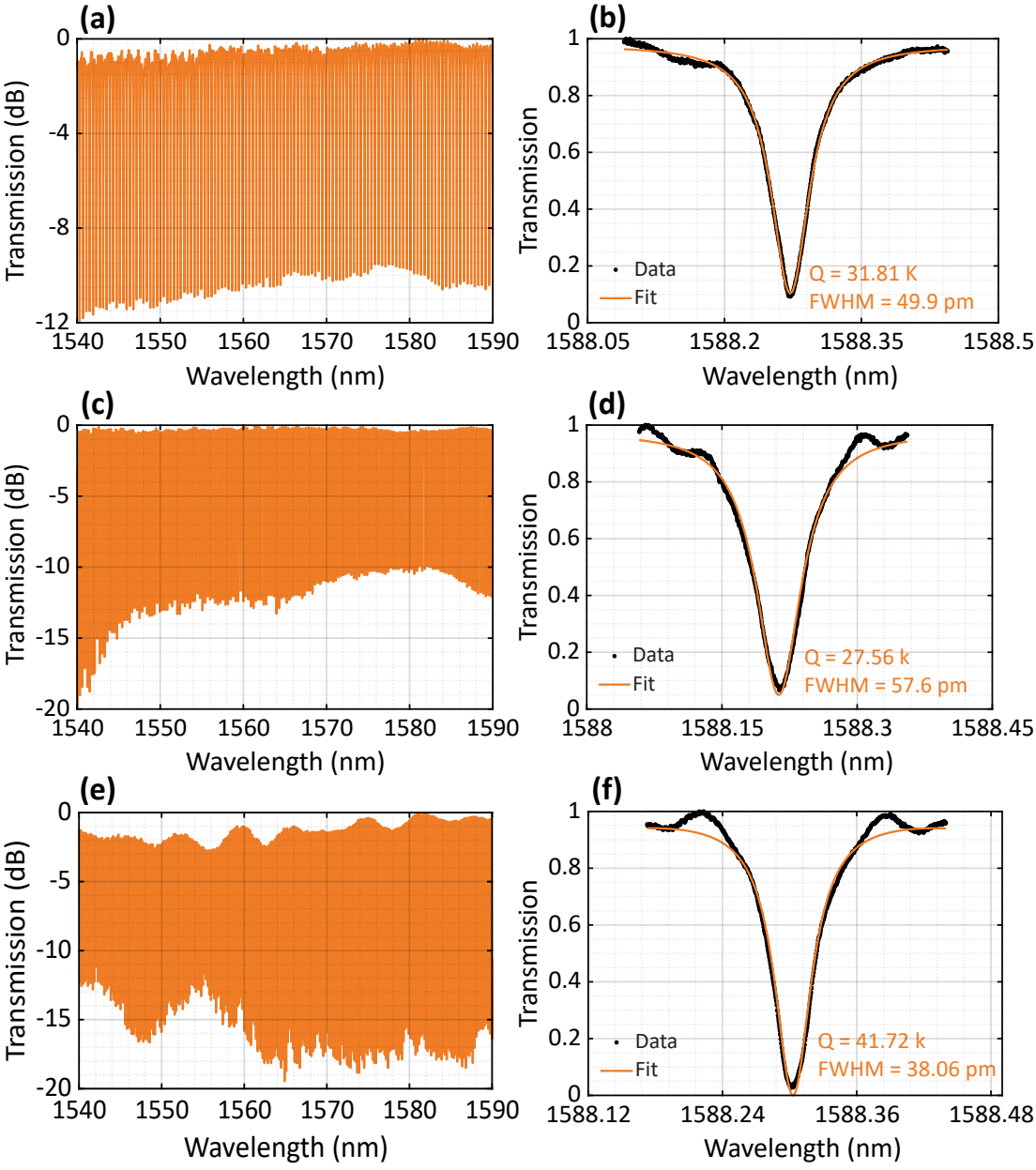

Figure 2.29: TM-mode transmission of strip-loaded micro-racetrack resonators. (a), (c), and (e) correspond to devices with straight waveguide sections of 1.0 mm, 1.5 mm, and 2.5 mm, respectively. (b), (d), and (f) show the associated fitted resonances at $\lambda = 1588.27$ nm, 1588.26 nm, and 1588.25 nm, respectively. Here Q denotes the loaded quality factor and FWHM the full width at half maximum.

of 1588.27 nm, 1588.21 nm, and 1588.30 nm for straight-section lengths of 1 mm, 1.5 mm, and 2.5 mm, respectively as, shown in Figures 2.29(b), (d), and (e). Although the maximum loaded Q factor achieved in this work is lower than the state-of-the-art value of 2.2×10^5 reported for TM BIC-based LN microring resonators [57], the primary objective of this study was not to maximise Q. Instead, the focus was to experimentally realise and characterise a tunable BIC-based racetrack resonator platform, which is discussed in detail in the following chapter. Moreover, for electro-optic modulation, a higher Q factor is not necessarily advantageous, as high-Q resonators exhibit smaller modulation bandwidths due to their longer photon lifetimes [52]. Moderate Q-factors are therefore desirable, balancing resonance sharpness against modulation bandwidth. Experimental characterisation of the S-bend demonstrated that TE-polarised light remains guided through bends with radii as small as 100 μm, in direct contrast to earlier bend-loss simulations, which predicted that such small radii would not support low-loss TE propagation. To further investigate this unexpected behaviour, we injected TE-polarised light into racetrack resonators incorporating the same bend geometries. The racetrack devices supported TE mode, in agreement with the guiding behaviour identified in the S-bend characterisation, and mode simulation also predicted that the SU-8 layer guides mode at 94 μm for 2 μm waveguide as shown in Figure 2.31. The group index extracted from the transmission spectra closely matches the simulated SU-8 TE-mode group index, confirming that the guided TE mode predominantly resides in the SU-8 layer rather than the LN layer.

The normalised transmission spectra of the racetrack resonators are presented in Figure 2.30. The devices exhibit low-frequency modulation of the off-resonance transmission as well as variations in resonance line shapes. As the straight-section length increases, the overall propagation loss also increases, leading to a noticeable reduction in the resonance contrast. The extracted free-spectral ranges are 0.54 nm and 0.40 nm for straight-section lengths of 1 mm and 1.5 mm, respectively. Fitting the measured spectra using Equation 2.9 yields loaded quality factors of 1.18×10^4 (FWHM: 134.7 pm) and 1.70×10^4 (FWHM: 93.7 pm) for respective straight sections. The racetrack with the longest straight section exhibits substantially reduced transmission contrast due to

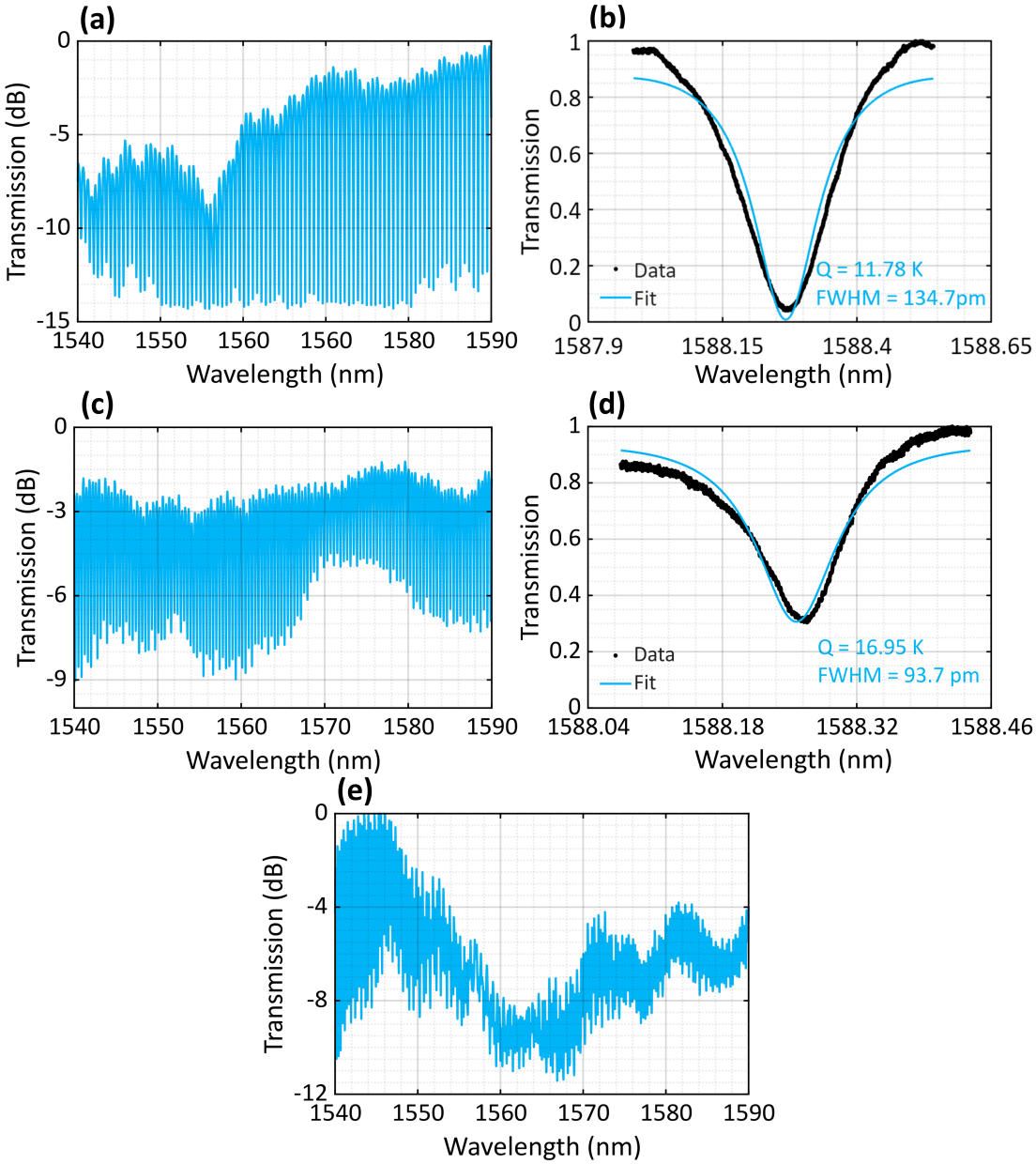

Figure 2.30: TE-mode transmission of strip-loaded micro-racetrack resonators. (a), (c), and (e) correspond to devices with straight waveguide sections of 1.0 mm, 1.5 mm, and 2.5 mm, respectively. (b) and (d) show the fitted resonances of the devices in (a) and (c) at $\lambda = 1588.26$ nm and 1588.27 nm, respectively. Here Q denotes the loaded quality factor and FWHM the full width at half maximum.

increased propagation loss, and as a result, its resonances could not be reliably fitted. Future device designs could incorporate mode converters to adiabatically transfer the SU-8 guided TE mode in the bends into the LN TE mode in the straight sections. Such an approach would enable exploitation of the stronger electro-optic tensor components in strip-loaded LN devices, thereby facilitating efficient TE-polarised modulation.

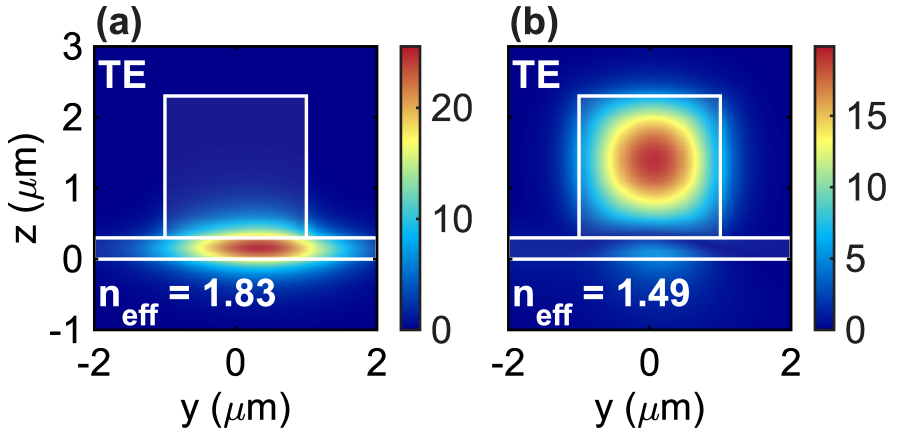

Figure 2.31: FDE mode simulation of a strip-loaded waveguide with a 2 μm waveguide width and a 94 μm bend radius. (a) TE bend mode in the LN layer. (b) TE bend mode in the SU-8 layer.

2.11 Summary

To conclude, this chapter has detailed the simulation, fabrication, and experimental characterisation of etchless strip-loaded lithium niobate waveguide devices. The fabricated structures were designed following the numerical models discussed earlier and were realised for both TE and TM polarisations. Propagation losses were estimated to be approximately 2 dB/cm for both TE and TM polarisations, values that are consistent with previously reported strip-loaded BIC platforms. On X-cut LN, TE-polarised devices require larger bend radii, whereas TM-polarised devices benefit from BIC-assisted confinement, enabling significantly more compact geometries. Among the devices presented, the compact racetrack resonator exhibited the highest loaded quality factor of 4.17×10^4. While higher Q factors improve resonance selectivity, they also reduce the achievable electro-optic modulation bandwidth through increased photon lifetime.

Consequently, moderate Q factors are often preferred in electro-optic modulators, as they enable higher modulation bandwidths. An etchless MZI was also demonstrated, which leverages the strongest electro-optic tensor component for modulation but results in larger device footprints due to the increased bend radius requirements. Conversely, the racetrack geometry provides substantial footprint reduction, though at the expense of relying on a weaker electro-optic tensor component. The implications of these design trade-offs, particularly with respect to modulation efficiency and device performance, are further examined through active electro-optic measurements presented in the following chapter.

Chapter 3

Active strip-loaded devices

Building on the passive strip-loaded lithium niobate devices presented in Chapter 2, this chapter investigates active strip-loaded Mach–Zehnder interferometers and racetrack resonators. By integrating electrodes into the previously demonstrated devices, electro-optic modulation is achieved through the Pockels effect in lithium niobate. This chapter presents the device design, fabrication process, and experimental characterisation, followed by measurements of optical transmission and modulation bandwidth.

3.1 Introduction

Electro-optic (EO) modulators are crucial components of integrated photonics systems, enabling the conversion of electrical signals into the optical domain for high speed communication [18], data centres [121], and emerging applications including quantum information processing, switching [22, 122], and optical neural networks [21]. In addition to modulation functionality, practical photonic integrated circuits rely on active tunability to achieve reconfigurability [20], and compensation for fabrication-induced variations [123]. As the demand for higher bandwidth, lower energy consumption, and enhanced signal fidelity continues to grow, the fundamental physical processes involved in electro-optic modulation become pivotal in determining the efficiency and scalability of photonic systems.

In integrated photonics, various electro-optic effects have been explored, each based on

unique physical principles to modulate the refractive index or absorption of a material when an electric field is applied. These effects include free-carrier plasma dispersion, electro-absorption phenomena such as the quantum-confined Stark effect and Franz-Keldysh effect in bulk semiconductors, thermo-optic tuning, the linear electro-optic (Pockels effect), and Kerr electro-optic effect (DC Kerr) as shown in Figure 3.1. Although all these mechanisms allow for electrical manipulation of light, they differ significantly in terms of modulation efficiency, speed, optical loss, and linearity. Broadly, these mechanisms result in either phase modulation, through changes in the refractive index (e.g., the Pockels and Kerr effects), or intensity (amplitude) modulation, through changes in optical absorption (e.g., the Franz–Keldysh and quantum-confined Stark effects). Phase-modulation devices therefore require an Mach-Zehnder interferometer or ring resonator structure to convert the index change into an intensity change, whereas amplitude-modulation devices can operate directly in a straight waveguide.

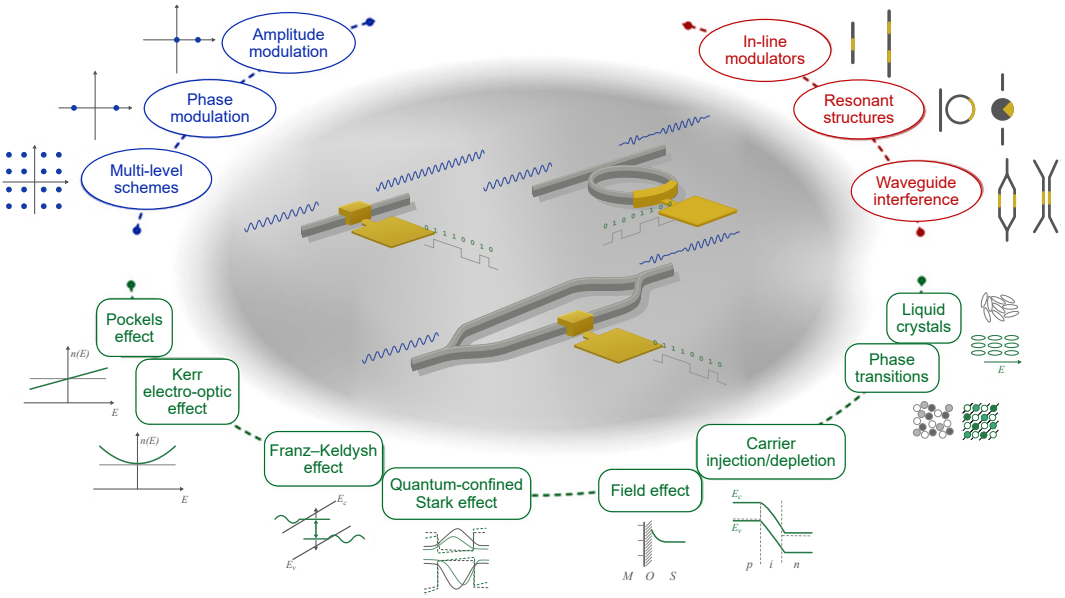

Figure 3.1: Overview of electro-optic modulation mechanisms and integrated photonic modulator architectures, grouped by modulation format (blue), device architecture (red) and physical modulation mechanism (green). Adapted from [23].

The free-carrier effect, commonly referred to as the plasma dispersion effect, describes the dependence of a material's optical properties on the concentration of free charge carriers. This effect is typically exploited using p–n junctions embedded within or

adjacent to an optical waveguide to achieve modulation. The dependence between refractive index modulation and optical loss in carrier-based electro-optic modulation limits modulation efficiency, energy consumption, and linearity in high-speed photonic applications [23, 27, 28]. Electro-absorption effects provide another method for electro-optic modulation through electric-field-induced changes in material absorption spectra. In bulk semiconductors, the Franz-Keldysh effect occurs when an electric field tilts the electronic band structure, enabling sub-bandgap optical transitions and field-dependent absorption changes [124]. In quantum wells, the quantum-confined Stark effect produces stronger electro-absorption, where applied fields shift excitonic energy levels through electron-hole wave function separation, enabling significant modulation over short lengths [125]. While modulators based on these effects achieve high extinction ratios in compact devices, they are inherently lossy and sensitive to wavelength, bias, and material quality, limiting their performance in broadband photonic systems. Thermo-optic modulation offers an alternative method by leveraging the temperature-dependent nature of the refractive index. This is achieved by passing a current through micro-heaters placed within the close proximity of the waveguide, which increases the waveguide's temperature and subsequently changes its refractive index based on the material's thermo-optic coefficient [126], and are extensively employed for DC tuning and reconfiguration in integrated photonic circuits [127]. Although it allows for a significant change in the index, thermo-optic modulation is inherently constrained by slow thermal time constants and high power requirements [128, 129], making it unsuitable for high-speed modulation applications.

The limitations of the above mentioned electro-optic methods have driven the exploration for a fast and low loss modulation technique. The Pockels effect fulfils this requirement as the refractive index change is directly proportional to the applied electric field. Linear electro-optic tuning is observed in non-centrosymmetric materials such as semiconductors like GaN, GaAs, CdTe, and ZnTe; crystals including $LiNbO_3$, $LiTaO_3$, $BaTiO_3$ and KDP; and certain poled polymers with specially designed organic chromophores. These non-centrosymmetric materials, which do not possess inversion symmetry, allow for a strong and instantaneous polarisation response to both DC and

high-frequency electric fields. The refractive index, which is related to the material polarisation through its non-linear optical susceptibility χ, can therefore be tuned linearly with an applied electric field. As discussed in Section 1.2.1, this electro-optic response can be described using the dielectric impermeability tensor and index ellipsoid formalism, resulting in the refractive index change given by

$$\Delta n = -\frac{1}{2} n^3 r E, \tag{3.1}$$

where n represents the refractive index, r is the relevant electro-optic coefficient, and E is the applied electric field. The cubic dependence on refractive index arises from the perturbation of the dielectric impermeability tensor and the corresponding deformation of the index ellipsoid.

Among materials supporting a strong Pockels effect, lithium niobate has emerged as a leading platform for high-performance electro-optic modulation. Lithium niobate combines large electro-optic coefficients, broad optical transparency, and excellent thermal stability, making it particularly well suited for phase modulation in demanding photonic systems. The recent advent of LNOI has further enabled tight optical confinement and strong electric field overlap, allowing the realisation of compact, low-voltage, and high-speed integrated modulators [24].

Despite these advantages, lithium niobate integration presents challenges related to material processing, waveguide fabrication, and heterogeneous integration with other photonic platforms which is discussed in section below.

3.2 Strip-loaded lithium niobate for EO modulation

Several approaches have been used to realise efficient EO modulators on a LNOI platform. Monolithic LN devices, where waveguides are fully or partially etched into the thin film, exhibit exceptional performance with high quality factors microrings ($> 10^6$), and low propagation loss [46, 49, 48]. However, the material is difficult to etch and the fabrication of waveguides relies on the transfer of a lithographic mask into the LN material via inductively coupled plasma-reactive ion etching (ICP-RIE), which must be

optimised for line-edge smoothness to minimise scattering losses [36, 90]. The LN etch process is generally considered as incompatible with other material platforms sharing toolsets due to contamination of the process chamber that can detrimentally affect subsequent processing [41]. The heterogeneous integration of lithium niobate with silicon, achieved through either transfer printing [52, 53, 130] or thin-film bonding [131, 132], offers an alternative pathway for realising EO modulators. This approach enables LN to be incorporated as a back-end process within silicon photonics, thereby combining the high-performance electro-optic properties of LN, which silicon itself lacks due to its centrosymmetric crystal structure, with the mature passive photonic components already established in silicon photonics. In transfer-printed devices, the hybrid integration process typically requires additional fabrication steps for membrane release, alignment, and bonding, and the lithium niobate membranes often need to be etched to define the waveguide structures, resulting in increased process complexity.

As an alternative to etched waveguides, there have been a number of demonstrations of strip-loaded waveguiding on the LNOI platform utilising SiN [91, 92, 93, 94, 95], Si [96, 97], TiO_2 [98, 99], and chalcogenide glass [100]. By patterning dielectric or polymer strips onto the LNOI, optical modes can be guided via effective refractive-index effects, with optical confinement to the LN material maximised through the use of low refractive index strip materials [101]. Although an etch-free process, strip loaded waveguides are typically weakly guiding, leading to prohibitive radiative bend losses for radii below the few hundred micron range. Although this is sufficient for long propagation length interferometric modulator geometries, it is prohibitive for production of compact optical devices on-chip. To overcome these limitations, bound states in the continuum (BIC) have recently been explored as a mechanism to enhance optical confinement in dielectric waveguides [57]. BIC modes enable strong localisation of light within a waveguide without introducing significant radiation losses, thereby allowing strip-loaded structures to achieve compact devices similar to that of fully etched counterparts while retaining fabrication simplicity with recent demonstration of micro-resonators and modulators [57, 102, 103].

Table. 3.1 summarises the key characteristics of various lithium niobate platforms

employed for realising electro-optic modulators. Monolithic LN modulators offer the highest EO performance but are limited by aggressive fabrication processes. Transfer-printed devices, while enabling heterogeneous integration, require LN etching and an additional transfer step, which can increase process complexity. Strip-loaded platforms provide a good balance between EO performance and fabrication simplicity but typically exhibit larger bend radii. The multilayer BIC approach yields good performance but at the expense of complicated fabrication. The strip loaded BIC approach offers reduced bend radius and simplified fabrication with low loss as discussed in detail in Chapter 2. We show the smallest active BIC-based resonator to date, to the best of our knowledge with adequate EO performance compared to other LN platforms. Along with that we have realised strip loaded MZIs, and both of these devices design and fabrication processes is discussed below.

3.3 Design of strip-loaded devices

The MZI and racetrack geometries employ the same design as discussed in Chapter 2, with the addition of electrodes for phase modulation, as shown in Figure 3.2. The MZI electrodes are positioned at 5 μm from the edge of the waveguide, with a width of 200 μm, while the lengths of the top and bottom electrodes are 2.5 mm and 2.09 mm, respectively. For the racetrack resonator, the electrodes are positioned at 4 μm from the waveguide edge, with a length of 2.5 mm and a width of 120 μm.

The electrode-to-waveguide separation was selected based on a trade-off between modulation efficiency and fabrication constraints. The racetrack resonator employed a smaller electrode separation of 4 μm to compensate for the lower electro-optic interaction associated with TM-polarised operation through the r_{13} coefficient. In contrast, the MZI devices operated using TE-polarised modes and exploited the larger r_{33} coefficient, allowing a larger separation of 5 μm. The smaller electrode spacing became feasible following the development of the bilayer lift-off process described in Section 3.4.1, whereas the initial single-layer metallisation process limited the minimum achievable electrode gap.

Table 3.1: Comparison of lithium niobate platforms for electro-optic modulators.

Platform	Device	Cut	Bend Radius (μm)	Prop. Loss (dB/cm)	Fibre–Chip (dB)	Add. Loss (dB)	Total Loss (dB)	Fabrication	EO coeff.	$V_\pi L$ (V · cm)	Tunability (pm/V)
Monolithic[a] [46]	Microring	X	80	0.093	–	–	> 0.093	LN etching	N/A	N/A	N/A
Monolithic [37]	Racetrack / MZI	X	–	3	10	N/A	> 13	LN etching	r_{33}	– / 7	1.8 / –
Transfer printing[a] [130]	Microring	Z	40	3	–	–	> 3	SiN + LN etching	N/A	N/A	N/A
Transfer printing [52]	Microring	X	100	–	4	–	> 4	SiN + LN etching	r_{33}	–	1.7[b]
Transfer printing [51]	MZI	X	–	–	18	3.3	> 21	SiN + LN etching	r_{33}	6[b]	–
Strip-loaded [91]	Microring	X	300	0.32	–	–	> 0.32	SiN etching	r_{33}	–	1.78
Strip-loaded [94]	Racetrack	X	300	0.2	12.8	N/A	13	SiN etching	r_{33}	5.1	2.9
Strip-loaded [95]	MZI	X	300	–	13.6	5.4	19	SiN etching	r_{33}	2.1	–
Strip-loaded BIC [57, 134]	Microring[a]/MZI	Z	~ 100	1.5	20	N/A	> 21	Non-etched	r_{51}	N/A / 80	N/A / –
Multilayer BIC [108]	MZI	X	–	1.36	3.10	N/A	5.4	SiN etching	r_{33}	10.8	N/A
This work	**Racetrack**	**X**	**94**	**2**[c]	**4**[c]	**N/A**	**6**	**Non-etched**	r_{13}	**35**	**0.49**
This work	**MZI**	**X**	**350**	**2**[c]	**4**[c]	**N/A**	**6**	**Non-etched**	r_{33}	**7.43**	**14.67**

[a] Passive device (no active modulation demonstrated).

[b] Single-arm measurement.

[c] Indicates that the value is estimated from insertion loss measurement.

– Not reported.

The electrode configurations used for both the MZI and racetrack are not optimised for high-speed operation. Electrode designs, such as ground–signal–ground (GSG) configuration, are widely adopted for achieving high bandwidth and improved impedance matching [38, 133].

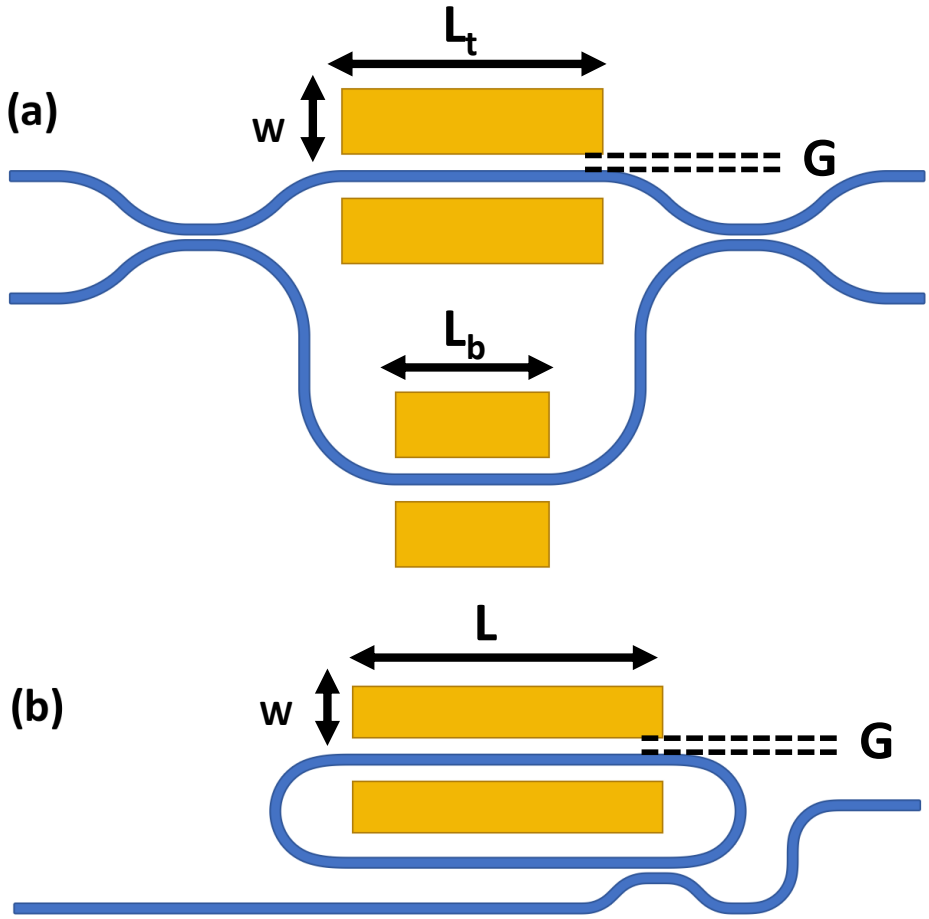

Figure 3.2: Schematic of active strip-loaded devices: (a) MZI and (b) racetrack, where W is the electrode width, G is the electrode gap from the waveguide, L_t and L_b are the lengths of the top and bottom MZI electrodes, respectively, and L is the length of the racetrack electrode.

3.4 Fabrication of active devices

The fabrication process for active strip-loaded devices is outlined in Figure 3.3. The 300 nm X-cut LNOI from NanoLN Ltd. was used, similar to the one used in the previous chapter. The first three steps are similar to those mentioned in the previous chapter, involving the fabrication of passive strip-loaded devices with the use of photolithography in SU-8 photoresist. Metal contact regions were defined using a lift-off process and metal evaporation of a bilayer of 50 : 200 nm Ti:Au. The optical waveguides are designed as facet coupled devices using a cleaved end-facet process.

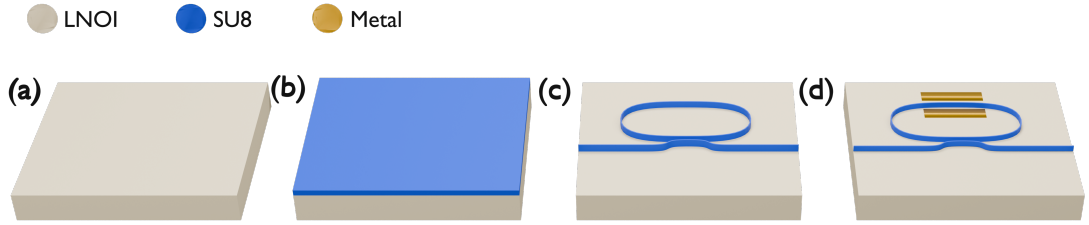

Figure 3.3: Fabrication process of active strip-loaded devices (a) LNOI sample, 300 nm X-cut, (b) SU-8 resist is spun, (c) waveguides are patterned using photolithography, and (d) metal deposition.

3.4.1 Strip-loaded LN metallisation

The metal electrodes for electro-optic tuning on strip-loaded lithium niobate were patterned using a lift-off process. Metallisation on a 2 μm thick polymer presents challenges for achieving a clean lift-off and accurate pattern transfer to minimise scattering loss. To address these challenges, both single-layer and bilayer lift-off metal deposition processes were investigated to achieve precise metal deposition on strip-loaded devices.

Single layer metal deposition

The single layer metal deposition process necessitates the use of a positive resist, making it a rapid and straightforward method for metallisation on PICs [135]. In this work, SPR4.5 positive photoresist was employed for strip-loaded waveguide metallisation due to its increased thickness, which was required to achieve reliable metal lift-off over the

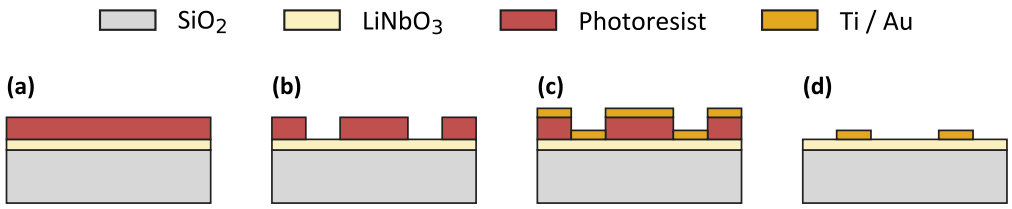

Figure 3.4: Schematic of the single layer metal deposition process: (a) spin coating of photoresist on LNOI substrate, (b) photolithography to define and open metal regions, (c) deposition of a 50 nm Ti adhesion layer followed by a 200 nm Au layer, and (d) metal lift-off.

approximately 2 μm-thick strip-loaded devices. The procedure involves the spinning of the SPR4.5 resist, which is baked at 115°C for 2 minutes, followed by a lithography step to create openings for metal deposition. Subsequently, metal was deposited using a metal evaporator with a composition of 50 nm : 200 nm Ti:Au as shown in Figure 3.4. Titanium is used because gold exhibits poor adhesion to common PIC substrates and tends to peel or delaminate when deposited directly [136]. Therefore, a thin titanium layer was deposited beneath the gold contacts to ensure strong adhesion to the underlying substrate and to enhance the robustness and electrical reliability of the electrodes. Figure 3.5 presents an optical image of the MZI where the metal is deposited. It can be observed that the lift-off process is not entirely clean, and some metal remains on the waveguide, which introduces loss. This is mainly due to the surface topography of the strip-loaded waveguides. Since the SU-8 strip is 2 μm in height, the SPR4.5 resist does not coat uniformly over such a high topography, becoming thinner on top of the waveguide and accumulating near its base. This non-uniform resist profile prevents a clean lift-off, and making it difficult to achieve smaller gaps, such as 5 μm, and resulting in residual metal on the waveguide. Thus, achieving clean lift-off for fine-resolution features is challenging with single-layer metal deposition on 2 μm tall waveguides. This limitation can be addressed using a bilayer resist process, which planarises the topography and provides a cleaner lift-off, as discussed in the following section.

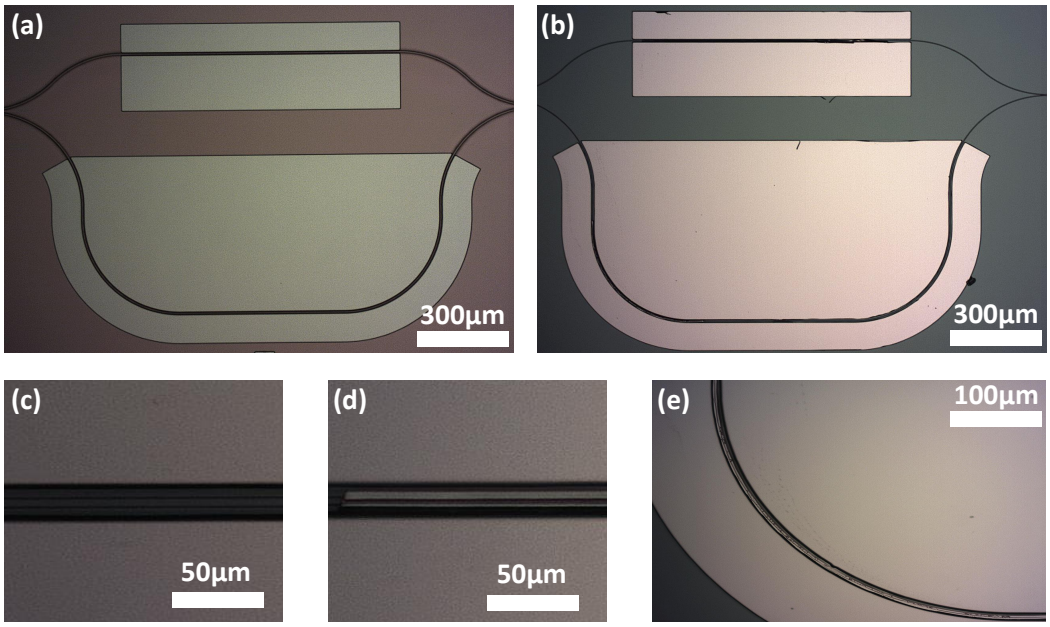

Figure 3.5: Optical microscope images of MZI electrode at different fabrication stages: (a) electrode openings defined after photolithography, (b) metal deposited within the electrode openings, (c) magnified view of the straight section of the bottom electrodes, (d) magnified view of the straight section of the top electrodes showing metal remaining on top of the waveguide, and (e) enlarged view of the bent sections highlighting metal on the waveguide.

Bilayer metal deposition

The bilayer lift-off processes employ two resist layers to achieve controlled undercut profiles that enable clean metal removal. Initially, the lift-off resist (LOR) is spun, followed by the application of a positive resist on top as shown in Figure 3.6. This metal deposition method offers significant advantages in terms of resolution, metal removal, and yield compared to conventional single-layer metal deposition [135]. The bilayer deposition requires the optimisation of multiple parameters, including resist thickness, bake time, bake temperature, and development, to achieve an acceptable undercut for effective metal lift-off. In this study, an LOR10B lift-off resist layer was spin-coated and baked at 190 °C for 5 minutes, followed by spin-coating of S1818 positive photoresist. The combined resist stack thickness was approximately 3 μm, which is intentionally thicker than the 2 μm waveguide layer to ensure reliable and clean metal lift-off as shown in Figure 3.7.

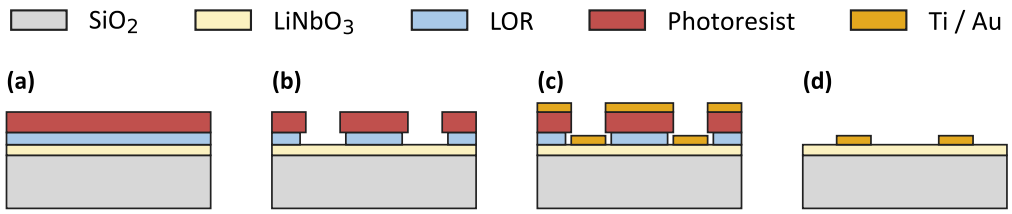

Figure 3.6: Schematic of the bilayer metal deposition process: (a) spin coating of LOR followed by photoresist on the LNOI substrate, (b) photolithographic patterning of the bilayer resist stack, (c) deposition of a 50 nm Ti adhesion layer followed by a 200 nm Au layer, and (d) metal lift-off.

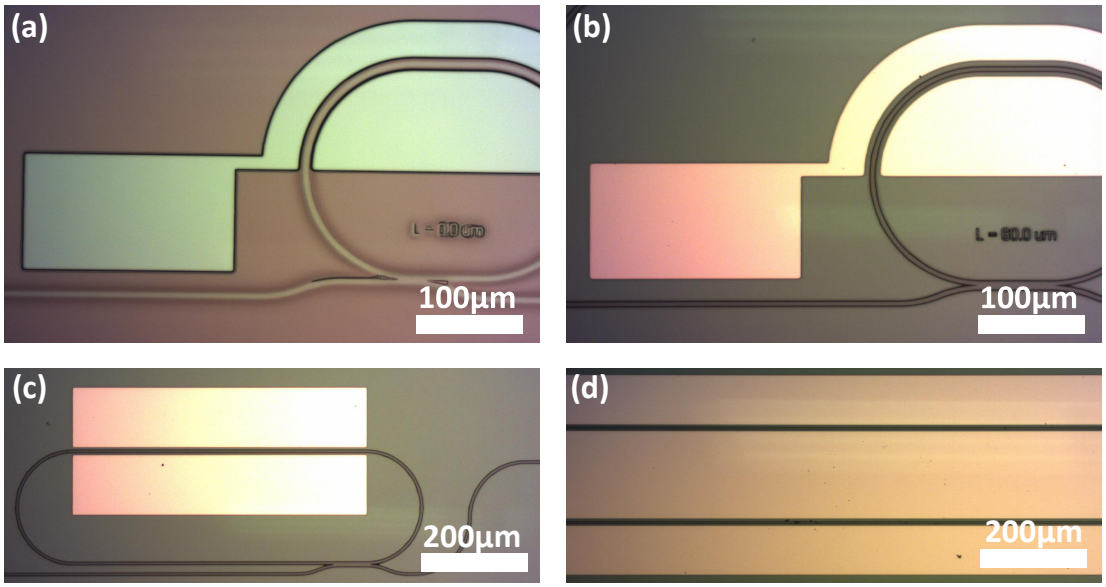

Figure 3.7: Optical microscope images of metal electrodes fabricated using a bilayer lift-off process, illustrating different electrode–waveguide gaps: (a) electrode openings defined after photolithography, where the dark outline around the electrodes corresponds to the resist undercut, (b) metal electrodes deposited on a ring resonator with a 5 μm gap from the waveguide, (c) electrodes on a racetrack resonator with a 4 μm gap, and (d) push–pull electrode configuration with a 4 μm gap on each side of the waveguide.

3.5 Electro-optic characterisation

The devices are optically characterised using the same end-fire fibre injection rig as that used in the previous chapter. For bandwidth measurements, tungsten probes are used to contact the electrodes, and 20 MHz function generator (TG120) is used to supply

sine wave as input signal to electrodes as shown in Figure 3.8. An auxiliary output is sent to the oscilloscope, which is employed to capture both the modulated optical signal from the photodetector and the electrical signal used for modulation.

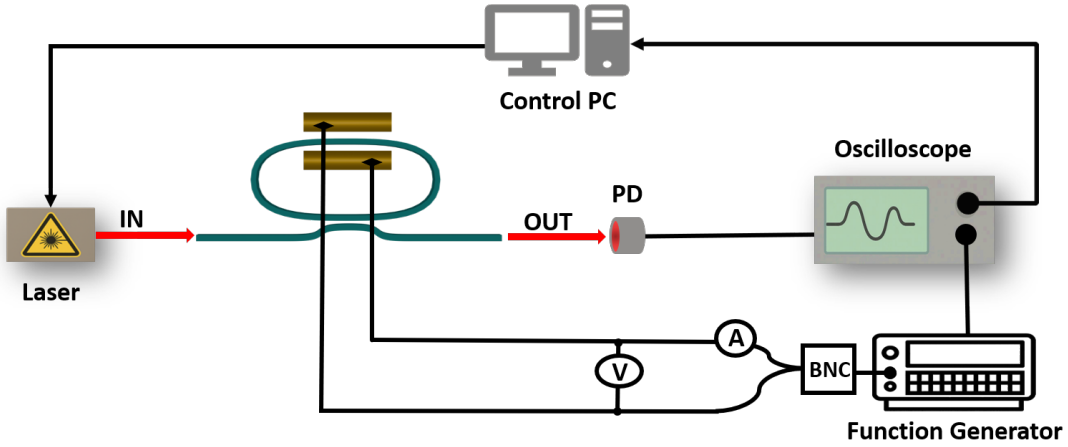

Figure 3.8: Optical transmission setup used for characterisation of tunable strip-loaded devices. For electro-optic measurements, 20 MHz function generator was used to supply a sine waveform. PD: photodetector

3.6 DC tuning

The DC tuning of the MZI and Racetrack resonator is performed using the setup shown in Figure 3.8, where the function generator is replaced with a DC power supply (Yokogawa GS610). The subsequent section provides a detailed discussion on the DC tuning of the MZI and Racetrack resonator.

3.6.1 Mach–Zehnder interferometer

The wavelength tuning of the MZI transmission spectrum is depicted in Figure 3.9. The voltage applied to the metal pad was increased by 1 V increments up to 10 V, followed by 5 V increments until reaching a maximum of 30 V. The difference between the initial and final spectra indicates a tuning range of 0.37 nm. The electro-optic tunability of MZI, derived from a linear fit, is 14.67 ± 0.64 pm/V, and a V_π of $7.4\,V \cdot cm$ is achieved, as illustrated in Figure 3.10

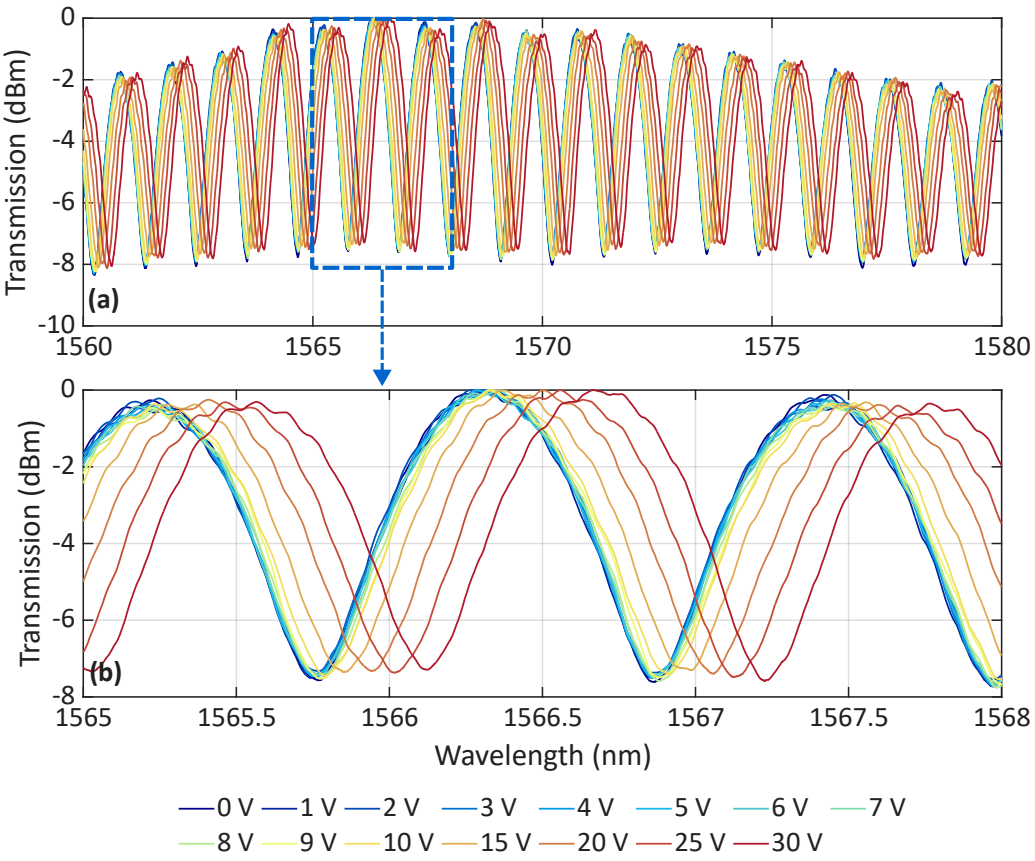

Figure 3.9: (a) Transmission spectra of the Mach–Zehnder interferometer under different applied voltages, showing a progressive redshift of the interference fringes. (b) Zoomed view of two adjacent resonances highlighting the wavelength tuning behaviour.

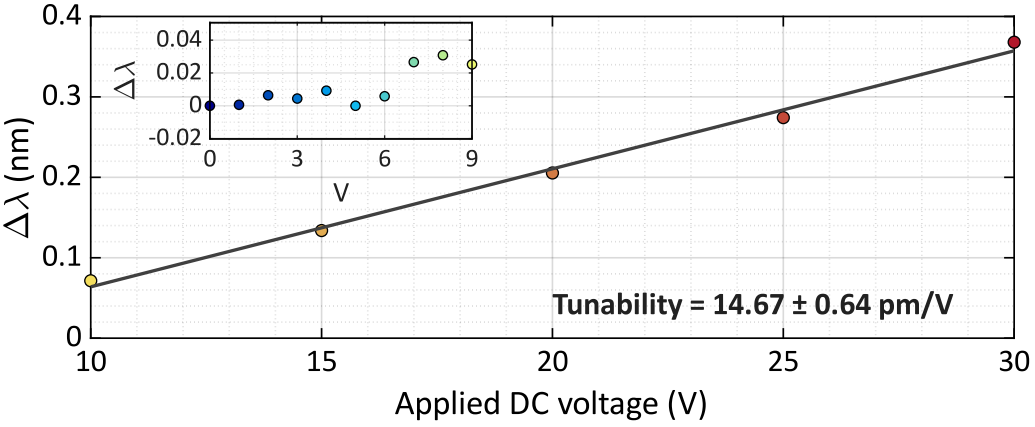

Figure 3.10: Wavelength shift of the Mach–Zehnder interferometer resonance as a function of the applied DC voltage, showing a linear electro-optic response. The extracted tunability from the linear fit is 14.67 ± 0.64 pm/V.

3.6.2 Racetrack resonator

The wavelength tuning of the racetrack transmission spectrum is taken similar to MZI, as depicted in Figure 3.11. The voltage applied to the metal pad was incrementally increased up to 110 V. The electro-optic tunability, derived from a linear fit, is determined to be 0.49 ± 0.01 pm/V, with a V_π of $35\,V \cdot cm$, as illustrated in Figure 3.12.

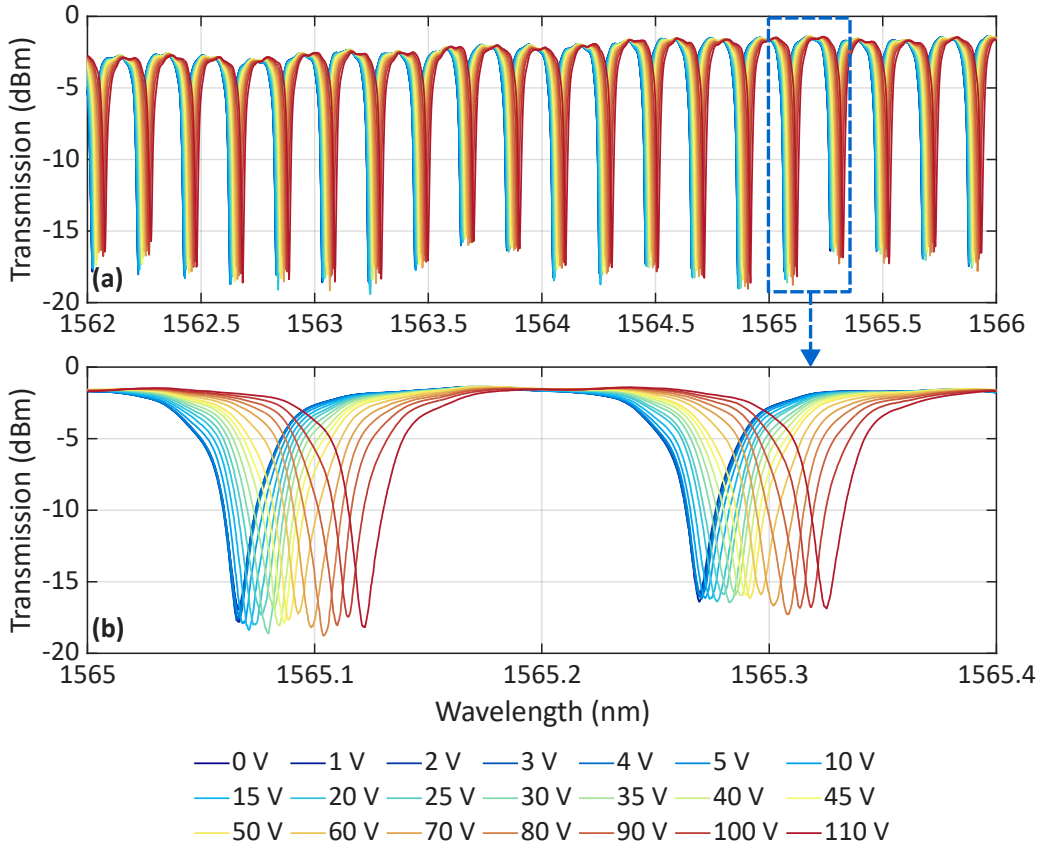

Figure 3.11: (a) Transmission spectra of the racetrack resonator under different applied voltages, showing a progressive redshift of the interference fringes. (b) Zoomed view of two adjacent resonances highlighting the wavelength tuning behaviour.

The tunability of the racetrack is notably lower than that of the MZI, due to the use of the TM mode for transmission, which employs the electro-optic tensor r_{13}, approximately three times lower than r_{33}, which is utilised in the MZI. As discussed in the previous chapter, strip-loaded guides are not suitable for resonating devices due to their large radii. Therefore, BIC based strip-loaded guides are employed to achieve compact resonant devices, along with a simplified fabrication process to achieve modulated res-

onant devices. As discussed in previous chapter, this geometry guides light for TE, so we attempted to tune the resonator under TE polarisation; however, no effective tuning was observed. This can be attributed to the fact that a significant portion of the mode field is confined within the SU-8 layer, which lacks a second order nonlinearity ($\chi^{(2)}$).

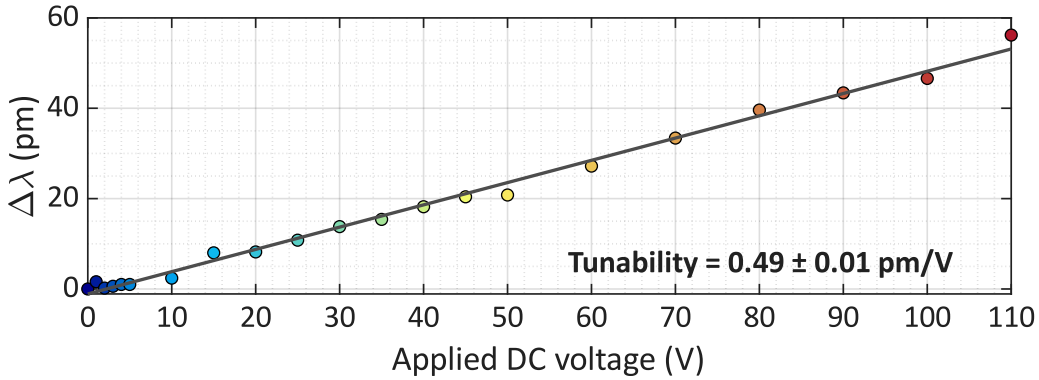

Figure 3.12: Wavelength shift of the racetrack resonator resonance as a function of the applied DC voltage, showing a linear electro-optic response. The extracted tunability from the linear fit is 0.49 ± 0.01 pm/V.

3.7 Bandwidth measurements

The bandwidth measurements were initiated by first recording the transmission spectra of the MZI and racetrack resonator, as described previously. Resonance wavelengths of approximately 1570.48 nm and 1588.23 nm were selected for the MZI and racetrack resonator, respectively. The laser wavelength was then parked at the centre of each resonance. The optical input power was maintained at a constant value of 0.35 mW. A sinusoidal electrical signal generated by a function generator, with a maximum frequency of 20 MHz, was applied to the metal electrodes of both devices with a peak-to-peak voltage of 10 V_{pp}. Figures 3.13 and 3.14 show the input and output signals measured at frequencies of 1 kHz and 5 MHz for the MZI and racetrack resonator, respectively. The optical output was detected using a Thorlabs PDA10CS photodetector operated at a fixed gain of 50 dB, corresponding to a detector bandwidth of 5 MHz. This bandwidth effectively limited the maximum measurable modulation bandwidth of the experimental setup.

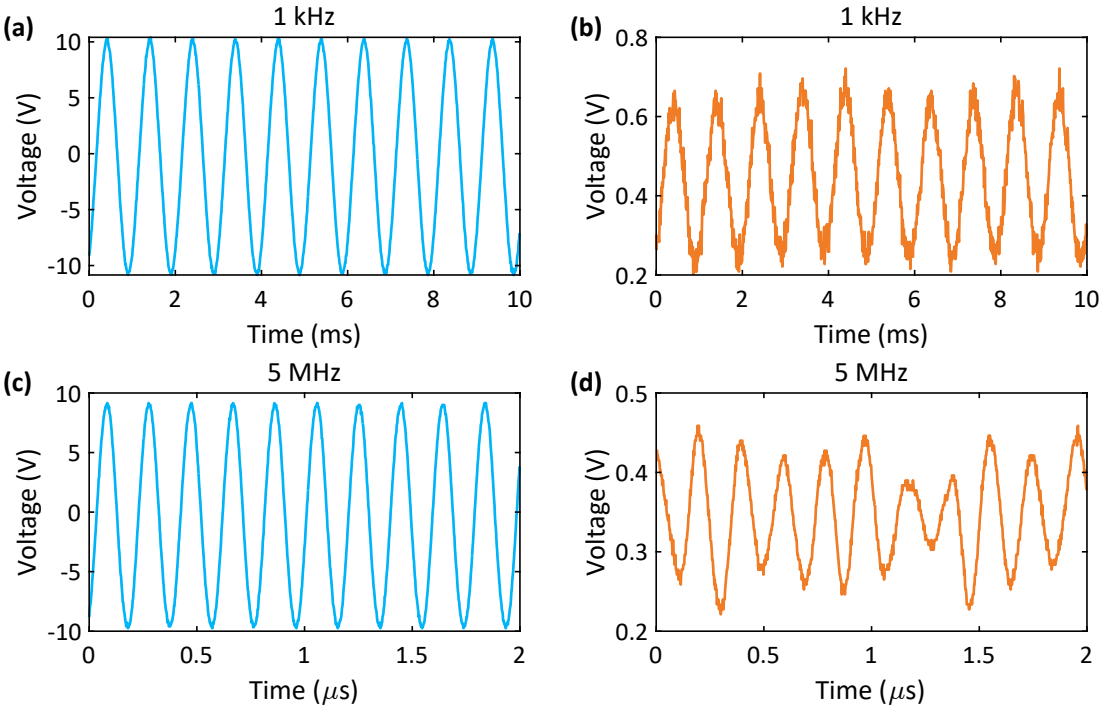

Figure 3.13: (a) Electrical 1 kHz sine-wave signal applied to the Mach–Zehnder interferometer and (b) the corresponding optical response. (c) Electrical 5 MHz input signal and (d) the corresponding optical response.

To evaluate the peak switching bandwidth of the MZI and racetrack resonator, sine waves of increasing frequency are transmitted through the metal pads. The device's tuning response time imposes a frequency limit, beyond which it cannot accurately replicate the electrical sine wave input, leading to a distortion of the modulated optical signal. A critical metric for determining the device's maximum operational frequency is the 3 dB bandwidth, which, in this context, refers to the point at which the peak-to-peak extinction of the optical signal decreases to −3 dB. The Figure 3.15(a) and 3.15(b) illustrate the peak-to-peak extinction for increasing frequencies up to 5 MHz for the MZI and racetrack resonator, respectively. The devices demonstrate satisfactory performance across the range of applied frequencies until reaching the photodetector bandwidth limit of 5 MHz. Notably, the modulation amplitude decreases at lower frequencies. This behaviour is consistent with electro-optic relaxation in lithium niobate, where mobile charge carriers partially screen the applied electric field and reduce the effective electro-optic interaction. Similar behaviour has been reported in

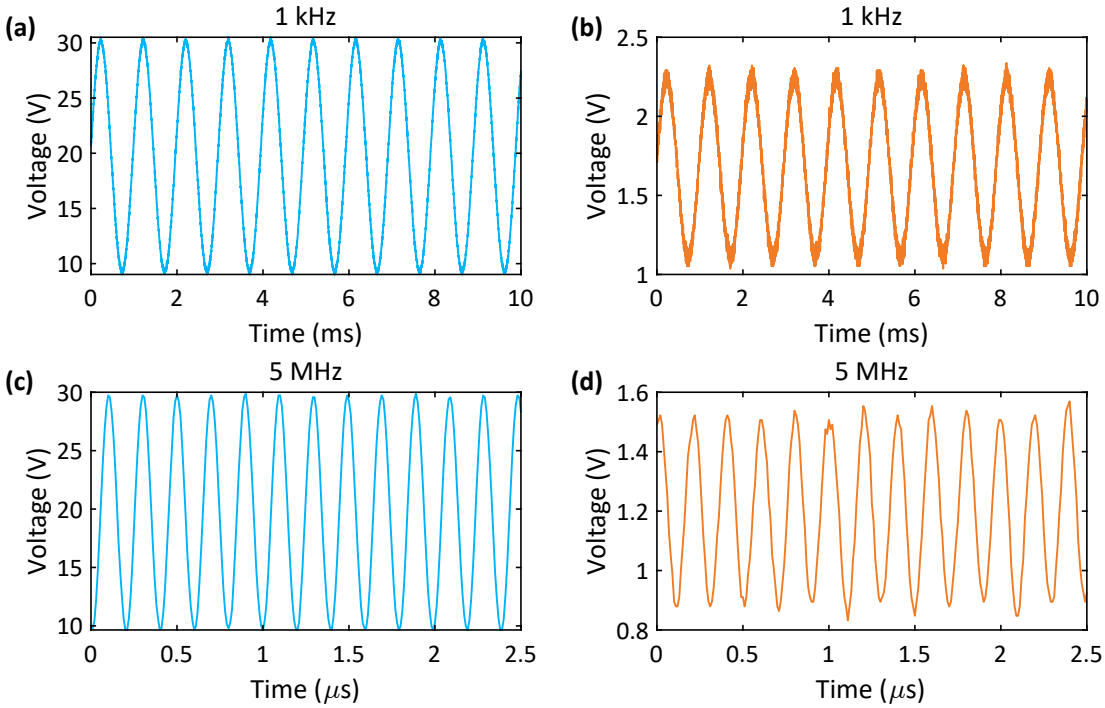

Figure 3.14: (a) Electrical 1 kHz sine-wave signal applied to the racetrack resonator and (b) the corresponding optical response. (c) Electrical 5 MHz input signal and (d) the corresponding optical response.

TFLN modulators, where significant suppression of the electro-optic response occurs below approximately 100 Hz [137]. This characteristic renders LN impractical for many low-frequency applications, necessitating the use of ubiquitous DC bias tuners in optical modulators [138]. However, thermo-optic phase shifters can be employed as an alternative [139, 140, 141, 142] to address these challenges, albeit at the expense of reduced bandwidth, increased power consumption [141], and crosstalk between phase shifters [143], making them less attractive for quantum photonics at cryogenic temperatures and optical communication systems where transmitter power consumption is a critical figure of merit. The electro-optic response is expected to improve at cryogenic temperatures because mobile charge carriers become increasingly immobilised, suppressing dielectric relaxation and reducing electric-field screening. Similar behaviour has been demonstrated in TFLN devices, where a substantial improvement in the low-frequency electro-optic response was observed at temperatures as low as 0.05 K. Furthermore, removal of the SiO_2 cladding has been shown to improve the low-frequency

electro-optic response by reducing dielectric screening effects at the LN surface, while annealing in nitrogen or oxygen can reduce defect-related charge transport, resulting in a flatter and more stable electro-optic response across a broad frequency range [137].

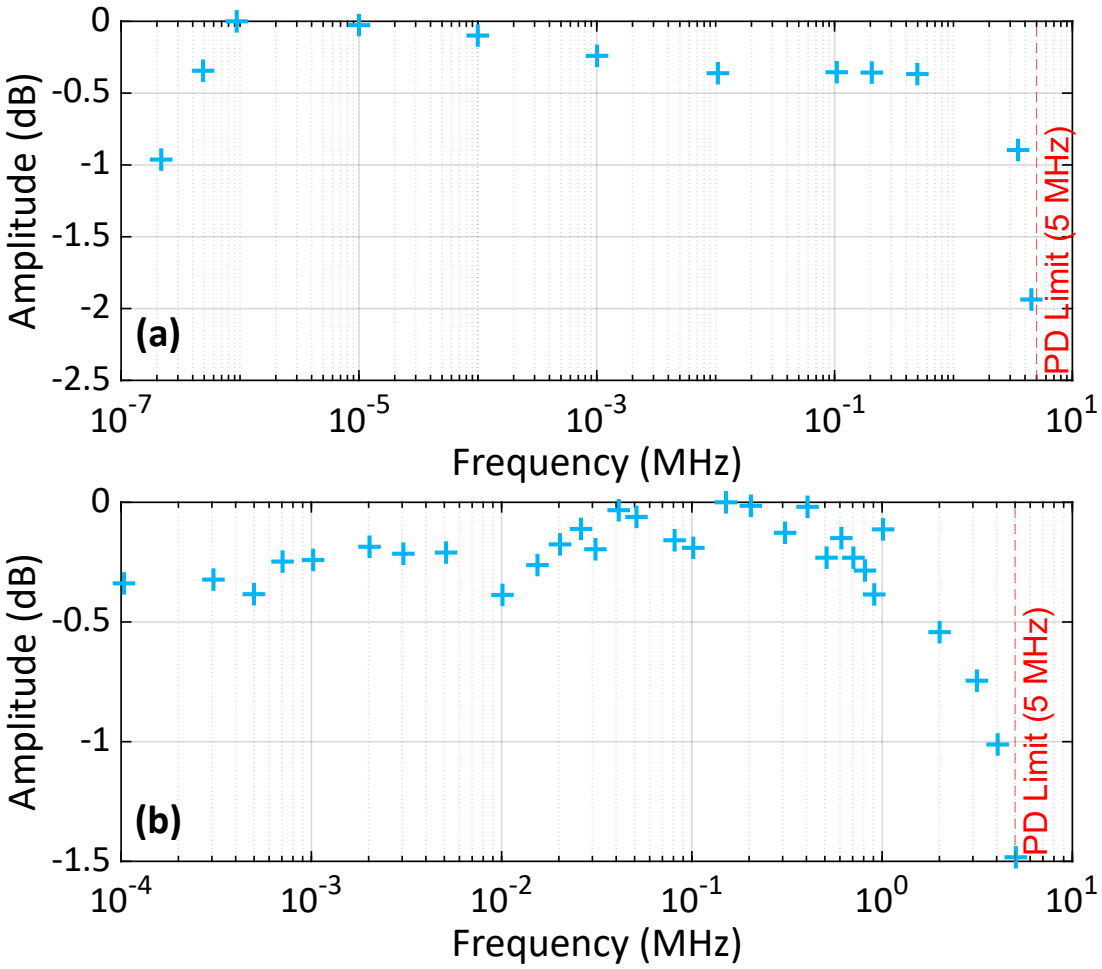

Figure 3.15: Peak-to-peak amplitude response of active strip-loaded devices, normalised to its maximum value. (a) Mach-Zehnder interferometer, (b) Racetrack resonator. PD:Photodetector

3.8 Summary

This chapter presented the development of active strip-loaded lithium niobate devices. A racetrack resonator based on BIC was demonstrated, representing, at the time of writing, the first tunable BIC-based racetrack resonator. The device exhibited an

electro-optic tunability of 0.49 pm/V, which is approximately three times lower than previously reported transfer-printed lithium niobate racetrack resonator. This reduced tunability arises from the use of a simplified fabrication process and the exploitation of the r_{13} electro-optic coefficient, which is intrinsically three times smaller than r_{33}. Despite these limitations, the results highlight the viability of low-complexity fabrication approaches for electrically tunable BIC-based resonators. Furthermore, the BIC platform enabled a reduction in bend radius from 350 μm in the strip-loaded MZI to 94 μm in the racetrack resonator, highlighting its potential for significantly enhanced integration density in strip-loaded lithium niobate photonic circuits

In contrast, the strip-loaded MZI leverages the r_{33} electro-optic coefficient, achieving a tunability of 14.67 pm/V, with electro-optic performance comparable to previously reported strip-loaded lithium niobate devices. Together, these demonstrated devices pave the way towards scalable and CMOS-compatible photonic integrated circuits, offering a compelling balance between fabrication simplicity and electro-optic performance.

Chapter 4

Hybrid integration of GaN and SiN

This chapter presents the development of a hybrid integration approach for suspended GaN membranes on silicon nitride (SiN) waveguides. It begins by outlining the motivation for hybrid integration of photonic materials. This is followed by the simulation and fabrication of SiN receiver devices and suspended GaN membranes, respectively. The chapter then describes the micro-transfer printing process used for integration, and concludes with the optical characterisation of the GaN membranes integrated on SiN waveguides.

4.1 Introduction

As integrated photonics technology has advanced, photonic systems have become faster, more complex, and increasingly capable, enabling a wide range of applications including telecommunications [144], healthcare [145], neuromorphic computing [146], sensing [147], and quantum information processing [148]. However, the limitations of monolithic photonic platforms have become increasingly apparent, as no single material system can simultaneously provide low-loss optical guiding, efficient light emission and detection, and strong electro-optic tunability. Consequently, the growing demand for sophisticated and multifunctional photonic systems cannot be met using a single

material platform alone [149].

To address these limitations, hybrid integration has emerged as a promising approach that leverages the complementary strengths of multiple photonic material platforms [149]. For example, silicon and silicon nitride (SiN) offer excellent scalability and low-loss waveguiding [150, 151, 152, 153], III–V semiconductors enable efficient light sources and photo-detectors [154, 155], and materials with strong second-order non-linearities, such as lithium niobate (LN), provide high-performance electro-optic modulation [37, 36]. By combining these complementary materials within a single photonic system, hybrid integration enables functionalities and performance levels that are not achievable using monolithic approaches. Among passive photonic platforms, SiN is an excellent choice due to its exceptional optical properties, including a wide transparency window spanning from the visible to the mid-infrared, low propagation loss, a low thermo-optic coefficient, and the absence of two-photon absorption [71, 72]. In addition, SiN exhibits excellent compatibility with CMOS fabrication technology, enabling stable and scalable photonic manufacturing [71, 79]. Low-loss SiN waveguides have enabled the realisation of high-quality-factor resonators and dense photonic integration, making SiN a highly attractive platform for large-scale photonic circuits [151, 150]. However, SiN is intrinsically a passive material and lacks active functionalities such as light emission, photodetection, and electro-optic modulation, which limits its ability to serve as a fully functional stand-alone photonic platform. In contrast, gallium nitride (GaN), a wide-bandgap III–V semiconductor, offers a complementary set of properties that can overcome many of the limitations of passive platforms such as SiN. GaN exhibits a refractive index of approximately 2.3 at telecommunication wavelengths and a wide transparency range extending from the ultraviolet to the mid-infrared. Owing to its non-centrosymmetric crystal structure, GaN possesses both second- and third-order optical non-linearities, which can be exploited for non-linear optical processes including frequency conversion, second-harmonic generation, and four-wave mixing [70]. Recent developments in monolithic GaN photonic platforms have demonstrated waveguides with propagation losses on the order of a few dB/cm and moderate optical quality factors [70, 156]. Nevertheless, bulk GaN substrates remain expensive and are typi-

cally available only at small wafer scales. Moreover, hetero-epitaxial growth of GaN on silicon or sapphire substrates introduces a high density of dislocations and significant residual stress [157]. As a consequence, the fabrication of low-loss, large-scale passive photonic circuits in GaN remains challenging, limiting the scalability of purely monolithic GaN photonic platforms.

These limitations motivate the heterogenous integration of GaN with low-loss passive photonic platforms such as SiN, allowing GaN to be used selectively for active and non-linear functionality while SiN provides efficient optical routing. As discussed in previous chapters, LN offers excellent electro-optic performance and has been widely used for modulator applications. However, its fabrication challenges, including etching complexity and limited CMOS compatibility, make large-scale integration challenging [41, 43, 44]. For applications where moderate electro-optic functionality is sufficient, GaN provides a practical alternative, enabling compact device implementations while offering non-linear and optoelectronic capabilities alongside mature and scalable fabrication processes well developed through its widespread use in LED technologies [62, 64]. The hybrid integration of GaN and SiN therefore enables the combination of low-loss optical routing with active functionality. In this work, we present GaN ring resonator membranes integrated on a SiN photonic platform, representing a promising route toward compact, low-loss, and scalable multifunctional integrated photonic systems.

4.2 Receiver chip

4.2.1 Simulation

The FDE simulations of SiN waveguides are performed using Tidy3D, similar to the strip-loaded waveguides discussed in Chapter 2. The simulations use frequency-dependent refractive index data for SiN and SiO_2 and are carried out at an operating wavelength of 1.55 μm. The waveguide geometry consists of a 300 nm thick SiN layer, while the waveguide width is swept from 1 μm to 5 μm as shown in Figure 4.1.

Figure 4.2 shows the effective refractive index as a function of the waveguide width. The solid lines correspond to TE modes, whereas the dashed lines represent TM modes.

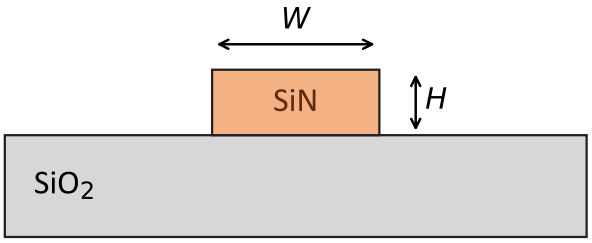

Figure 4.1: Schematic diagram of SiN waveguide, where W is the waveguide width (varied from $1-5\,\mu$m) and H is the fixed height of 300 nm.

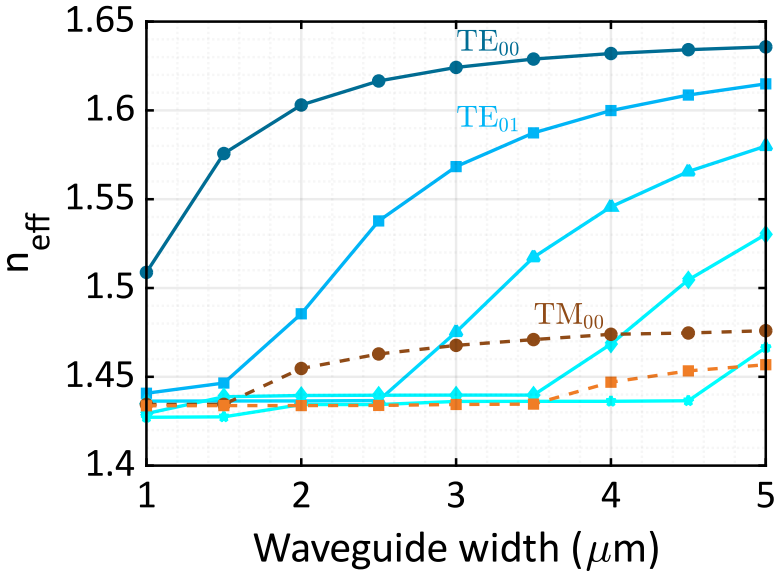

Figure 4.2: Mode effective indices for TE and TM polarisations as a function of waveguide width, with the SiN layer thickness fixed at 300 nm.

As the waveguide width increases, the waveguide supports a larger number of guided modes, and the effective refractive index increases due to improved optical confinement within the SiN core. The TM modes exhibit significantly lower effective indices compared to the TE modes, indicating weaker confinement and higher overlap with the cladding. Improved TM confinement could be achieved by increasing the SiN thickness due to the vertical field distribution; however, for the current geometry, the TM modes remain close to cut-off. The waveguide width of 1.5 μm supports single-mode operation, beyond which the waveguide becomes multimode. The waveguide width is considered

as a free design parameter and should be chosen to be larger than the resolution limit of the employed lithography process.

4.2.2 Fabrication

The SiN waveguides were fabricated using a pre-deposited 300 nm thick SiN layer on top of a 3 μm thick SiO_2 wafer. The fabrication process is shown in Figure 4.3, which began with standard solvent cleaning, followed by spin-coating of S1805 positive photoresist. A softbake was performed at 95 °C for 1 minute. Waveguide patterns were exposed using direct-write laser lithography, similar to the previous chapter. After exposure, the resist was developed in a 1:1 mixture of MicroDeveloper and deionised water for 30s to reveal the lithographic patterns. Since a positive resist was used, the exposed regions were removed during development, in contrast to the negative SU-8 resist used in the previous chapter.

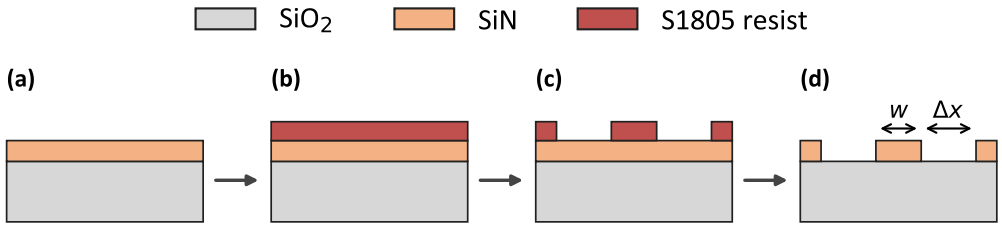

Figure 4.3: Fabrication process of SiN waveguides: (a) solvent cleaning of the substrate, (b) spin coating of the photoresist, (c) waveguide patterning and development, and (d) transfer of the pattern into the SiN layer via RIE. Here, W denotes the waveguide width and Δx represents the trench width.

The waveguide geometry was defined by exposing the trench regions on either side of the waveguide core. The remaining resist served as an etch mask during reactive ion etching (RIE), while etching away the trench pattern and resulting in fully etched SiN waveguides. A trench spacing ($\Delta x = 20\,\mu$m) was used to ensure uniform etching and isolation of the waveguide core from the surrounding SiN, which is required for proper optical confinement. SiN was etched using SF_6 gas in (RIE) process, achieving an etch rate of approximately 74 nm/min. After etching, the remaining resist was stripped using a Matrix asher. Finally, the fabricated waveguides were cleaved to enable edge

coupling for optical transmission. Optical microscope images of the fabricated SiN receiver chip are shown in Figure 4.4, showing receivers with waveguide widths of 1, 1.5, 2, 2.5, and 3 μm. Enlarged views of receivers with 1 μm and 2 μm waveguide widths are also presented.

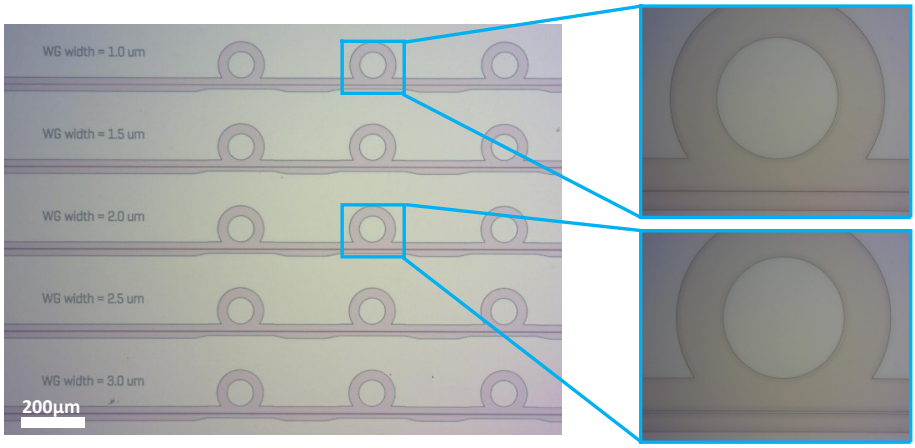

Figure 4.4: Optical microscope images of fabricated SiN receivers with waveguide widths ranging from 1 to 3 μm, including zoomed-in views of 1 μm and 2 μm waveguides.

4.3 Donor chip

4.3.1 Simulation

Mode analysis of the hybrid waveguide structure was performed using Tidy3D, following an approach similar to that employed for the receiver simulation. A schematic of the hybrid device is presented in Figure 4.5. The SiN layer thickness was fixed at approximately 300 nm. As discussed earlier, SiN waveguides with widths of 1 μm and 1.5 μm support single-mode operation; therefore, both widths were selected. The GaN substrate consists of an 800 nm-thick GaN layer on top of a 50 nm-thick AlN layer. To investigate mode confinement, the GaN thickness was varied from a fully etched total thickness of 850 nm (including 50 nm of AlN) to partially etched heights of 600 nm, 400 nm, and 200 nm as illustrated in Figure 4.5. In addition, the GaN waveguide width was swept from 0.5 μm to 2 μm. These variations were analysed to evaluate the modal

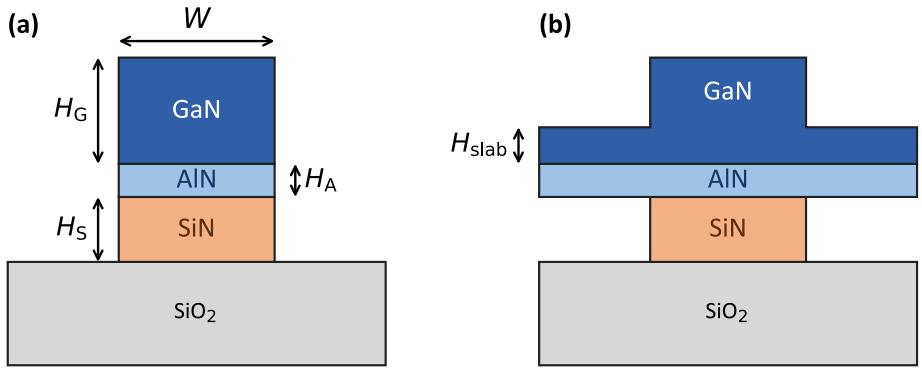

Figure 4.5: Schematic diagrams of the hybrid GaN-on-SiN waveguide structures: (a) fully etched GaN waveguide and (b) partially etched GaN waveguide. The waveguide width W is varied from 0.5 μm to 2 μm for the GaN layer. H_G denotes the GaN layer height, H_A the aluminium nitride (AlN) layer height, H_{slab} the GaN slab height in partially etched devices, and H_S the SiN layer height.

behaviour and confinement in waveguide bends with a radius of 60 μm.

Figure 4.6 shows the effective mode indices of the hybrid GaN-on-SiN waveguide for different etch configurations. In cases (a) and (b), where the slab thickness is 600 nm and the GaN ridge height is 200 nm, the optical mode is primarily supported by the thick slab region. As a result, lateral confinement is weak and the structure becomes multimode even for relatively small GaN widths. For the configurations shown in (c) and (d), where both the GaN ridge and slab thicknesses are 400 nm, the separation between the fundamental and higher-order modes increases; however, the lateral confinement remains limited due to the still relatively thick slab. In contrast, for cases (e) and (f), where the GaN height is 600 nm and the slab thickness is reduced to 200 nm, both the fundamental TE_{00} and TM_{00} modes are well confined within the GaN ridge. In this configuration, the effective indices of higher-order modes decrease as these modes become weakly guided, resulting in an extended single-mode operating regime. For the fully etched GaN structure, the optical confinement is strongest compared to all other configurations, and the effective indices of higher-order modes are pushed further down. Overall, both the partially etched GaN structure with a height of 600 nm and the fully etched GaN geometry provide good confinement of the fundamental modes. In this work, the partially etched GaN configuration with a 600 nm GaN height is selected, as

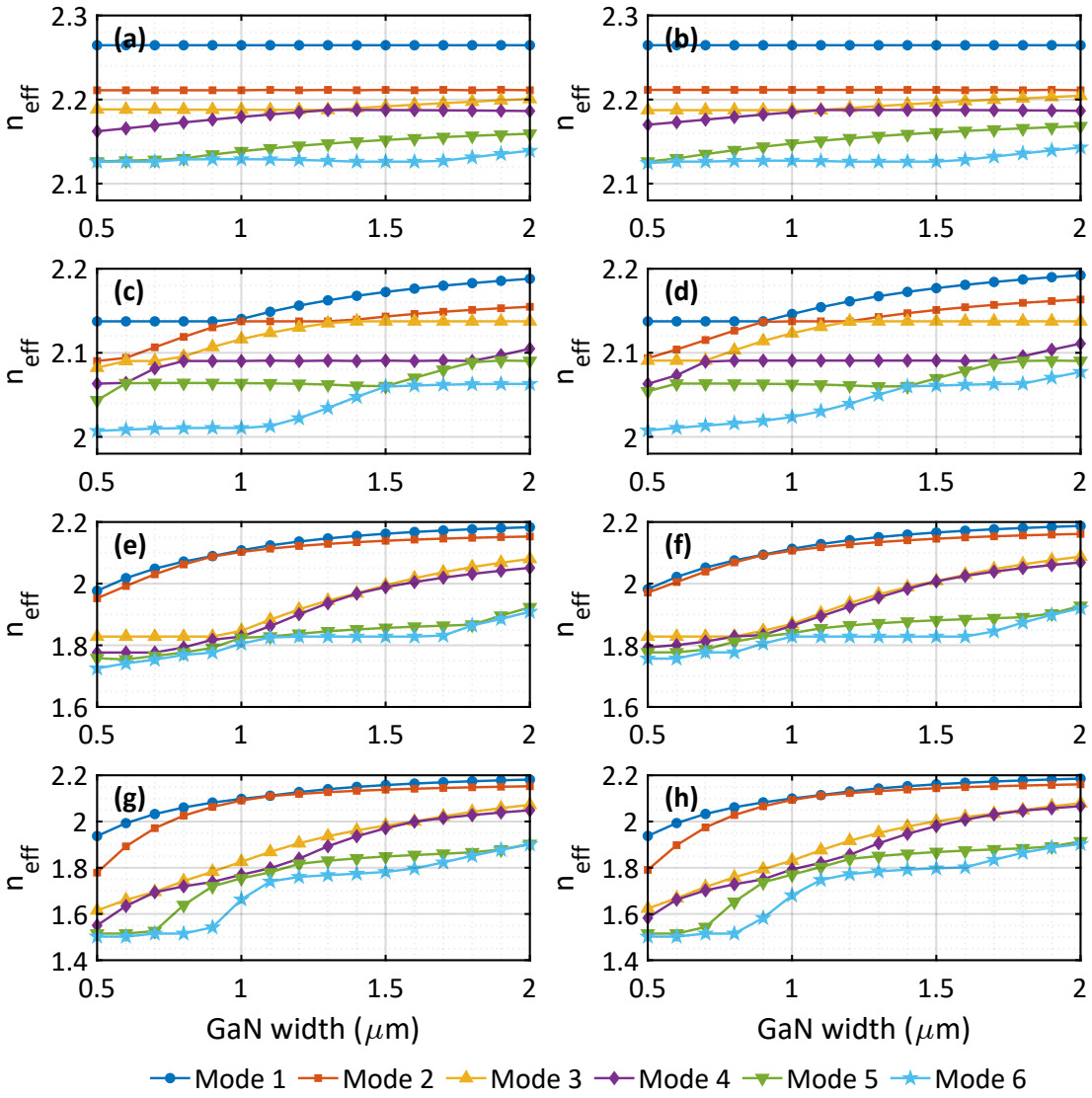

Figure 4.6: Effective mode index as a function of the GaN waveguide width for the hybrid GaN-on-SiN waveguides shown in Fig. 4.5. The GaN width is varied from 0.5 μm to 2 μm by adjusting the slab thickness. Two SiN waveguide widths are considered: 1.0 μm and 1.5 μm. The left column corresponds to a SiN width of 1.0 μm for the following cases: (a) GaN height of 200 nm with a slab height of 600 nm; (c) GaN and slab heights of 400 nm; (e) GaN height of 600 nm with a slab height of 200 nm; and (g) fully etched GaN down to the AlN layer. The right column shows the corresponding structures for a SiN width of 1.5 μm, labelled as (b), (d), (f), and (h), respectively.

it is expected to reduce sidewall scattering losses compared to the fully etched case. In addition, partially etched geometries are more favourable for future active devices, as they enable improved electrical and optical mode overlap. The mode confinement for SiN waveguide widths of 1.0 μm and 1.5 μm is found to be similar, as confirmed by the simulated mode profiles shown in Figure 4.7 and the confinement values summarised in Table 4.1. For both polarisations, the majority of the optical field remains confined within the GaN layer. A modest increase in field confinement is observed in the TE_0 mode when increasing the SiN width from 3.5% to 4.9%, while for the TM_0 mode the confinement increases from 6.6% to approximately 8.1%. The slightly higher confinement in the SiN layer for the TM mode arises from its vertical mode profile.

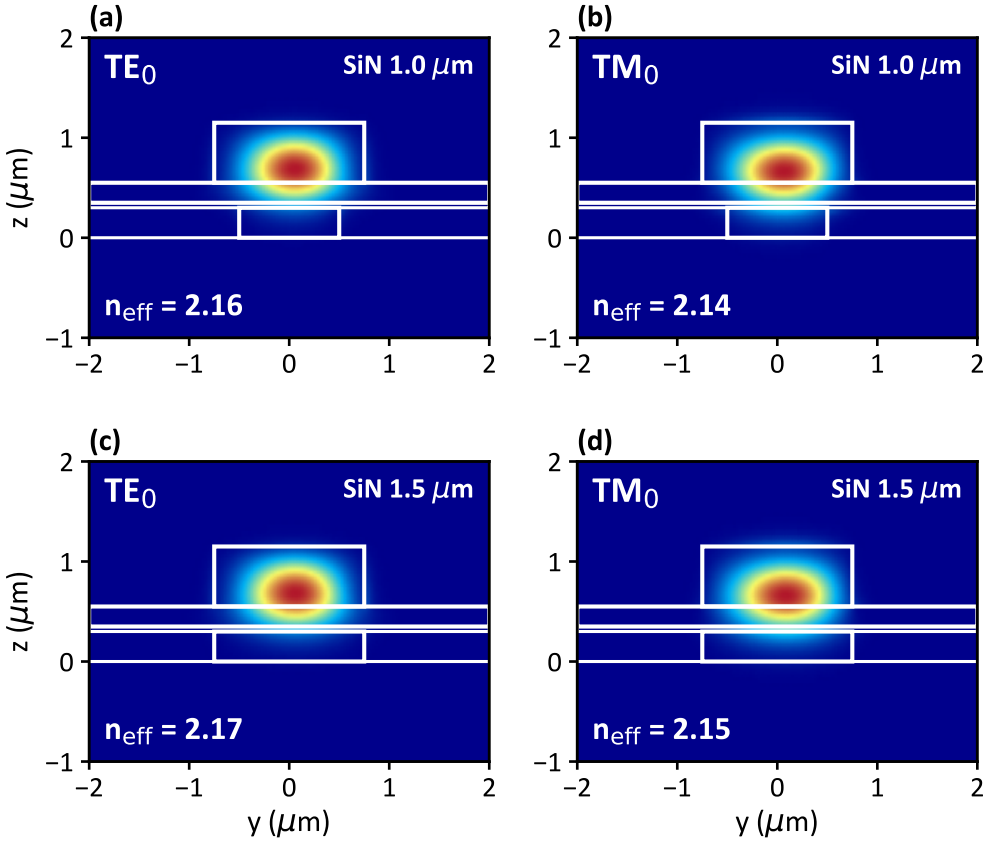

Figure 4.7: Mode profiles of both TE and TM polarisations for hybrid GaN-on-SiN waveguide at 1550 nm, for SiN waveguide widths of (a, b) 1.0 μm and (c, d) 1.5 μm.

Table 4.1: Optical power confinement in different material layers for the fundamental TE_0 and TM_0 modes of the hybrid GaN-on-SiN waveguides.

Panel	SiN width	Mode	SiN (%)	AlN (%)	GaN (%)
(a)	1.0 μm	TE_0	3.5	2.5	90.8
(b)	1.0 μm	TM_0	6.6	3.3	85.2
(c)	1.5 μm	TE_0	4.9	2.8	89.5
(d)	1.5 μm	TM_0	8.1	3.7	84.1

4.3.2 Design

As discussed in the simulation section, hybrid GaN-on-SiN waveguides transition to multimode operation as the waveguide width increases, making single-mode operation difficult for wider geometries. To explore this trade-off, the waveguide width was iterated from 1.2 μm to 2.0 μm with a step size of 0.2 μm, while keeping the bend radius fixed at 60 μm.

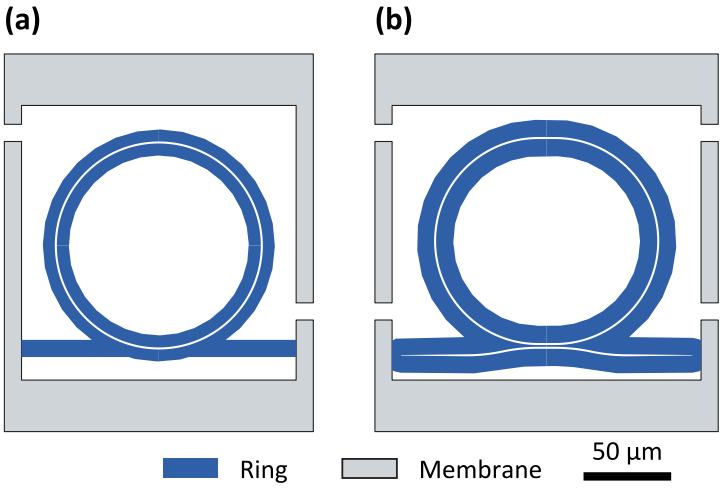

Figure 4.8: GaN suspended membranes: (a) isolated ring with two anchors, and (b) bus-coupled ring with four anchors.

The GaN suspended membranes, shown in Figure 4.8, follow two design approaches: (i) isolated rings and (ii) bus-coupled membrane rings. In addition to rings , racetrack geometries with a straight section length of 10 μm were also implemented. For the coupling configuration, isolated rings rely on vertical evanescent coupling to the underlying SiN waveguide. In contrast, bus-coupled rings employ a tapered GaN bus waveguide

with length and width of 40 μm and 0.3 μm, respectively to enable mode transition from the SiN waveguide into the GaN bus waveguide, from which light evanescently couples into the GaN ring resonator. The coupling strength between the bus waveguide and the ring resonator is primarily determined by the coupling gap, interaction length, and modal overlap between the guided modes. A fixed coupling gap of 1 μm was maintained across all devices, while the racetrack resonators additionally employed a coupling length of 10 μm.

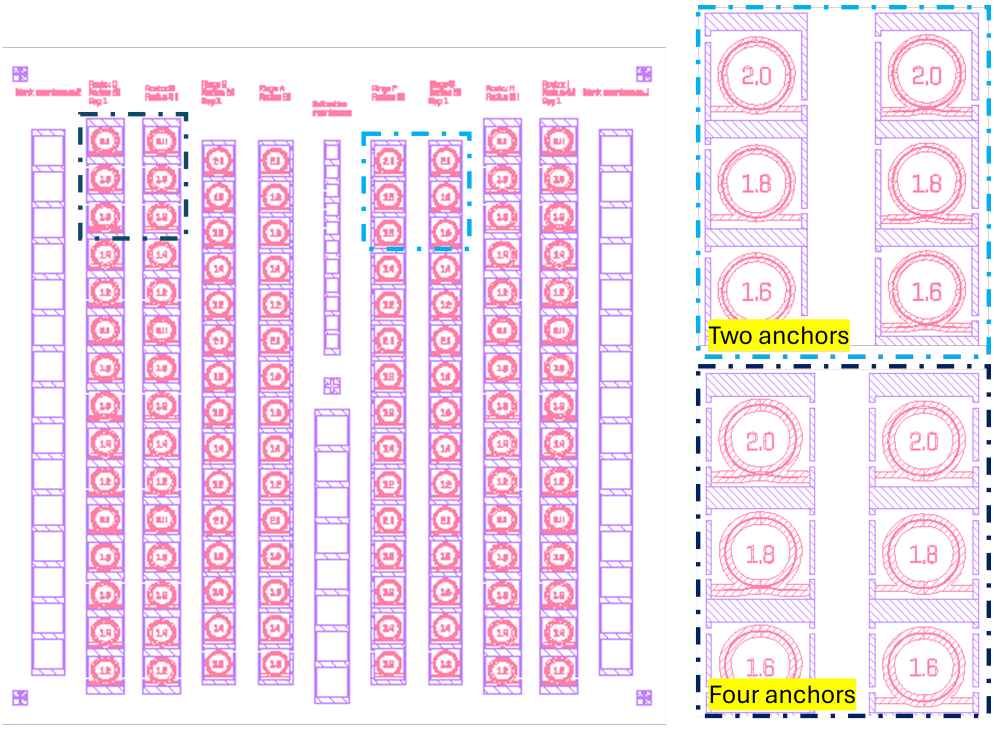

Figure 4.9: GDS mask of GaN membranes, highlighting the detailed membrane geometries implemented with two and four anchor supports.

As the GaN membranes are intended for transfer printing onto a SiN receiver chip, their dimensions and anchor configurations were chosen to facilitate membrane printing. The membrane dimensions were chosen as $160 \times 160\,\mu\text{m}^2$ for ring devices, and $180 \times 160\,\mu\text{m}^2$ for racetrack geometries to accommodate the extended straight sections. Although these dimensions are determined by the footprint of the ring and racetrack resonators rather than by the transfer printing process itself, which has been demonstrated for considerably smaller structures including photonic crystal cavity membranes

and semiconductor nanowires [158, 159]. The GaN membranes were designed with either four or two anchoring points to maintain their attachment to the surrounding GaN layer once the underlying silicon is removed. The left four columns employ four-anchor membranes, where the first and third columns incorporate bus-coupled ring resonators and the second and fourth include isolated rings. The right four columns follow the same arrangement using two-anchor membranes. The first two and last two columns incorporate racetrack resonator geometries. Two-anchor designs facilitate easier membrane pick-up during transfer printing, whereas four-anchor designs improve stability but make membrane release more challenging. The membrane GDS design was produced by my colleague, Dr. Jack Smith.

4.3.3 Fabrication of free-standing GaN membranes

The fabrication of free-standing GaN membranes begins with the preparation of the donor chip. The GaN wafer is first cleaved into small pieces and subsequently cleaned using standard solvent cleaning procedures to remove organic and particulate contaminants, ensuring a clean surface for further processing. The fabrication process consists of two main stages: (i) fabrication of GaN ring resonator structures and (ii) fabrication of suspended GaN membranes. A schematic overview of the complete fabrication sequence is shown in Figure 4.10.

The fabrication of the ring resonators starts with the deposition of 300 nm SiO_2 hard mask, deposited at a rate of 43 nm/min. Subsequently, S8105 photoresist is spin-coated onto the sample and soft-baked at 95 °C for 1 min. The ring resonator patterns were defined using standard photolithography. After exposure, the sample is developed for 30 s, revealing the lithographically defined features in the photoresist. The resist pattern acts as a mask for SiO_2 etching, Approximately 350 nm of SiO_2 is etched at an etch rate of 41 nm/min, with an intentional over-etch applied to ensure complete removal of SiO_2 in the exposed regions as shown in Figure 4.11(a). Following the SiO_2 etch, the remaining photoresist is removed. SiO_2 acts as hard mask to transfer pattern in GaN layer using RIE-ICP (see Figure 4.11(b)) using a Cl_2/Ar chemistry (30/10 sccm) at 20 mTorr, with 400 W ICP coil power and 200 W platen power. Approximately

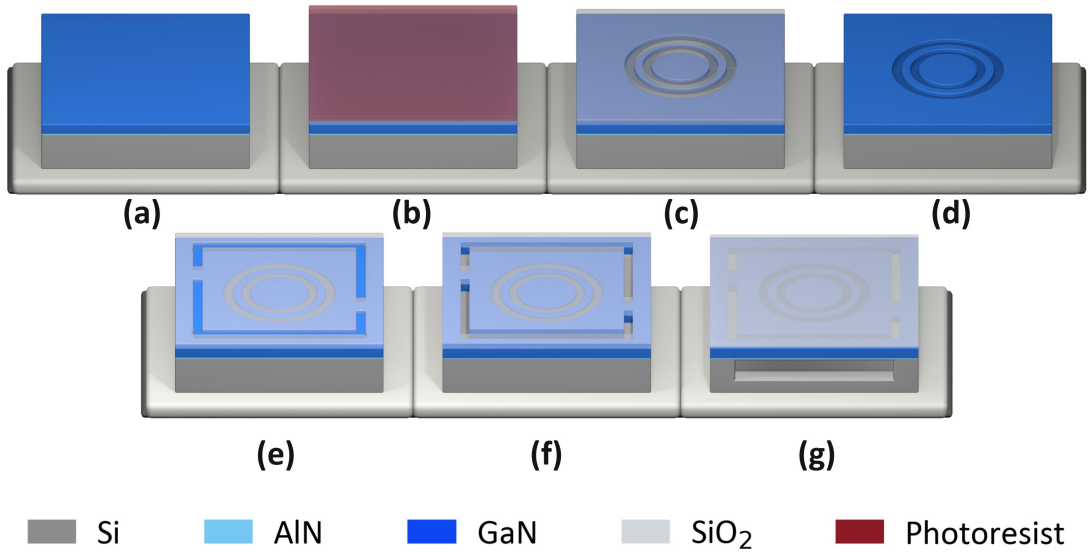

Figure 4.10: Schematic illustration of the fabrication process for a suspended GaN membrane: (a) GaN-on-silicon sample; (b) SiO_2 deposition followed by resist spin coating; (c) ring pattern definition and RIE; (d) ICP etching of the ring structures; (e) membrane pattern definition and RIE; (f) ICP etching of the membrane layer; and (g) silicon etching, followed by protective silica deposition and KOH under-etching to release the suspended GaN membrane.

600 nm of GaN is etched at a rate of 400 nm/min.

Following the fabrication of the ring resonators, the suspended membrane structures are defined. A thicker SiO_2 mask layer with a thickness of approximately 1 μm is deposited, followed by spin-coating of S1805 photoresist. The membrane patterns are then defined using photolithography, with careful alignment to the previously fabricated resonator structures to ensure accurate overlay. After exposure and development, the SiO_2 membrane mask is etched using RIE to a depth of approximately 1.1 μm to ensure complete removal of the mask in the exposed regions as shown in Figure 4.11(c). The photoresist is subsequently stripped, and the sample undergoes a second ICP etching step, during which the GaN layer is fully etched through to define the membrane boundaries using same ICP-RIE recipe for 2 min and 30 s as depicted in Figure 4.11(d). To enable membrane release, the underlying sacrificial SiO_2 layer with a thickness of approximately $2-3\,\mu$m is selectively removed as shown in Figure 4.11(e). An additional SiO_2 layer with a thickness of approximately 1 μm is then deposited on top of the sample

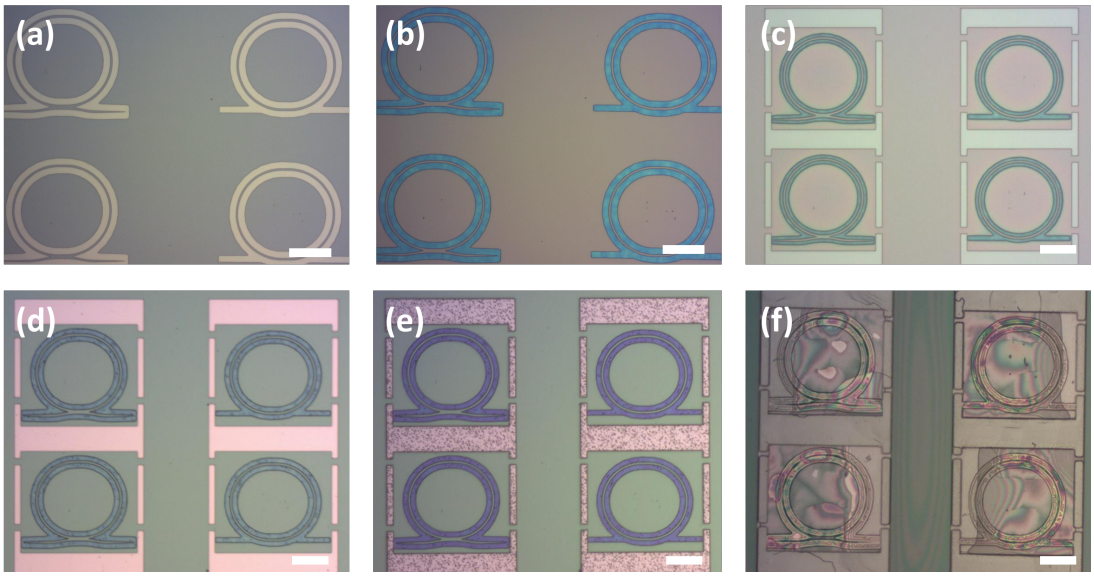

Figure 4.11: Optical microscope images of GaN membrane devices: (a) lithography and RIE of ring device; (b) ICP etching of ring devices; (c) lithography and RIE of the membrane layer; (d) ICP etching of the membrane layer; (e) silica etching; and (f) KOH under-etching resulting in suspended GaN membranes. All scale bars correspond to 50 μm.

to protect the ring resonator structures during wet chemical etching. Finally, a KOH wet etch (40 wt% KOH at approximately 85 °C for ∼1 h) was used to undercut the underlying silicon sacrificial layer and release the free-standing GaN membranes, as shown in Figure 4.11(e). KOH is a strongly anisotropic silicon etchant, with the etch rate depending on crystallographic orientation. The exposed Si(110) planes beneath the membrane are preferentially etched, while the Si(111) substrate is etched much more slowly, thereby defining the undercut geometry. After this step, the membranes are fully suspended and ready for pickup and transfer on SiN receiver chip.

4.4 Hybrid integration through micro-transfer printing

4.4.1 Transfer printing system

Micro-transfer printing was carried out using a custom, in-house–built transfer printing system [160]. An image of the transfer printing system is shown in Figure 4.12. The system consists of four main components: (i) a mechanical frame, (ii) a translation

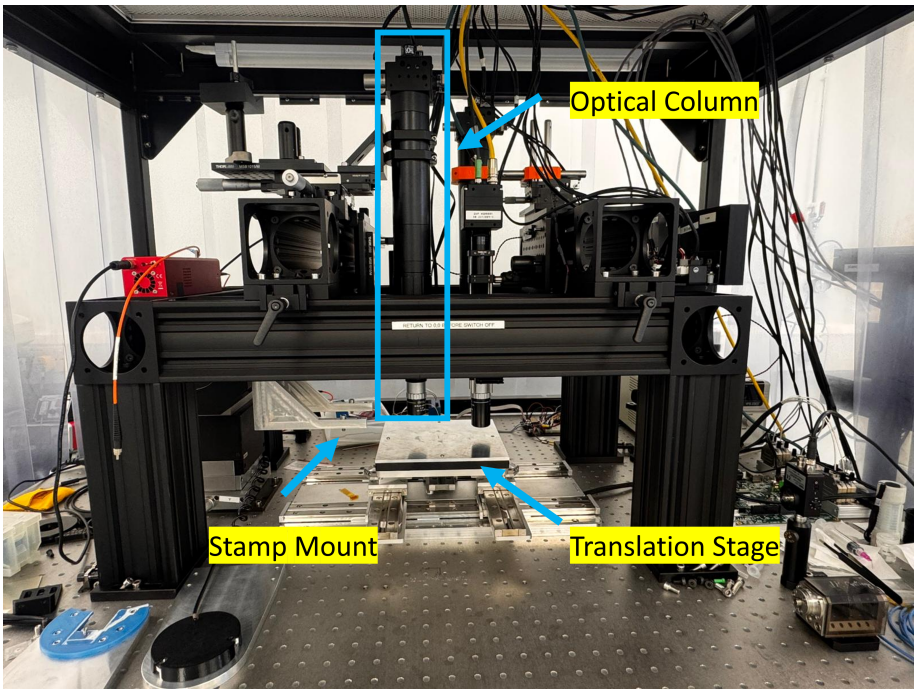

Figure 4.12: Transfer printing setup.

stage, (iii) a stamp system, and (iv) an optical vision system.

The mechanical frame is constructed from 95 mm aluminium extrusion rails (Thorlabs), providing high structural rigidity while offering a wide range of modular mounting options. This modular design allows the system to accommodate different microscope configurations, enabling both coarse alignment using global alignment markers and fine, local alignment of suspended micro- and nanoscale devices. High-precision positioning during the transfer printing process is achieved using a SmarACT translation stage, which provides motion along multiple axes with nanometre-scale accuracy and precision. The stage allows controlled movement over an area of approximately $200 \times 200\,\mathrm{mm}^2$, with programmable translation speeds ranging from $0.1\,\mu\mathrm{m\,s}^{-1}$ to $10{,}000\,\mu\mathrm{m\,s}^{-1}$. This wide range of motion speeds enables precise control of the mechanical forces applied during both pick-up and release steps of the transfer printing process.

The stamp system operates independently of the translation stage and is designed to accommodate polydimethylsiloxane (PDMS) stamps mounted on 1-inch-diameter glass

slides. The stamp can be vacuum-mounted to ensure a flat and mechanically stable configuration relative to the substrate. Fine positioning of the stamp with respect to the optical microscope is achieved using a three-axis translation stage, allowing precise control during device alignment and transfer. The vision system is based on an Optem Fusion optical microscope (Qioptiq), equipped with motorised zoom and focus capabilities. These motorised functions enable partial automation of critical steps in the transfer printing process. During device transfer, the stamp may be positioned several millimetres above the substrate to prevent accidental contact and damage. At such distances, the stamp geometry is no longer visible within the microscope field of view, necessitating frequent focus adjustments to verify successful device pick-up and to monitor the initial contact between the stamp and the target substrate. The automated zoom and focus capabilities of the microscope facilitate these adjustments, allowing the system to accommodate suspended membranes with different lateral dimensions while maintaining consistent alignment performance relative to predefined alignment markers.

4.4.2 Transfer printing process

The micro transfer printing process is illustrated in Figure 4.13 which begins with mounting both the receiver and donor chips onto the translation stage. After mounting, the PDMS stamp is aligned with the optical microscope column to establish a common reference frame for subsequent alignment steps. Once the system alignment is completed, the receiver chip is first located under the microscope, and the position of the target receiver device is recorded. The translation stage is then moved to locate the donor chip.

After identifying the donor chip, a selected suspended GaN membrane is aligned beneath the PDMS stamp. During this step, the PDMS stamp is positioned slightly above the donor chip surface. The stamp remains fixed while the translation stage is slowly moved upward, bringing the donor chip into contact with the PDMS stamp. As contact is established, the stamp is compressed, resulting in deformation of PDMS stamp such that the roof of the stamp achieves full contact with the GaN membrane. Sufficient

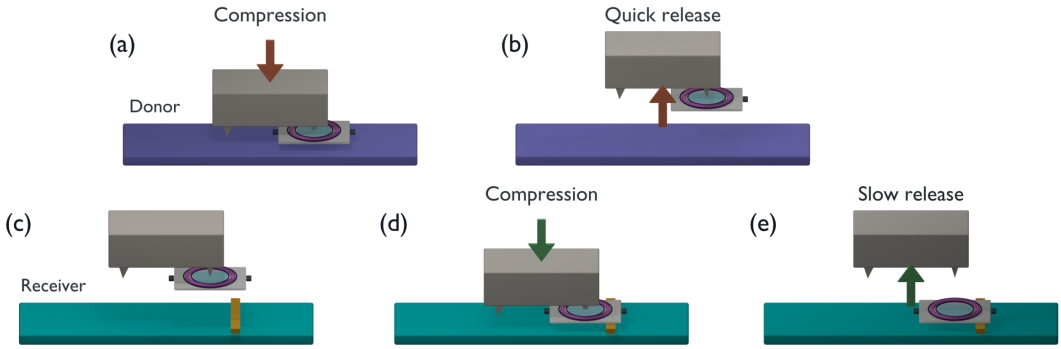

Figure 4.13: Micro-transfer printing process of a suspended GaN membrane onto a SiN waveguide.

compression is verified optically through the transparent PDMS stamp, where the compressed regions appear out of focus when full contact is achieved. A rapid retraction step is then performed to pick up the suspended GaN membrane from the silicon donor substrate, as shown in Figure 4.13(b). Following successful pick-up, the GaN membrane is transferred to the receiver chip and aligned with nanometre-scale precision using predefined alignment markers. The membrane is then brought into contact with the SiN waveguide on the receiver substrate. Finally, the GaN membrane is released by slowly retracting the PDMS stamp, as shown in Figure 4.13(d). This release process exploits the rate-dependent adhesion behaviour of viscoelastic polymers such as PDMS, whereby slower separation speeds result in lower energy release rates, enabling controlled and deterministic release of the transferred membrane [161, 162, 163]. A lateral shear velocity of approximately 8 mm/s was used during pick-up and a stamp withdrawal rate of approximately 0.05 μm/s during release [159]. The release conditions depend on the receiver material, as successful transfer requires the adhesion between the device and receiver substrate to exceed that between the device and PDMS stamp during release. Since this adhesion is determined by the composition and roughness of the contacting surfaces, different receiver materials require different release conditions.

4.5 Optical characterisation

The optical characterisation of the receiver chip was performed both before and after the transfer of the suspended GaN membrane, using the same experimental setup described in Chapter 2. During the characterisation of the SiN receiver chip, it was observed that waveguides with widths of 1 μm and 1.5 μm did not support guided modes. This occurred because SiN etching process used SF_6 only, which is known to etch isotropically. As a result, lateral etching occurs beneath the photoresist mask, leading to a reduction in the effective waveguide width [164]. Therefore, 2 μm waveguide width was used for transfer printing of GaN membrane.

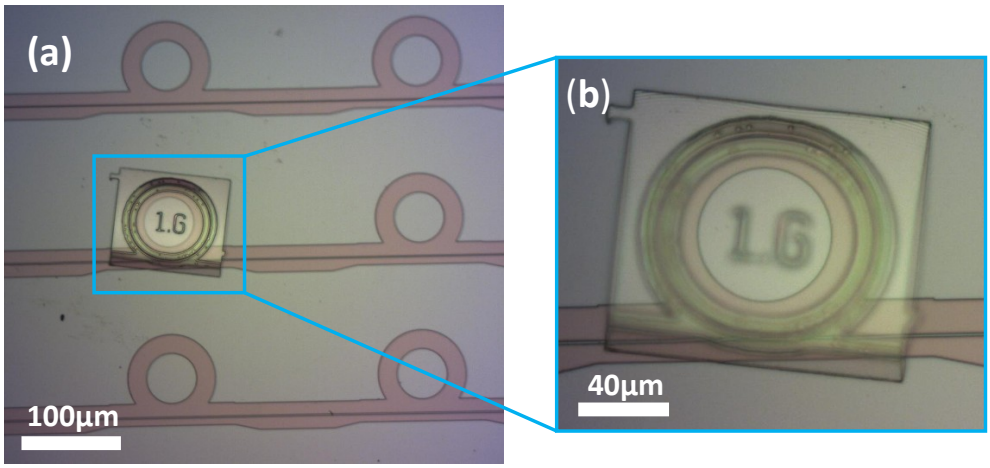

Figure 4.14: Micro-transfer-printed suspended GaN membrane integrated on a SiN waveguide. (a) Suspended GaN membrane with a bend radius of 60 μm and a waveguide width of 1.6 μm (b) Zoomed-in view of the suspended GaN membrane.

Figure 4.14 shows the micro-transfer-printed GaN membrane ring with a width of 1.6 μm printed onto the SiN receiver chip. A slight rotational misalignment of the GaN membrane can be observed, which is attributed to lateral shear during stamp release, while the coupling region remains approximately aligned. Following the transfer printing process, the GaN membranes were observed to exhibit out-of-plane bowing, as shown in Figure 4.14(b). This bowing increases the vertical separation between the GaN membrane and the underlying SiN waveguide. The transmission spectra taken before and after printing, shown in Figure 4.15, show no observable change in the transmission spectrum, indicating negligible optical interaction due to insufficient evanescent field

overlap between the SiN waveguide and the GaN membrane. This result indicates that the vertical separation between the GaN membrane and the underlying SiN waveguide is the most critical transfer printing tolerance, as membrane bowing can suppress the evanescent coupling even when the lateral alignment remains sufficient.

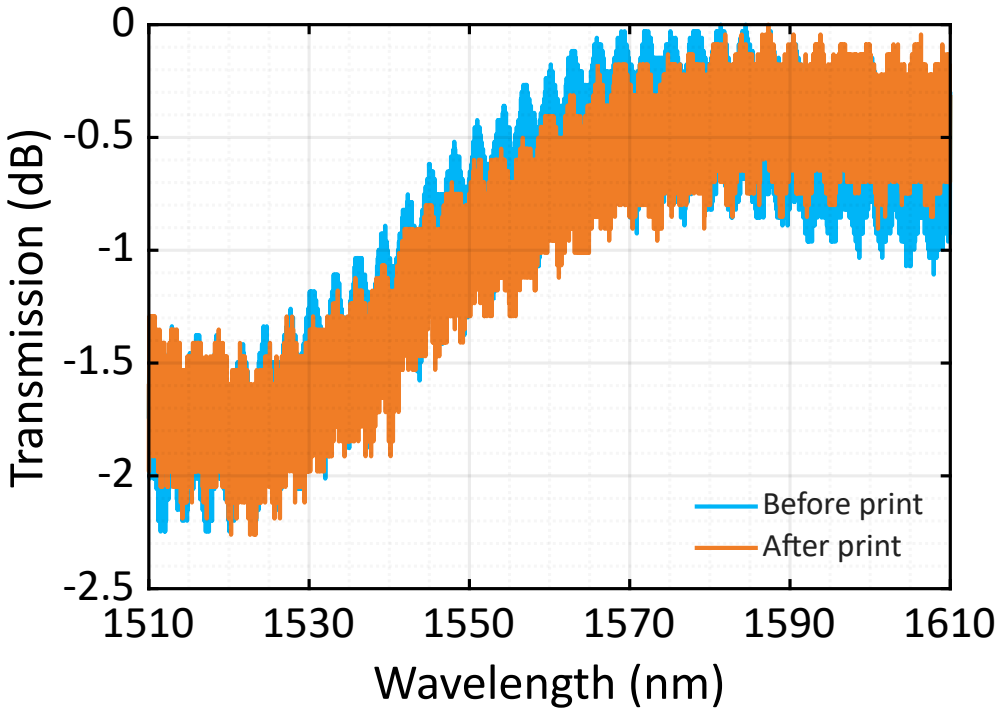

Figure 4.15: Optical transmission spectra of the SiN waveguide for TE polarisation, measured before and after the transfer printing process.

This membrane bowing is attributed to the thermal expansion coefficient mismatch between GaN (5.6×10^{-6} K^{-1}) and Si (2.6×10^{-6} K^{-1}), which introduces residual stress in the GaN layer upon cooling from the metal–organic chemical vapour deposition (MOCVD) growth temperature [165]. The resulting out-of-plane deformation introduces a finite vertical gap between the GaN membrane and the underlying SiN waveguide. Figure 4.16 shows that the evanescent field from 1 μm wide SiN waveguide decays exponentially into the air cladding, with a 1/e decay length of approximately 96 nm. As a result, the field intensity reduces to 34% at the a gap of 100 nm, and 12% at 200 nm. Since the evanescent coupling relies on this field overlap, even a small out-of-plane deformation of few hundred nanometres is sufficient to significantly reduce

the coupling strength, explaining the absence of observable coupling to GaN membrane in measured transmission.

For successful heterogeneous integration, membrane flatness is essential. Recent studies have demonstrated that the deposition of SiO_2 or SiN_x layers on GaN membranes using PECVD (plasma-enhanced chemical vapour deposition) can provide stress compensation, enabling the fabrication of flat suspended membranes suitable for micro-transfer printing applications [166, 167]. A potential future extension of this work would be to investigate the required thickness of PECVD SiO_2 for effective stress compensation, thereby enabling evanescent coupling between the GaN membrane and the SiN waveguide, which was not achieved in this work due to membrane bowing. In addition, a thin adhesion layer could be introduced on the receiver substrate to increase the bonding between the membrane and receiver [167, 168], thereby reducing the rotational misalignment caused by lateral shear during membrane release.

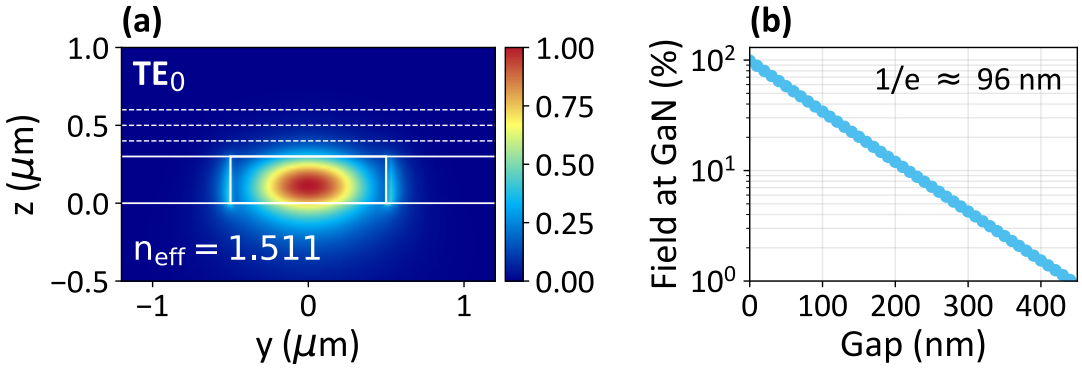

Figure 4.16: Evanescent field decay of the SiN bus mode. (a) Mode profile of a 1 μm-wide SiN waveguide at $\lambda = 1550$ nm, with the GaN underside indicated by dashed lines for air gaps of 100, 200, and 300 nm. (b) Normalised field intensity at the GaN membrane as a function of the air gap.

4.6 Summary

This chapter presented the efforts toward hybrid integration of GaN-on-SiN using a transfer printing approach. Detailed simulations and fabrication processes of both the donor and receiver chips were discussed. The successful transfer printing of GaN

membranes onto SiN substrates was demonstrated, confirming the feasibility of the transfer printing process. However, no optical coupling between the GaN membrane and the underlying SiN waveguide was observed. This limitation was attributed to membrane bowing caused by residual stress within the GaN membrane, which prevented proper alignment and mode overlap. To achieve effective hybrid integration of GaN on SiN, a systematic investigation of PECVD SiO_2 or SiN stress-compensation layers is required to mitigate membrane bowing and enable reliable optical coupling.

Chapter 5

Inverse-designed polymer devices

This chapter presents the design and implementation of inverse-designed compact polymer photonic devices, including SU-8-based waveguide bends and multilayer vertical couplers. The chapter begins with motivation of implementing inverse design in polymer photonics, and discuss the theoretical background of inverse design, with particular emphasis on adjoint-based optimisation method used to realise compact and efficient photonic structures. This is followed by the fabrication of the proposed devices and optical transmission measurements to evaluate device performance.

5.1 Introduction

The recent emergence of artificial intelligence (AI) and high-performance computing (HPC) has led to a significant increase in the amount of data being transported across networks, with data volumes expected to grow exponentially in the coming years. As a result, the routing capabilities of existing planar photonic circuits that rely on in-plane waveguide crossings will no longer be able to satisfy the scalability requirements of advanced data-driven technologies. Multilayer photonic systems provide a promising solution to this bottleneck by routing data across multiple vertical layers, rather than relying solely on in-plane crossings. In this context, multilayer photonics refers to the vertical stacking of multiple waveguide layers interconnected through optical transitions to enable dense three-dimensional routing [75, 76, 169].

To date, this multilayer approach has been extensively explored using silicon and silicon nitride (SiN) material platforms [75, 80, 169, 170, 171]. These platforms typically employ grating-based and evanescent coupling mechanisms for interlayer power transfer; however, grating couplers suffer from wavelength sensitivity and cross talk [77, 78], while evanescent coupling structures, such as adiabatic tapers, often require large device footprints [79, 80, 81]. However, three-dimensional integration based on Si and SiN often introduces several challenges, including reliance on high-temperature processing steps that can limit back-end CMOS compatibility [73], the use of expensive substrates, and stringent thickness control requirements for reliable vertical coupling and routing [77, 80]. In contrast, polymer photonic platforms employ low-temperature fabrication processes, making them compatible with CMOS back-end integration and flexible substrates. Polymer waveguides are also comparatively inexpensive to fabricate, and their typically tall cross-sectional profiles make vertical alignment between layers more tolerant [82, 172]. The primary trade-off associated with polymer photonics is their relatively low refractive-index contrast, which results in larger device dimensions [173]. This limitation becomes particularly significant for multilayer photonic systems, where the footprint of passive routing components increases rapidly with circuit complexity [76]. Several approaches have been explored to realise high index-contrast polymer waveguides through the integration of additional materials with higher refractive indices; however, such solutions often increase fabrication complexity [174].
Inverse design has been widely adopted in photonics as a powerful methodology for realising compact and unconventional device geometries that are difficult to achieve using traditional design approaches [175, 176]. This capability is particularly attractive for polymer photonics, where inverse design can mitigate the footprint penalties imposed by low refractive-index contrast and enable scalable multilayer routing architectures. To date, inverse design techniques have been extensively explored within silicon photonics [177, 178], where the high refractive-index contrast enables compact device footprints and dense integration. In polymer photonics, however, inverse-designed devices have primarily been demonstrated in planar two-dimensional geometries [179]. As a result, the extension of inverse design to multilayer polymer photonic systems, where vertical

routing and interlayer transitions play a critical role in scalability, remains relatively unexplored.

Among available polymer materials, SU-8 is a negative-tone epoxy photoresist that has been widely used for optical waveguide patterning. As demonstrated in earlier chapters, SU-8 has been employed as a strip waveguide layer on lithium niobate to realise an etch-less platform. SU-8 exhibits a refractive index of approximately 1.57, low optical loss, and a broad transparency window covering telecommunications wavelengths. In addition, it is widely available, compatible with standard photolithographic processing, and well suited for scalable and low-cost fabrication [82, 180, 181].

This chapter investigates inverse-designed multilayer polymer photonic structures as a viable platform for scalable optical routing. By combining low-temperature polymer processing with inverse design methodologies, this work aims to address the inherent size limitations of polymer waveguides while preserving their advantages for multilayer photonic integration.

5.2 Inverse design

In photonic integrated circuits, optical devices are traditionally designed using a forward design approach shown in Figure 5.1(a), where an initial device geometry is assumed and its optical response is subsequently calculated using numerical simulations. The device structure is then manually adjusted in an iterative manner until the desired optical performance is achieved. While this approach is widely used, it relies heavily on designer intuition and becomes increasingly inefficient for complex structures with large design spaces. In contrast, inverse design reverses this workflow by starting from the desired device specifications and target optical response. An optimisation algorithm is employed to systematically modify the device geometry, repeatedly evaluating its optical response through numerical simulations until a structure is obtained that satisfies the required performance criteria as detailed in Figure 5.1(b). One of the key advantages of inverse design is its ability to generate compact, high-performance photonic devices through a fully automated optimisation process, often yielding non-intuitive

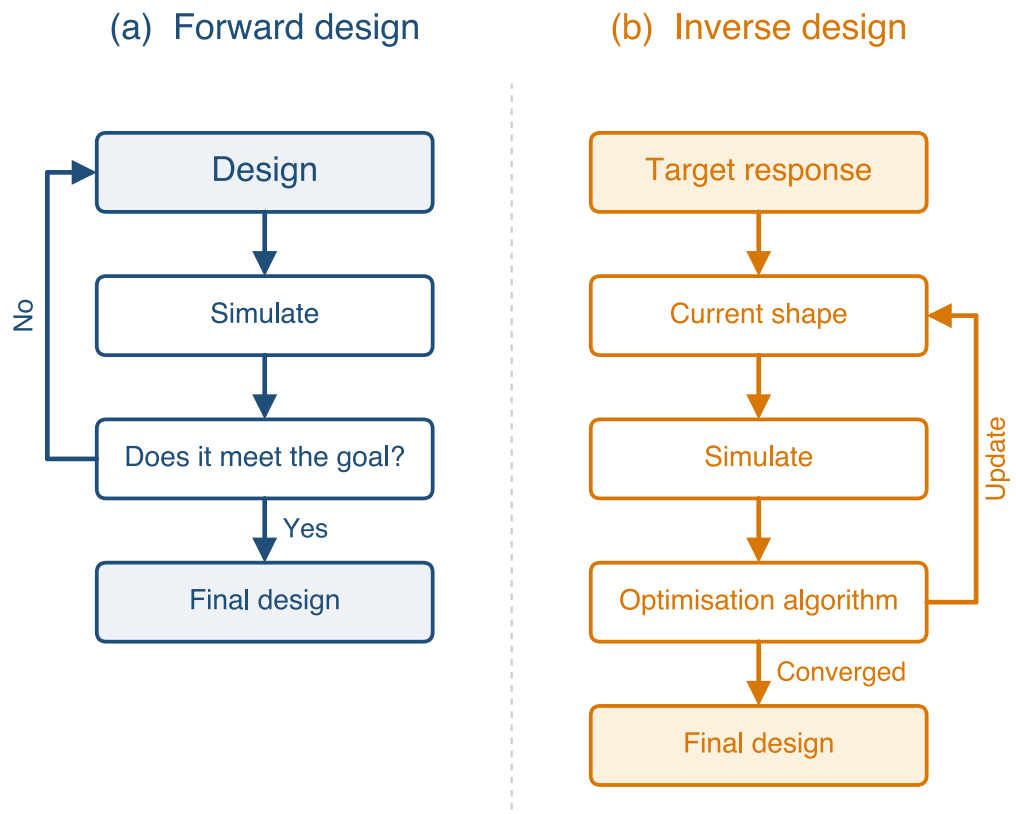

Figure 5.1: Flowchart illustrating optical device design approaches: (a) forward design; (b) inverse design.

geometries that are difficult to realise using conventional forward design methods.

5.2.1 Density-based topology optimisation

In inverse design, the optical device geometry is not defined in the traditional manner by explicitly specifying boundaries or waveguide shapes. Instead, the design region is discretised into a grid and the geometry is represented numerically by a set of parameters that can be modified by an optimisation algorithm [182, 183]. The design region is discretised into a two-dimensional array of pixels, where each pixel is assigned a density parameter $\rho \in [0, 1]$ [182]. A value of $\rho = 0$ denotes air, while $\rho = 1$ corresponds to the core material, which in this work is SU-8 polymer as shown in Figure 5.2. Intermediate values of ρ are permitted during optimisation and provide continuous variables that

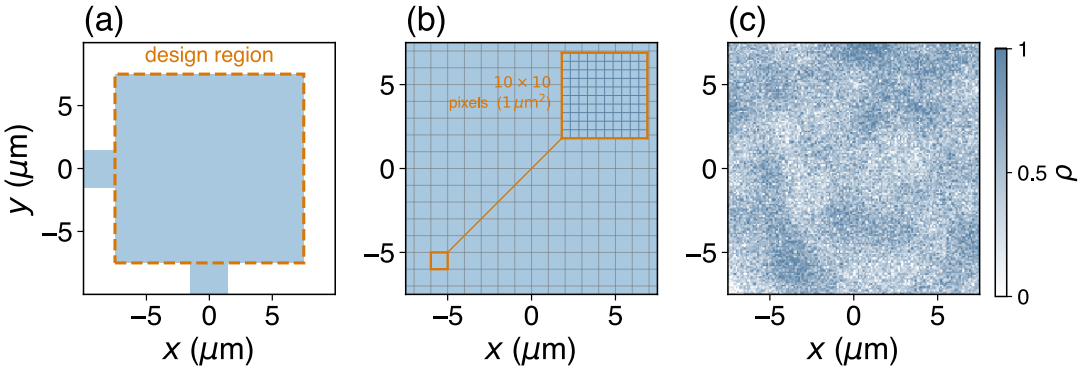

Figure 5.2: Density-based topology optimisation parametrisation showing (a) the design region, (b) the corresponding pixel grid, and (c) an example density field ρ, where each pixel is assigned a continuous value between air ($\rho = 0$) and core material ($\rho = 1$) before the design converges.

enable smooth, gradient-based modification of the device geometry. The density distribution is mapped to a spatial permittivity profile through linear interpolation between the permittivity of air and that of the SU-8 core material, as shown in Equation 5.1, allowing the FDTD solver to evaluate the optical response for both intermediate and final geometries.

$$\varepsilon(\mathbf{r}) = \varepsilon_{\text{air}} + \rho(\mathbf{r})\big(\varepsilon_{\text{core}} - \varepsilon_{\text{air}}\big), \tag{5.1}$$

Allowing continuous density values introduces intermediate, or "grey", regions that do not correspond to any physically realisable material. While this relaxation is essential for gradient-based optimisation, such regions must be eliminated before a final, fabricable device geometry is obtained. To address this, a filtering operation is applied to smooth the spatial density distribution and impose a minimum feature size [182]. This is followed by a projection operation, which progressively drives the filtered density towards a binary distribution corresponding to air or SU-8 polymer [184]. Overall, the effect of the projection is strengthened as the optimisation proceeds, resulting in a fully binarised design upon convergence [183]. The following section discusses how optimisation is performed on such parameterised geometries to realise compact and non-intuitive photonic structures that are difficult to obtain using conventional design approaches.

5.2.2 Adjoint method

Finite-difference methods are commonly used for sensitivity analysis by perturbing each design parameter individually and evaluating the resulting change in device performance. Denoting the device performance by a scalar objective function J and the design parameters by the vector $\mathbf{p}$, this approach requires on the order of $2N$ full electromagnetic simulations to compute the gradient $\nabla_{\mathbf{p}} J$ for a problem with N parameters. As a result, finite-difference methods become computationally expensive for large-scale inverse-design problems. In addition, the accuracy of the computed derivatives depends on the choice of the perturbation step size, and the resulting gradients are inherently approximate [185].

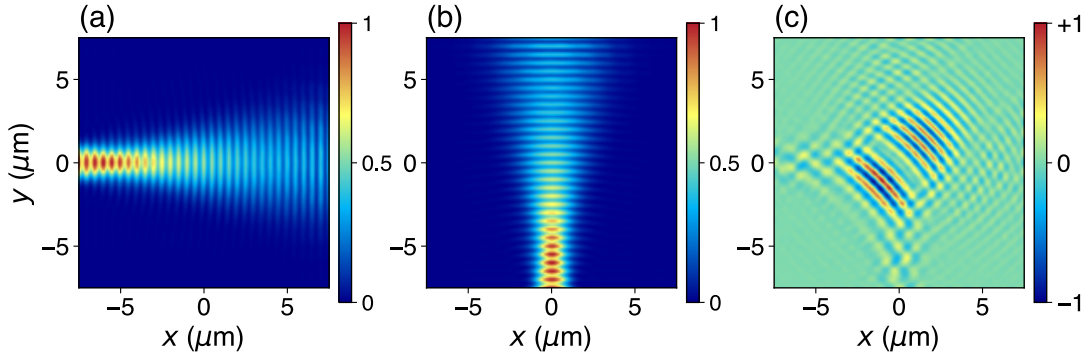

Figure 5.3: Adjoint-method visualisation of gradient computation. (a) Forward-field intensity $|\mathbf{E}_{\text{fwd}}|^2$ obtained from an FDTD simulation with the source placed at the input port. (b) Adjoint-field intensity $|\mathbf{E}_{\text{adj}}|^2$ from a second FDTD simulation with a virtual source placed at the output monitor. (c) Pixel-wise overlap $\text{Re}[\mathbf{E}_{\text{fwd}} \cdot \mathbf{E}_{\text{adj}}]$ corresponds to the gradient $\partial J / \partial \varepsilon(\mathbf{r})$ at each pixel.

In contrast, the adjoint method enables the computation of the gradient of the objective function using only two electromagnetic simulations, independent of the number of design parameters [175, 186]. A forward FDTD simulation is first performed to evaluate the electric field distribution as shown in Figure 5.3(a) and compute the objective function J. A second FDTD simulation is then carried out with an adjoint source placed at the monitor location associated with the objective as presented in Figure 5.3(b). The gradient $\nabla_{\mathbf{p}} J$ is obtained from the overlap of the forward and adjoint electromagnetic fields as depicted in Figure 5.3(c), enabling efficient and accurate gradient-based opti-

misation.

Once the gradient has been computed, the forward–adjoint simulation is repeated iteratively, with each iteration involving a new pair of forward and adjoint FDTD simulations to evaluate updated sensitivities. The gradients obtained from the overlap of the forward and adjoint electromagnetic fields are used to modify the device geometry represented in a pixels, discussed in above section. The optimisation parameters $\mathbf{p}$ correspond to the pixel values controlling the spatial density field of the device. At each iteration, the updated density distribution is processed using the filtering and projection operations described earlier, ensuring that the evolving geometry remains binary and compatible with fabrication constraints. This iterative optimisation loop continues until the desired objective function is achieved. The following section will discuss the optical geometries implemented using adjoint method using polymer on glass.

5.3 Inverse design of polymer devices

As discussed in earlier sections, the refractive-index contrast between SU-8 polymer and the glass substrate is relatively small, which results in large waveguide bend radii, typically on the order of $100 - 200\,\mu$m. Although polymer photonics offers several advantages, such as low-cost fabrication, ease of integration, and mechanical flexibility, the requirement for large bends poses a significant challenge for device miniaturisation and scalable photonic integration. Consequently, the realisation of compact, low-loss waveguide bends is a critical requirement for advancing scalable polymer photonic circuits. A similar challenge was addressed in Chapter 2 through BIC-based mode engineering on a strip-loaded lithium niobate platform. In this chapter, inverse design is employed to realise compact photonic devices in a stand-alone SU-8 polymer platform, enabling a significant reduction in device footprint. Motivated by these considerations, compact waveguide bend geometries are designed using the adjoint-based optimisation and implemented in Tidy3D, as introduced in the previous section. All simulations are performed using a refractive index of 1.57 for SU-8 and 1.44 for the glass substrate, at 1550 nm. Waveguide bends are first selected as test-case structures to evaluate both

the effectiveness of the inverse-design approach and the practical capabilities of the in-house lithography system. The following sections present the detailed numerical simulations for inverse-designed SU-8 waveguide bends, and multi-layer vertical coupler. The inverse design devices were simulated by my colleague Dr. Jack Smith and provided the GDS of individual components. All the FDTD simulations presented here are performed by importing GDS files into Tidy3D.

5.3.1 Bends

The simulation schematic of a representative inverse-designed 90° SU-8 bend is shown in Figure 5.4. The design region, measuring $15 \times 15 \times 2\,\mu\text{m}^3$, is connected to input and output waveguides with a cross-section of $3 \times 2\,\mu\text{m}^2$. The design region is discretised using a pixel pitch of $0.1\,\mu$m, resulting in a total of 22 500 design parameters. Within the design region continuos density variable $\rho[0\ 1]$ where 0 is glass refractive index, and 1 is for SU-8 refractive index. The optimisation algorithm starts with $\rho = 0.5$ as shown in Figure 5.4(a) where the design is featureless, and no light could reach the output port. At each step, the adjoint method computes the gradient of the objective function from forward and adjoint simulation as discussed above and is defined as:

$$J = T - \gamma,$$

where T represents the optical transmission at the output port and γ denotes a feature size penalty term which cost optimiser power whenever the feature size is smaller than the filter radius r. The Adam optimiser updates the design using learning rate of 0.25 over 40 iteration steps.

To ensure fabrication robustness and feasibility, two key parameters are considered. The first is the filter radius r. The optimisation is constrained to a minimum feature size of $1.2\,\mu$m by setting $r = 0.6\,\mu$m. This enforces a length scale constraint, penalising features smaller than $1.2\,\mu$m and filtering them out of the design. As a result, the final design layout shown in Figure 5.4(b) is compatible with fabrication using the in-house lithography tool, in good agreement with the Heidelberg DWL66+. This minimum

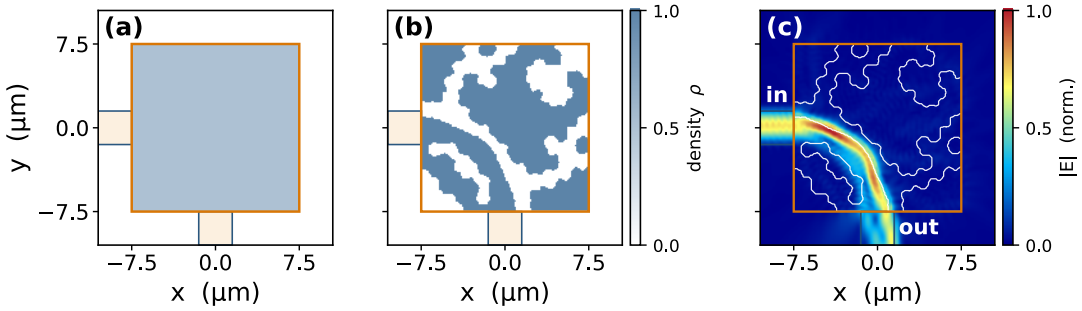

Figure 5.4: Inverse design process of the compact S-bend: (a) design region, (b) optimised device layout, and (c) simulated electric field distribution of the optimised S-bend.

feature size was validated experimentally through checkerboard pattern exposure on SU-8 on glass. The second parameter is the projection sharpness β, which is increased linearly from 0 at the first iteration to 40 at the 40th iteration. This gradual increase converts intermediate (grey) density values ρ into binarised values corresponding to SU-8 and glass, ensuring a physically realisable and fabrication-ready structure as the optimisation progresses. Figure 5.4(c) present the resulting electric field magnitude of the compact bend. The device achieves a flux of 75.6, corresponding to an objective function value of 74%.

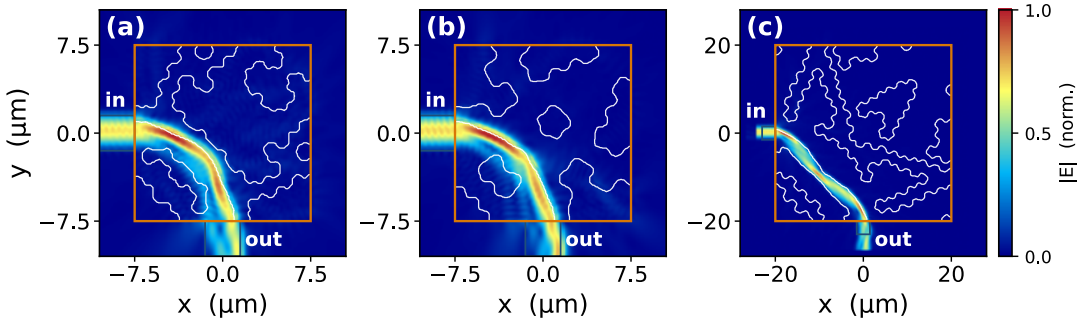

Figure 5.5: $|E|$ of the three SU-8 inverse-designed 90° bends at $\lambda = 1.55\,\mu$m: (a) 74 % and (b) 72 % in a 15×15 μm^2 design region; (c) 69 % in a 40×40 μm^2 region.

Figure 5.5 presents electric field magnitude of three SU-8 inverse-designed bends. A filter radius of 0.6 μm is used for Figure 5.5(a), while a larger radius of 0.7 μm is used in Figure 5.5(b) and (c), with all other parameters kept constant. In addition, the design

Table 5.1: Inverse-designed SU-8 90° bends.

Figure	Device	Objective J	Single-mode T	Total flux Φ
(a)	Bend, $15 \times 15\,\mu$m	74 %	50.7 %	75.6 %
(b)	Bend, $15 \times 15\,\mu$m	72 %	38.9 %	79.7 %
(c)	Bend, $40 \times 40\,\mu$m	69 %	61.7 %	75.9 %

region is increased to 40×40 for Figure 5.5(c) to investigate the impact on the overall performance of the bends. The corresponding objective values, single-mode transmission and total flux are summarised in Table 5.1.

The total flux and single-mode transmission were obtained by loading the inverse-designed GDS into Tidy3D and running a forward FDTD simulation. For all three bends the total flux is comparable to the objective value, but the single-mode transmission is lower. This discrepancy arises due to the binarisation of the design. During optimisation, the permittivity is represented in greyscale, meaning it can take intermediate values between SU-8 and air, and the objective is evaluated on this greyscale structure. When the design is exported to GDS, it is thresholded to a fully binary pattern, causing smooth features to become sharp transitions. This binarisation scatters part of the light into higher-order modes and lowers the single-mode transmission, while the total power, and hence the flux, stays almost the same. The $40 \times 40\,\mu$m bend in (c) is more robust against binarisation than the smaller $15 \times 15\,\mu$m bends and keeps a single-mode transmission closer to its objective, because the larger design region gives more degrees of freedom to recover the optimised response.

5.3.2 Multilayer vertical coupler

The schematic of the multilayer vertical coupler is shown in Figure 5.6. The design region for each layer is $50 \times 50 \times 2\,\mu\text{m}^3$ for both the bottom and top layers, with no gap between the stacked layers. This results in a total SU-8 thickness of $4\,\mu$m. The bottom layer consists of one input and one output port, each with a width of $3\,\mu$m and a height of $2\,\mu$m. The top layer includes a single output port with the same dimensions.

During optimisation, the projection parameter β started with 1 and was incremented

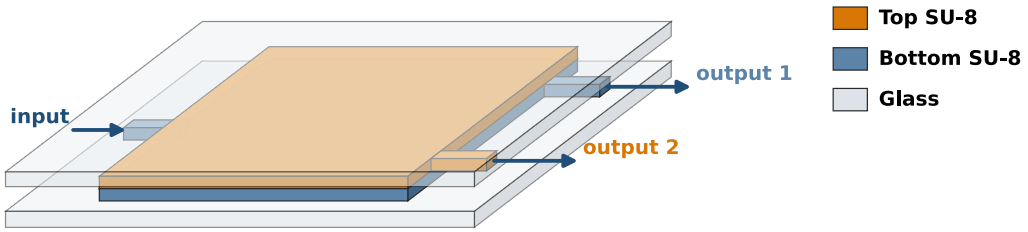

Figure 5.6: Schematic of a multilayer SU-8 vertical coupler with the input and Output 1 in the bottom layer, and Output 2 in the top layer.

by 0.2 over 60 iterations. The Adam optimiser was used with a learning rate of 0.1. A filter radius of $r = 0.7\,\mu$m was applied, corresponding to a minimum feature size of $1.4\,\mu$m. Features smaller than this threshold were penalised to ensure fabrication feasibility. This value was selected based on previous compact bend optimisations, where it provided good fabrication fidelity, which is critical for inverse-designed structures. The objective function for the vertical coupler is given in Equation 5.2:

$$J = I_{\text{top}} \cdot I_{\text{bot}} - \frac{1}{2}\left(P_{\text{top}} + P_{\text{bot}}\right), \tag{5.2}$$

where I_{top} and I_{bot} represent the fundamental TE-mode power in the top and bottom layers, respectively. The product term is chosen to enforce equal power splitting between the two layers; if a summation were used instead, the optimisation could favour one output while suppressing the other. The penalty terms P_{top} and P_{bot} are included to suppress features below $1.4\,\mu$m, ensuring compatibility with the in-house lithography system.

The binarised masks for the top and bottom layers after optimisation are shown in Figure 5.7. The electric field magnitude in both layers demonstrates that optical power is evenly distributed between the bottom and top outputs, as shown in Figure 5.8(a) and (b), respectively. This is further confirmed by the y–z cross-section at $x = 25\,\mu$m, where the optical modes are clearly observed in both layers.

We also test the robustness of the vertical coupler to lateral misalignment and to

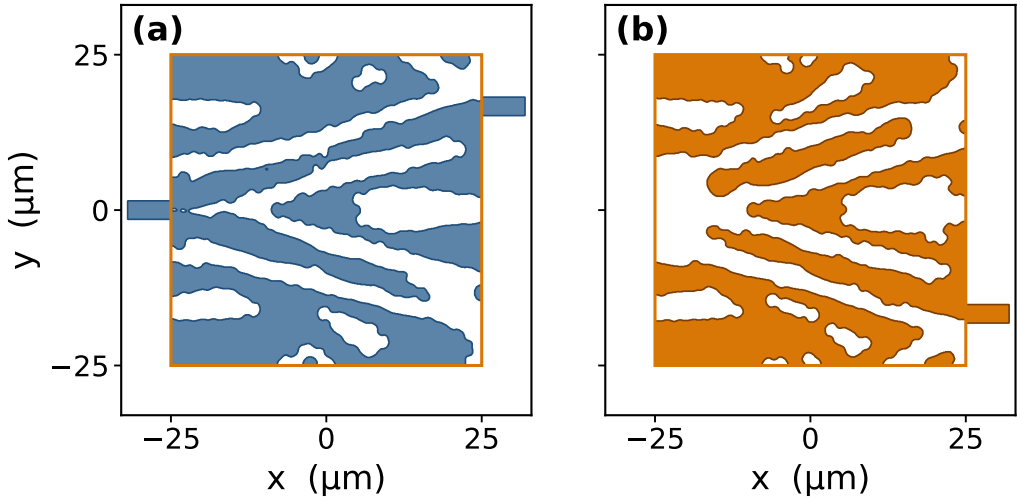

Figure 5.7: Finalised mask of multilayer vertical coupler after optimisation. (a) SU-8 bottom layer, (b) SU-8 top layer.

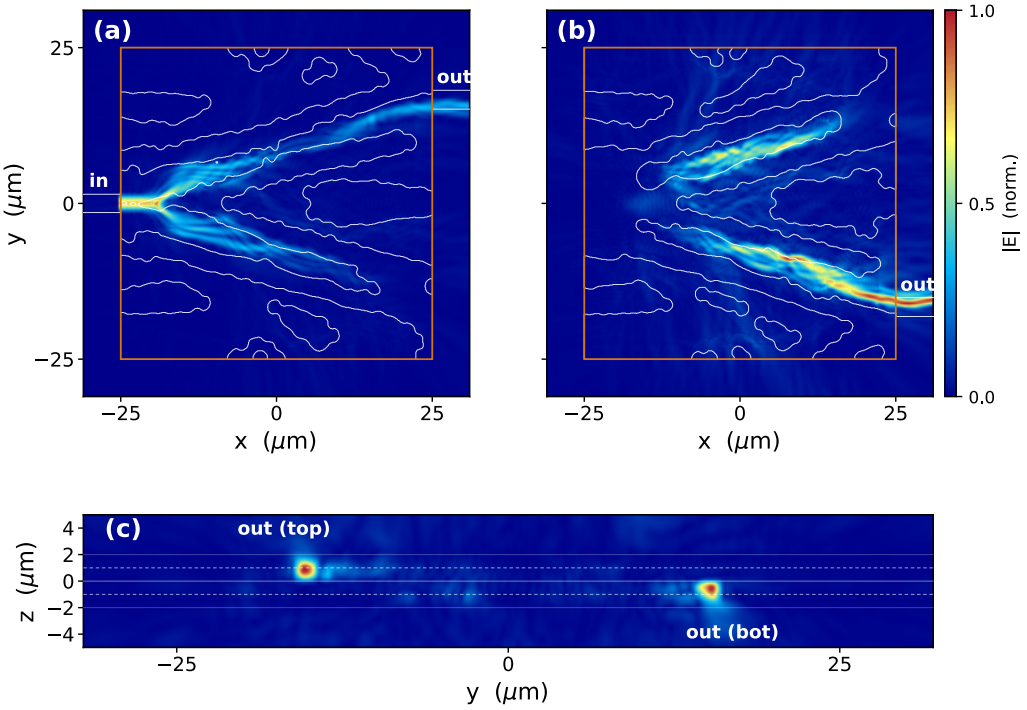

Figure 5.8: $|E|$ of the multilayer vertical coupler at $\lambda = 1.55\,\mu$m: (a) SU-8 bottom-layer mid-plane ($z = -1\,\mu$m); (b) SU-8 top-layer mid-plane ($z = 1\,\mu$m); (c) $y-z$ cross-section at $x = 25\,\mu$m.

interlayer-gap variation. For the misalignment, FDTD simulations were performed by offsetting the top coupler layer relative to the fixed bottom layer over 0–2 μm in each in-plane direction, as shown in Figure 5.9. In the longitudinal (x) direction the coupler is highly tolerant, both output ports remain within $\sim$1 dB of their peak up to $\sim$1 μm of offset, and the excess loss reaches only 3 dB at 2 μm. In the transverse (y) direction, however, the device is far more sensitive, the transmission drops steeply beyond $\sim$0.2 μm and reaches 3 dB of loss by $\sim$0.5 μm. Beyond this point the bottom port partially recovers, whereas the top port continues to degrade and remains lossy.

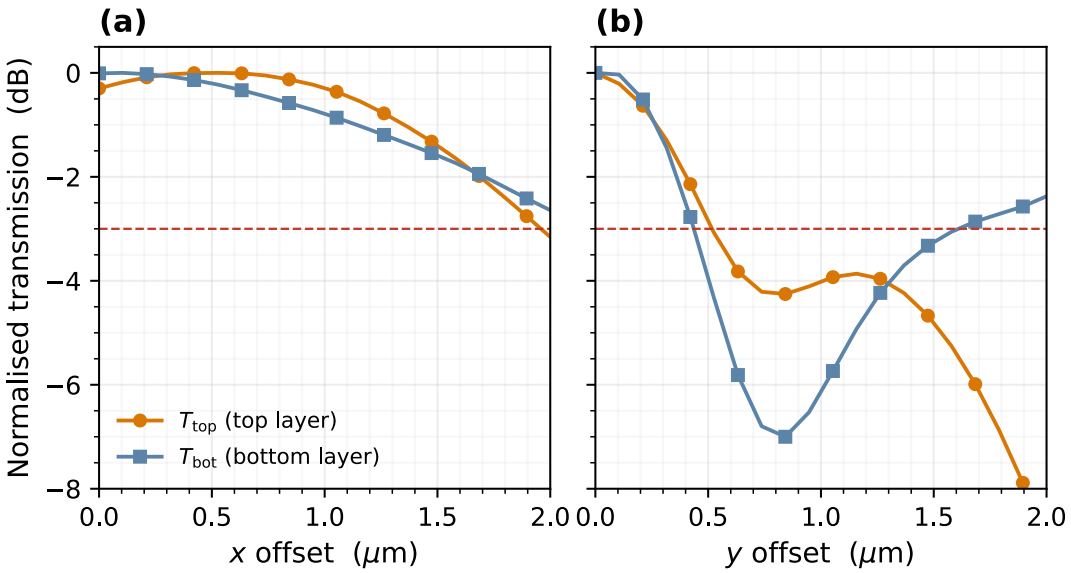

Figure 5.9: Misalignment tolerance for the vertical coupler in x and y, showing the normalised transmission (dB) of the top and bottom ports versus layer-to-layer offset: (a) x offset and (b) y offset. The dashed horizontal line depicts the -3 dB level.

Another critical parameter is the interlayer gap between the two layers. FDTD simulations were performed by increasing the gap from 0 to 1 μm, as shown in Figure 5.10. The coupler is highly sensitive to this gap, the top port transmission falls by 3 dB for a gap of only $\sim$0.08 μm and then decreases exponentially, which means no light couples to the top layer for gaps beyond $\sim$0.1 μm. The bottom port, in contrast, is largely unaffected, since it carries the in-plane through path and does not depend on the evanescent coupling between the layers.

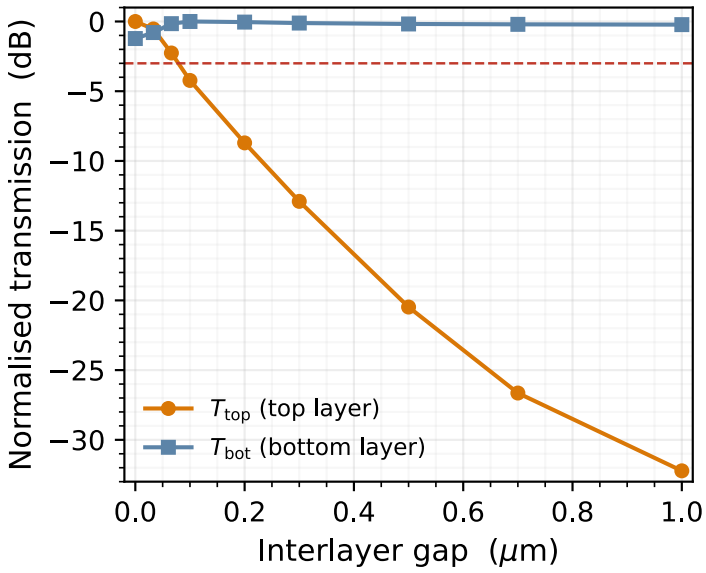

Figure 5.10: Normalised transmission (dB) of the top and bottom ports as a function of the interlayer gap between the vertical-coupler layers. The dashed horizontal line depicts the −3 dB level.

5.4 Chip layout of inverse-designed compact devices

The GDS layout of the inverse-designed 90° bends chip is shown in Figure 5.11. The layout includes slab with width of of 50 μm for alignment, straight waveguides with a width of 3 μm, followed by S-bends with a bend radius of 150 μm. Following the S-bends, compact bends with 69%, and 72%, and 74% are implemented, where the input straight waveguides are connected to the input ports of the compact bends. The output ports of the compact bends are connected to conventional bends, followed by output straight waveguides. Each device is replicated five times within the layout. The total chip length is 0.8 cm, and the chips are cleaved at both ends to allow optical coupling using an edge-coupling. Figure 5.12 presents the GDS layout of the multilayer vertical coupler chips. The bottom coupler layout is shown in Figure 5.12(a), where the input of the coupler is connected to straight waveguides, while the output is routed through an S-bend followed by straight waveguides. The layout includes 12 square support structures of size $500 \times 500\,\mu m^2$, with six located on each side of the chip to improve mechanical stability during bonding. Additionally, horizontal and vertical

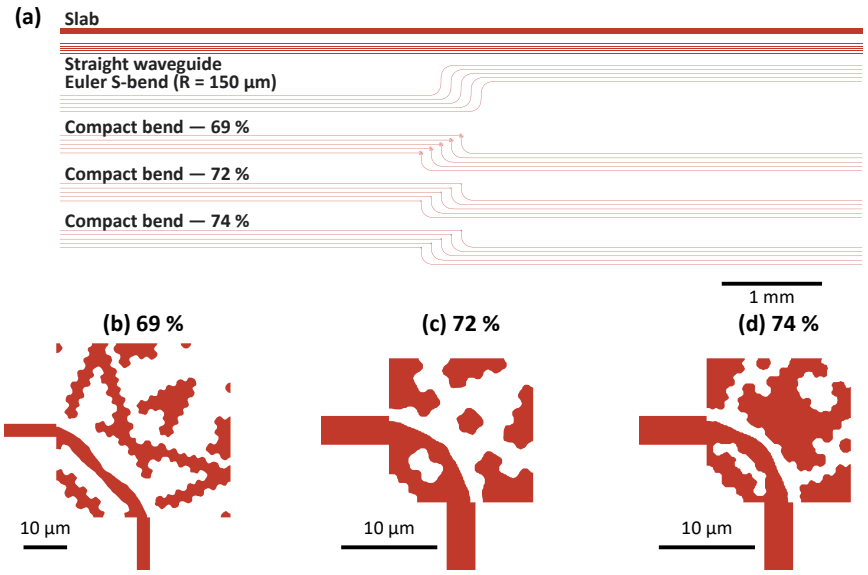

Figure 5.11: (a) GDS layout of inverse-designed SU-8 90° bends; (b) zoomed-in view of 69 % bend; (c) zoomed-in view of 72% bend; and (d) zoomed-in view of 74 % bend.

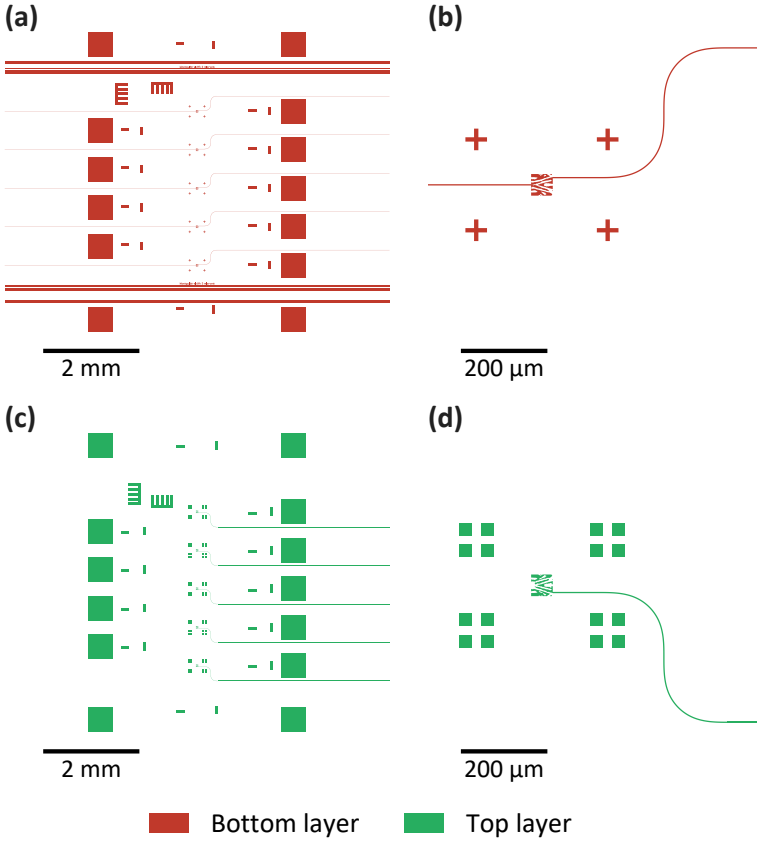

Figure 5.12: GDS layout of inverse-designed multilayer vertical couplers: (a) bottom layer chip of the vertical coupler; (b) zoomed-in view of the bottom coupler; (c) top layer chip of the vertical coupler; and (d) zoomed-in view of the top coupler.

vernier markers are distributed across the layout to enable accurate measurement of misalignment in both the x- and y-directions. The layout also includes horizontal and vertical comb structures at the top of the chip, which are used for coarse alignment between the two layers. The design further incorporates a slab with a width of 50 μm for alignment, along with five straight waveguides of 3 μm width located at the top and bottom edges of the chip.

The top coupler layer layout is shown in Figure 5.12(c), where the coupler is similarly connected through S-bends and straight waveguides. Corresponding square structures and vernier markers are included to ensure alignment and structural stability during multilayer bonding. The layout contains five copies of the vertical coupler, and the overlaid top and bottom layers are shown in Figure 5.13.

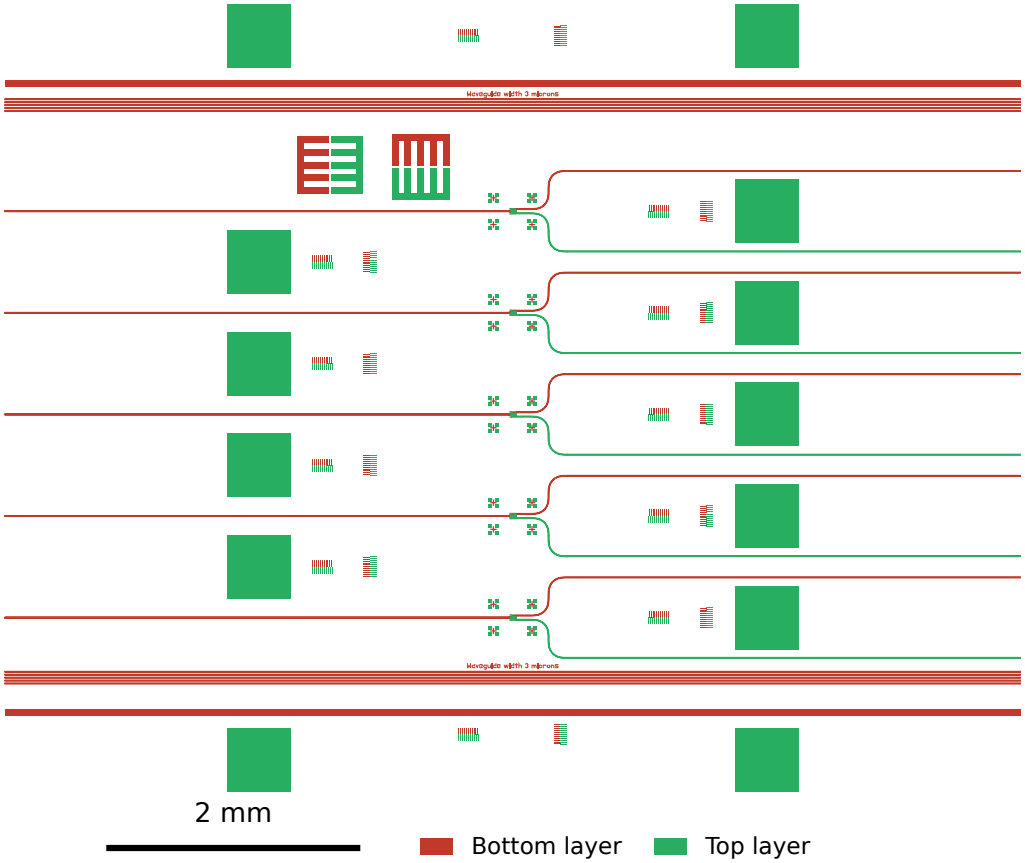

Figure 5.13: Overlay of the top and bottom layers of the multilayer vertical coupler chips.

5.5 Fabrication of inverse-designed devices

The inverse-designed polymer devices are fabricated using fabrication processes described in Chapter 2, with the primary difference being the use of a glass substrate instead of lithium niobate. While the change in substrate material mainly affects the exposure dose, dose optimisation was performed for this process, after which the rest of the fabrication process remains unchanged.

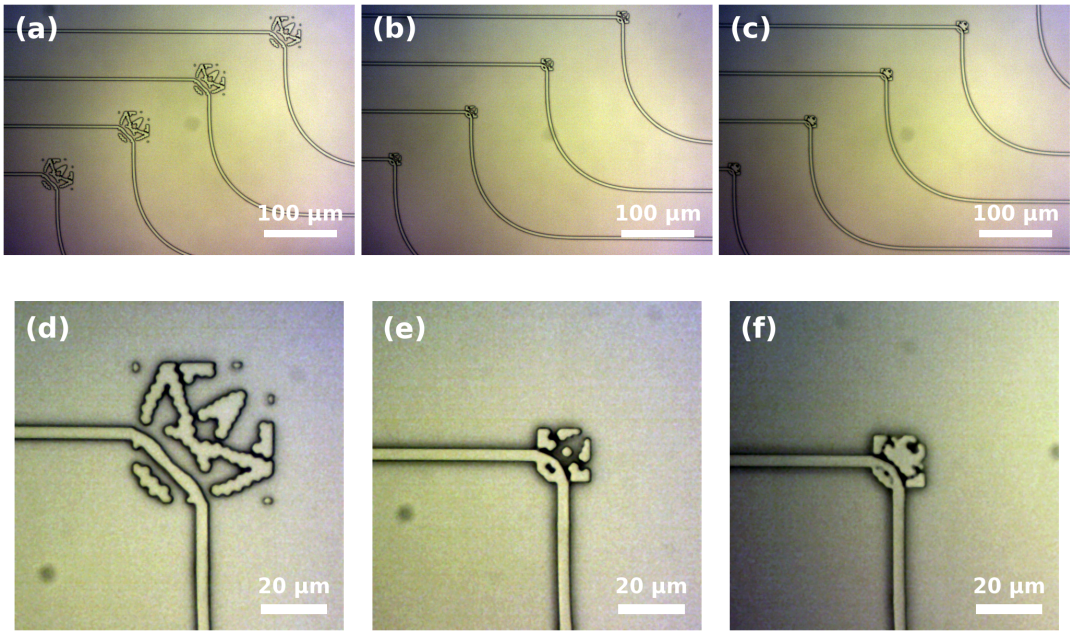

Figure 5.14: Optical microscope images of fabricated SU-8 compact bends: (a) 69%, (b) 72% and (c) 74% , with the corresponding zoomed-in images shown in (d), (e) and (f) respectively.

For inverse-designed geometries, the minimum resolvable feature size is a critical consideration. To know the practical fabrication limits of the Heidelberg DWL66+ with 2 μm thick SU-8 polymer resist, checkerboard test patterns with feature sizes ranging from 1–2 μm in 0.2 μm increments and 3–5 μm in 1 μm increments were fabricated. The dosage results indicate that features size of 1.2 μm represent the lower limit of reliable fabrication, with feature sizes of 1.4 μm and above exhibiting improved pattern fidelity. Based on these results, a minimum feature size of 1.2 μm and 1.4 μm were adopted for inverse-designed geometries. Figure 5.14 presents optical microscope images of the fab-

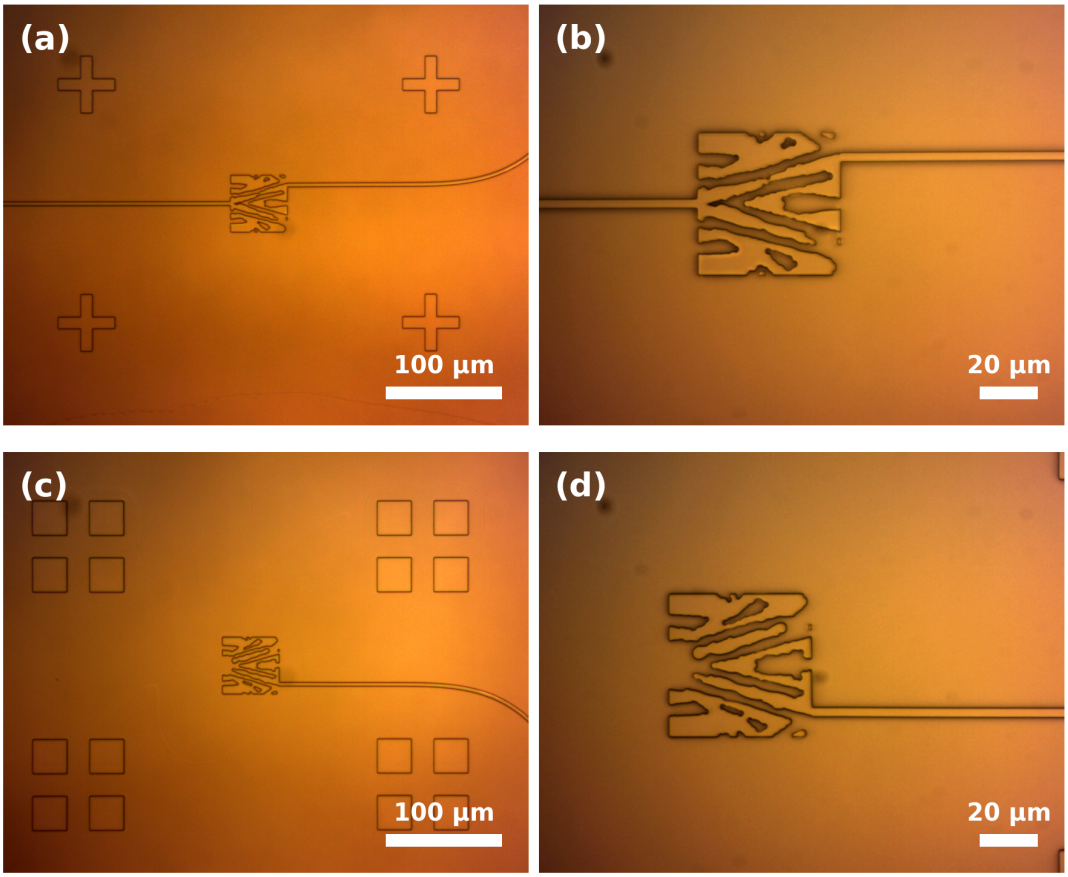

Figure 5.15: Optical microscope images of the fabricated vertical coupler layers: (a) bottom layer, (b) enlarged view of bottom layer, (c) top layer, and (d) enlarged view of top layer.

ricated compact bends. The edges of the larger bends are clearly defined, whereas the smaller bend features appear to be slightly overexposed. Figure 5.15 presents optical microscope images of the bottom and top layers of the vertical coupler, which were fabricated separately and cleaved for bonding. The images show that the features are well defined across both layers, which is crucial for the performance of inverse-designed devices, as overexposure or underexposure can change feature dimensions and lead to a reduction in optical transmission.

5.6 Flip-chip transfer printing of the SU-8 vertical coupler

Flip-chip bonding of the SU-8 vertical coupler was performed using a Nanolithography System (NLP 2000). This system has been widely used, along with the custom-built transfer printing tool discussed in Chapter 3, for the transfer printing of photonic devices within our group. Although the fundamental printing process remains similar, the NLP system has more limited capabilities compared to the custom-built setup. However, it is particularly modified for flip-chip bonding applications, and was therefore used for bonding the SU-8 chips in this work.

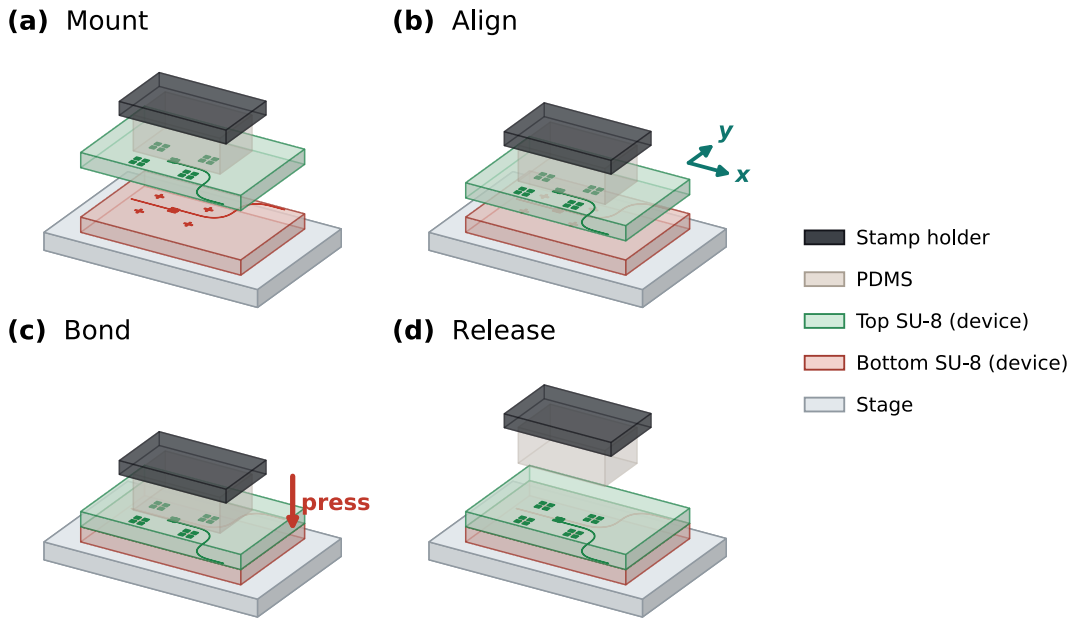

Figure 5.16: Flip-chip transfer printing of the two layer SU-8 vertical coupler.

The system comprises an optical microscope, precision translation stage, and a control PC. The process begins by placing the top SU-8 chip upside down onto a PDMS stamp as shown in Figure 5.16(a), which is then mounted onto the system. Since both the PDMS stamp and the glass substrate are transparent, it is possible to image through the device using the microscope, facilitating accurate alignment with the bottom chip. Subsequently, the bottom chip is placed on the translation stage, and the two chips are aligned using alignment markers present on both layers, as shown in Figure 5.16(b).

Alignment is verified visually by matching the vertical and horizontal reference lines displayed on the monitor to the on-chip alignment markers. Once satisfactory alignment is achieved, the two chips are brought into contact, and controlled pressure is applied to ensure proper bonding. The large square structures integrated into the design assist in achieving reliable mechanical bonding between the two layers. After bonding, the PDMS stamp along with the bonded chips is removed from the system. The PDMS stamp is then carefully peeled from the bonded chip, leaving chips bonded together only.

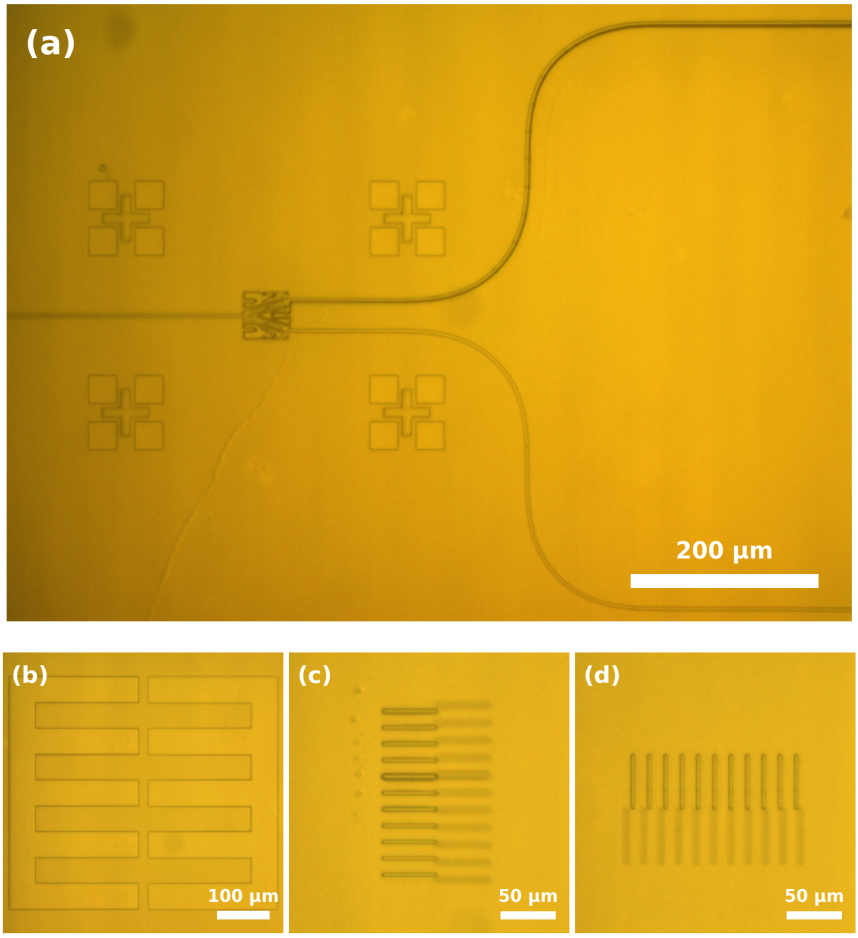

Figure 5.17: (a) Optical microscope image of the bonded vertical coupler, (b) E-comb alignment marker, (c) vernier marker with horizontal bars, and (d) vernier marker with vertical bars.

The optical microscope image of the bonded chip is shown in Figure 5.17(a), which

shows that good alignment is achieved between the two layers. This is important for the performance of the multilayer vertical coupler, as discussed above. The E-comb markers and vernier structures further confirm the good alignment, although a slight offset in the x direction can be seen in the vertical vernier in Figure 5.17(d). This offset should not affect the performance much, because the vertical coupler is tolerant to misalignment in the x direction, as discussed in simulation section.

5.7 Optical transmission

Optical transmission measurements of the inverse-designed polymer devices were performed using the same edge-fire injection setup used in Chapter 2 for passive characterisation. Since the devices are designed for TE polarisation, the setup was set to TE, and an input power of 350 μW was used for the measurements.

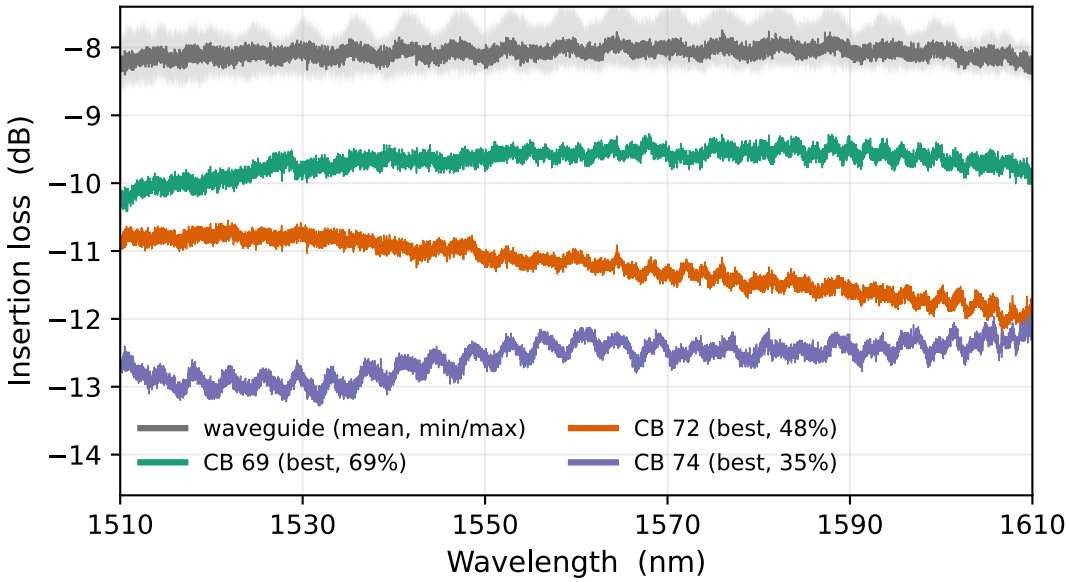

Figure 5.18: Insertion-loss spectra of the inverse-designed compact bends (best device of each design) and the straight-waveguide reference (mean of five devices, with shaded region indicating the minimum and maximum).

The inverse-designed compact-bend chip includes five replicas of the waveguides and bends, and the measured insertion loss of these devices as a function of wavelength is shown in Figure 5.18. The mean waveguide insertion loss is 8.1 ± 0.3 dB, and the best

device of each design reaches 69% (CB 69, $40 \times 40\,\mu\mathrm{m}^2$), 48% (CB 72, $15 \times 15\,\mu\mathrm{m}^2$), and 35% (CB 74, $15 \times 15\,\mu\mathrm{m}^2$), corresponding to excess losses of approximately 1.6, 3.1, and 4.5 dB, respectively, relative to the reference waveguide. The bend efficiency is defined as:

$$\text{Bend efficiency} = 10^{-(\mathrm{IL_{wg}} - \mathrm{IL_{device}})/10} \times 100 \tag{5.3}$$

where $\mathrm{IL_{wg}}$ and $\mathrm{IL_{device}}$ are the wavelength-averaged insertion losses (in dB of the straight waveguide and the bend, respectively. It should be noted that the compact bends are optimised for single-mode transmission, whereas the measurement collects the total guided power; therefore, these efficiency values are expected to lie between the single-mode transmission and the total flux of the bend. The best CB 69 and CB 72 devices fall within this range, while CB 74 falls below it, which we attribute to additional fabrication loss. All spectra show a wavelength ripple arising from Fabry–Perot reflections between the facets; the additional slower beating observed in the bends suggests that power is also coupled into higher-order modes.

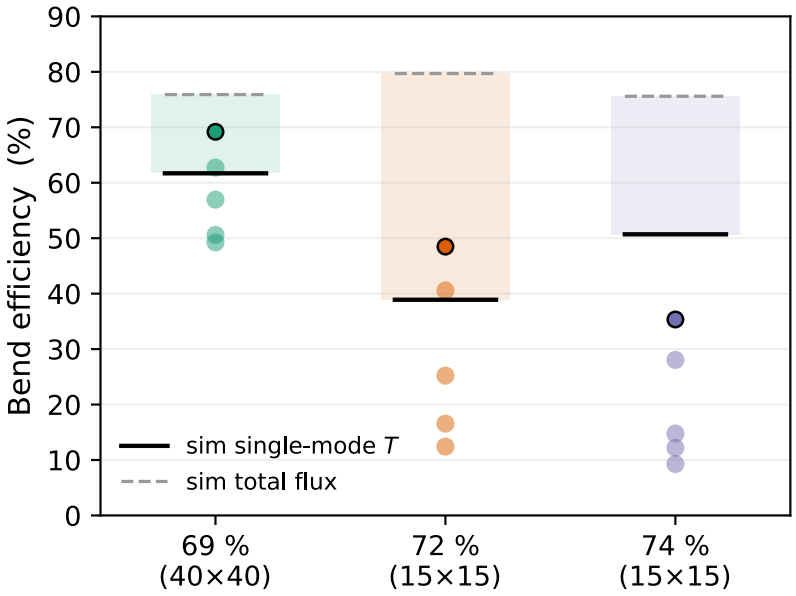

Figure 5.19: Measured bend efficiency of the inverse-designed compact bends (best highlighted). The shaded band spans simulated single-mode transmission (solid) and total flux (dashed).

The replicas of each compact bend design also show a variance in bend efficiency as shown in Figure 5.19, with CB 69 at 49–69%, CB 72 at 12–49%, and CB 74 at 9–35%. CB 69 is the most robust against fabrication variation and the most reproducible, while the smaller bends are more sensitive to fabrication. We attribute this wider spread to the overexposure of the smaller bends discussed above, where smaller features round off or merge with neighbouring structures, particularly in CB 74. In addition to fabrication, coupling and facet quality also contribute to the variation in efficiency across the devices.

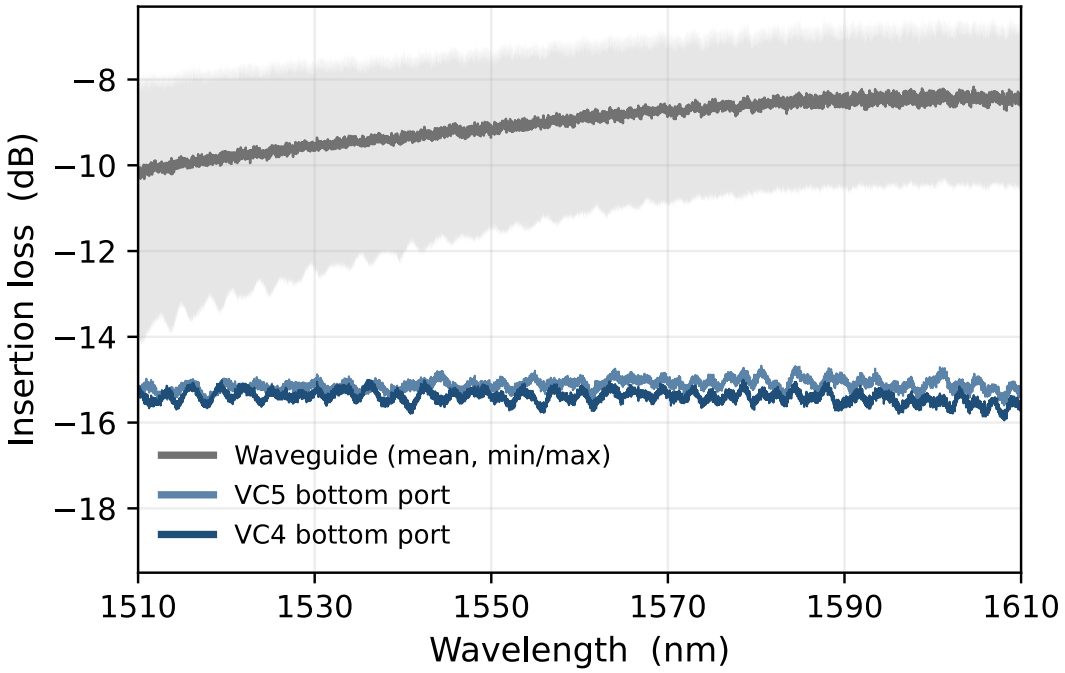

Figure 5.20: Measured insertion loss of the transfer-printed multilayer vertical-coupler chip. The shaded region in the waveguide transmission indicates the minimum and maximum insertion loss.

The multilayer vertical-coupler chip has five replica waveguides on the bottom layer and five bonded vertical couplers. The insertion loss of the vertical couplers and the reference waveguides is shown in Figure 5.20. The waveguide insertion loss here is higher than on the compact-bend chip and varies by about ±2 dB across the chip, which we attribute to a rougher cleaved facet.

For the in-plane bottom port, vertical couplers 4 and 5 show good agreement, each exhibiting approximately 6 dB more loss than a straight waveguide, although this value is approximate given the variation in waveguide loss. Some of this loss is expected, as the coupler splits the input power between its two output ports and radiates a fraction in the coupling region. With the interlayer gap suppressing vertical coupling, the power intended for the top port is lost rather than redirected to the bottom port. We were not able to access the inputs of the remaining three couplers due to an irregular cleave. However, the top port of the vertical coupler does not guide. As discussed above, the vertical coupling is sensitive to an interlayer gap exceeding 100 nm (Figure 5.10), beyond which no power is coupled to the top port. This is confirmed by the IR image in Figure 5.21, which shows no light at the top port while the bottom port guides. Together with the vernier alignment results, which confirm good lateral alignment, this indicates that the interlayer gap is the most likely cause.

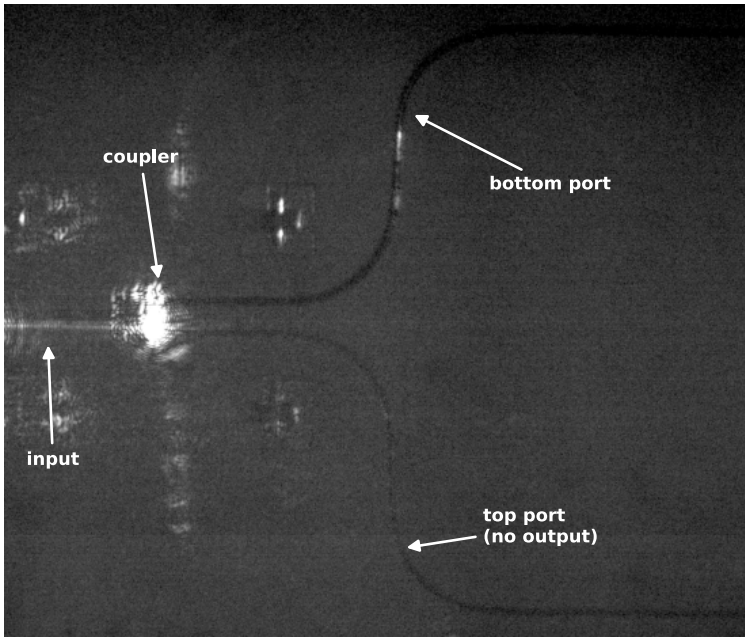

Figure 5.21: IR image of the multilayer vertical coupler, showing no light at the top port while the bottom port guides the light.

These results are preliminary and based on a small number of devices; they demonstrate the feasibility of the two-layer fabrication and bonding process rather than a final high-

efficiency coupler. To overcome the interlayer gap issue, future work should re-engineer the transfer-printing workflow to minimise residual air gaps at the bonding interface. This could include introducing a thin UV-curable index-matched adhesive layer, such as a Norland optical adhesive with a refractive index comparable to that of SU-8, to fill microscopic voids and improve optical contact between the layers, and optimising the bonding process through the application of uniform pressure, potentially under vacuum conditions, to reduce trapped air and achieve a more uniform bond interface. These modifications are expected to reduce the interlayer separation and improve the efficiency of vertical coupling in future multilayer polymer photonic devices.

In future multilayer photonic circuits, vertical routing could be realised through the selective placement of vertical couplers between waveguide layers, enabled by the controlled and repeatable interlayer bonding process described above. While conventional waveguides provide in-plane routing within each layer, vertical couplers enable optical signals to be transferred between layers at designated locations. This approach allows routing to be distributed across multiple photonic layers, increasing integration density and reducing the footprint of complex circuits.

5.8 Summary

This chapter presented inverse-designed compact bends and a multilayer vertical coupler on a polymer platform, and discussed the inverse design process in detail along with the fabrication of the compact bends. The results showed that larger bends are more robust to fabrication variations and can achieve performance consistent with simulation results, with the best compact bend reaching an efficiency of 69%. It also presented a multilayer vertical coupler, including its design, simulation, fabrication, and the transfer printing of the bottom and top layers. The measurements show that the bottom in-plane port supports guided propagation, but no light was coupled to the top port. Vernier alignment results confirmed good lateral alignment between the two layers, and the loss of top-port coupling is consistent with the observed sensitivity of the device to interlayer gaps exceeding 100 nm, indicating that a residual interlayer gap, rather than

misalignment, is the most likely cause. However, this preliminary result demonstrates the feasibility of the two-layer fabrication and bonding process. Further improvement can be achieved by using an adhesive layer to enhance bonding between the two layers and recover efficient vertical coupling.

Chapter 6

Conclusion

This thesis investigated approaches for developing compact, low-loss, and electro-optically functional photonic integrated circuits that are compatible with scalable manufacturing. LN is one of the most attractive materials for electro-optic modulators due to its outstanding electro-optic properties. However, conventional LN devices typically rely on etched waveguides, which require dedicated processing tools and lacks compatibility with CMOS process. To address these challenges, this thesis explored etchless device architectures that utilise the electro-optic properties of LN without physically etching the LN layer.

Passive etchless devices including waveguides, S-bends, and ring resonators were realised using the bound states in the continuum (BIC). Compact ring resonators with bend radii below $100\,\mu$m were demonstrated while maintaining low optical loss and achieving loaded quality factors of 4.17×10^4. In addition to the TM-polarised BIC mode, the geometry also supported TE-polarised guiding within the polymer loading layer. These results demonstrated that compact and low-loss devices can be achieved without direct etching of the lithium niobate layer.

The passive platform was subsequently extended to realise active electro-optic devices. A compact tunable ring resonator based on the BIC concept was demonstrated with a tuning efficiency of 0.49 pm/V. To the best of our knowledge, this represents the first tunable compact resonator based on the BIC principle. In addition, a Mach–Zehnder interferometer operating with TE polarisation was demonstrated, achieving improved

tuning efficiency 14.67 pm/V through utilisation of the larger r_{33} electro-optic tensor component. The results highlight the trade-off between compactness and modulation efficiency within etchless lithium niobate platforms.

Beyond lithium niobate, this thesis investigated heterogeneous integration of GaN membranes on silicon nitride photonic circuits using transfer printing. GaN possesses a lower electro-optic coefficient than lithium niobate but benefits from a mature fabrication ecosystem and offers potential for compact electro-optic devices. Successful transfer printing of GaN membranes onto SiN waveguides was demonstrated. However, optical coupling between the SiN waveguide and the transferred GaN membrane was not achieved due to membrane bowing. Nevertheless, this work established the complete process flow and identified the key challenges that must be addressed for future hybrid GaN-on-SiN photonic platforms.

Finally, inverse-designed polymer vertical couplers were investigated as a route towards compact three-dimensional optical interconnects. Inverse design enabled significantly reduced device dimensions compared with conventional taper-based approaches. Separate top and bottom polymer waveguides were fabricated and assembled using flip-chip transfer printing. Although vertical optical coupling to the upper waveguide layer was not achieved due to interlayer gaps between the polymer layers. In addition, fabrication-induced deviations in the inverse-designed devices were found to significantly affect device performance, highlighting the sensitivity of inverse-designed photonic devices to fabrication tolerances. These findings provide valuable insight for future transfer-printed photonic interconnect technologies.

Overall, this thesis demonstrates that compact and scalable photonic integrated circuits can be realised through etchless fabrication approaches and heterogeneous integration strategies. While challenges remain in transfer-printed hybrid photonic systems, the work establishes important foundations for future low-loss, compact, and manufacturable photonic integrated circuits.

6.1 Future work

The compact electro-optic modulators demonstrated in this thesis overcome several challenges associated with conventional etched lithium niobate devices. However, the compact BIC resonator utilises TM polarisation and therefore relies on the r_{13} electro-optic tensor component, which is approximately three times smaller than r_{33} which is exploited by TE polarisation. Future work could investigate polarisation diversity schemes that allow conversion between TM and TE modes. Such an approach would enable compact BIC resonators to exploit the larger r_{33} coefficient while maintaining compact device geometries and simplified fabrication.

For the hybrid GaN-on-SiN platform, future research should focus on overcoming the membrane bowing that prevented optical coupling between the transferred GaN membrane and the underlying SiN waveguide. Approaches such as silica or silicon nitride stress-engineering layers could be explored to reduce out-of-plane deformation of the membrane. Once efficient coupling is achieved, electrode integration could be introduced to realise tunable hybrid GaN-on-SiN photonic devices.

For the inverse-designed vertical couplers, future work should focus on minimising the interlayer gap formed during the transfer-printing process. Adhesive-assisted bonding could be investigated to ensure full contact between the layers to facilitate efficient optical coupling to the upper waveguide layer. In addition, inverse-designed devices were found to be highly sensitive to fabrication variations, with lithographic limitations altering critical device features and degrading performance. Future inverse-design methodologies should therefore incorporate fabrication-aware constraints and robustness optimisation to improve tolerance to fabrication imperfections while preserving the desired optical functionality.

Bibliography

[1] Martin Hilbert and Priscila López. The world's technological capacity to store, communicate, and compute information. *Science*, 332(6025):60–65, 2011.

[2] Adam Wright, David Reinsel, and IDC Research. Worldwide IDC Global DataSphere forecast, 2024–2028: AI everywhere, but upsurge in data will take time. Market Forecast US52076424, IDC, May 2024.

[3] D. Miller. Device Requirements for Optical Interconnects to Silicon Chips. *Proceedings of the IEEE*, 97(7):1166–1185, July 2009.

[4] Gordon E. Moore. Cramming more components onto integrated circuits. *Electronics*, 38(8):114–117, 1965.

[5] Karl Rupp. 42 years of microprocessor trend data. `https://www.karlrupp.net/2018/02/42-years-of-microprocessor-trend-data/`, 2018. Data repository: `https://github.com/karlrupp/microprocessor-trend-data`; CC-BY 4.0.

[6] Thomas N. Theis and H.-S. Philip Wong. The end of Moore's law: A new beginning for information technology. *Computing in Science & Engineering*, 19(2):41–50, 2017.

[7] Graham T Reed and Andrew P Knights. Silicon photonics: an introduction. 2004.

[8] David Thomson, Aaron Zilkie, John E Bowers, Tin Komljenovic, Graham T Reed, Laurent Vivien, Delphine Marris-Morini, Eric Cassan, Léopold Virot, Jean-Marc Fédéli, Jean-Michel Hartmann, Jens H Schmid, Dan-Xia Xu, Frédéric Boeuf,

Peter O'Brien, Goran Z Mashanovich, and M Nedeljkovic. Roadmap on silicon photonics. *Journal of Optics*, 18(7):073003, June 2016.

[9] Raymond G. Beausoleil. Large-scale integrated photonics for high-performance interconnects. *J. Emerg. Technol. Comput. Syst.*, 7(2):6:1–6:54, July 2011.

[10] Lukas Chrostowski and Michael E. Hochberg. *Silicon photonics design*. Cambridge university press, Cambridge, 2015.

[11] Y. Yuan, Y. Peng, S. Cheung, X. Xiao, W. V. Sorin, Z. Huang, D. Liang, A. Kumar, R. Liu, Y. Hu, S. Hooten, S. Palermo, M. Fiorentino, and R. G. Beausoleil. The perspective of all-silicon photonics and systems. *APL Photonics*, 10(6):060901, June 2025.

[12] Francesco Testa, Alberto Bianchi, Stefano Stracca, and Roberto Sabella. Silicon Photonics for Telecom and Datacom Applications. In Lorenzo Pavesi and David J. Lockwood, editors, *Silicon Photonics III: Systems and Applications*, pages 421–446. Springer, Berlin, Heidelberg, 2016.

[13] Weihan Xu, Qiqi Yuan, Yunhong Yang, Liangjun Lu, Jianping Chen, and Linjie Zhou. Progress and prospects for LiDAR-oriented optical phased arrays based on photonic integrated circuits. *npj Nanophotonics*, 2(1):14, May 2025.

[14] Tingzhao Fu, Jianfa Zhang, Run Sun, Yuyao Huang, Wei Xu, Sigang Yang, Zhihong Zhu, and Hongwei Chen. Optical neural networks: progress and challenges. *Light: Science & Applications*, 13(1):263, September 2024.

[15] Muhammad Ali Butt, Xavier Mateos, and Ryszard Piramidowicz. Photonics sensors: A perspective on current advancements, emerging challenges, and potential solutions (Invited). *Physics Letters A*, 516:129633, August 2024.

[16] Graham J. Triggs, Yue Wang, Christopher P. Reardon, Matthias Fischer, Gareth J. O. Evans, and Thomas F. Krauss. Chirped guided-mode resonance biosensor. *Optica*, 4(2):229–234, February 2017.

[17] Ali W. Elshaari, Wolfram Pernice, Kartik Srinivasan, Oliver Benson, and Val Zwiller. Hybrid integrated quantum photonic circuits. *Nature Photonics*, 14(5):285–298, May 2020.

[18] Peter J. Winzer, David T. Neilson, and Andrew R. Chraplyvy. Fiber-optic transmission and networking: the previous 20 and the next 20 years [Invited]. *Optics Express*, 26(18):24190, September 2018.

[19] Yong Zheng, Zhen Han, Liheng Wang, Pu Zhang, Yongheng Jiang, Huifu Xiao, Xudong Zhou, Mingrui Yuan, Mei Xian Low, Aditya Dubey, Thach Giang Nguyen, Qinfen Hao, Guanghui Ren, Arnan Mitchell, and Yonghui Tian. Integrated Microwave Photonics Multi-Parameter Measurement System. *Laser & Photonics Reviews*, 19(14):2500013, 2025. _eprint: https://onlinelibrary.wiley.com/doi/pdf/10.1002/lpor.202500013.

[20] Wim Bogaerts, Daniel Pérez, José Capmany, David A. B. Miller, Joyce Poon, Dirk Englund, Francesco Morichetti, and Andrea Melloni. Programmable photonic circuits. *Nature*, 586(7828):207–216, October 2020.

[21] Ryan Hamerly, Liane Bernstein, Alexander Sludds, Marin Soljačić, and Dirk Englund. Large-Scale Optical Neural Networks Based on Photoelectric Multiplication. *Physical Review X*, 9(2):021032, May 2019.

[22] Hsin-Pin Lo, Takuya Ikuta, Nobuyuki Matsuda, Toshimori Honjo, and Hiroki Takesue. Electro-optic modulators for photonic quantum information processing. In Qihuang Gong, Guang-Can Guo, and Byoung Seung Ham, editors, *Quantum and Nonlinear Optics VI*, page 24, Hangzhou, China, November 2019. SPIE.

[23] Georgios Sinatkas, Thomas Christopoulos, Odysseas Tsilipakos, and Emmanouil E. Kriezis. Electro-optic modulation in integrated photonics. *Journal of Applied Physics*, 130(1):010901, July 2021.

[24] Mian Zhang, Cheng Wang, Prashanta Kharel, Di Zhu, and Marko Lončar. Integrated lithium niobate electro-optic modulators: when performance meets scalability. *Optica*, 8(5):652, May 2021.

[25] Wesley D. Sacher and Joyce K. S. Poon. Dynamics of microring resonator modulators. *Optics Express*, 16(20):15741–15753, September 2008.

[26] W. Bogaerts, P. De Heyn, T. Van Vaerenbergh, K. De Vos, S. Kumar Selvaraja, T. Claes, P. Dumon, P. Bienstman, D. Van Thourhout, and R. Baets. Silicon microring resonators. *Laser & Photonics Reviews*, 6(1):47–73, January 2012.

[27] G. T. Reed, G. Mashanovich, F. Y. Gardes, and D. J. Thomson. Silicon optical modulators. *Nature Photonics*, 4(8):518–526, August 2010.

[28] Abdul Rahim, Artur Hermans, Benjamin Wohlfeil, Despoina Petousi, Bart Kuyken, Dries Van Thourhout, and Roel Baets. Taking silicon photonics modulators to a higher performance level: state-of-the-art and a review of new technologies. *Advanced Photonics*, 3(02), April 2021.

[29] Larry R. Dalton, Philip A. Sullivan, and Denise H. Bale. Electric field poled organic electro-optic materials: state of the art and future prospects. *Chemical Reviews*, 110(1):25–55, January 2010.

[30] Jingdong Luo, Su Huang, Yen-Ju Cheng, Tae-Dong Kim, Zhengwei Shi, Xing-Hua Zhou, and Alex K.-Y. Jen. Phenyltetraene-Based Nonlinear Optical Chromophores with Enhanced Chemical Stability and Electrooptic Activity. *Organic Letters*, 9(22):4471–4474, October 2007.

[31] Iman Taghavi, Maryam Moridsadat, Alexander Tofini, Shaheer Raza, Nicolas A. F. Jaeger, Lukas Chrostowski, Bhavin J. Shastri, and Sudip Shekhar. Polymer modulators in silicon photonics: review and projections. *Nanophotonics*, 11(17):3855–3871, September 2022.

[32] Andreas Messner, David Moor, Daniel Chelladurai, Roman Svoboda, Jasmin Smajic, and Juerg Leuthold. Plasmonic, photonic, or hybrid? Reviewing waveguide geometries for electro-optic modulators. *APL Photonics*, 8(10):100901, October 2023.

[33] Wolfgang Heni, Yasar Kutuvantavida, Christian Haffner, Heiner Zwickel, Clemens Kieninger, Stefan Wolf, Matthias Lauermann, Yuriy Fedoryshyn, Andreas F. Tillack, Lewis E. Johnson, Delwin L. Elder, Bruce H. Robinson, Wolfgang Freude, Christian Koos, Juerg Leuthold, and Larry R. Dalton. Silicon–Organic and Plasmonic–Organic Hybrid Photonics. *ACS Photonics*, 4(7):1576–1590, July 2017.

[34] Alexander A. Demkov and Agham B. Posadas. Ferroelectric BaTiO3 for Electro-Optic Modulators in Si Photonics. *IEEE Journal of Selected Topics in Quantum Electronics*, 30(4: Adv. Mod. and Int. beyond Si and InP-based Plt.):1–13, July 2024.

[35] Chenguang Deng, Yutong He, Wenfeng Yang, Han Yu, Zijian Hong, Hao Liu, Haojie Han, Wei Li, Yunpeng Ma, Zhongshan Zhang, Yongjun Wu, Jing Ma, Bing Xiong, Changzheng Sun, Rong Yu, Jing-Feng Li, Ji Zhou, Yi Luo, and Qian Li. Self-buffered epitaxy of barium titanate on oxide insulators enables high-performance electro-optic modulators. *Light: Science & Applications*, 15(1):21, January 2026.

[36] Di Zhu, Linbo Shao, Mengjie Yu, Rebecca Cheng, Boris Desiatov, C. J. Xin, Yaowen Hu, Jeffrey Holzgrafe, Soumya Ghosh, Amirhassan Shams-Ansari, Eric Puma, Neil Sinclair, Christian Reimer, Mian Zhang, and Marko Lončar. Integrated photonics on thin-film lithium niobate. *Adv. Opt. Photon.*, 13(2):242–352, Jun 2021.

[37] Cheng Wang, Mian Zhang, Brian Stern, Michal Lipson, and Marko Lončar. Nanophotonic lithium niobate electro-optic modulators. *Optics express*, 26(2):1547–1555, 2018. Publisher: Optical Society of America.

[38] Cheng Wang, Mian Zhang, Xi Chen, Maxime Bertrand, Amirhassan Shams-Ansari, Sethumadhavan Chandrasekhar, Peter Winzer, and Marko Lončar. Integrated lithium niobate electro-optic modulators operating at CMOS-compatible voltages. *Nature*, 562(7725):101–104, 2018.

[39] Yaowen Hu, Di Zhu, Shengyuan Lu, Xinrui Zhu, Yunxiang Song, Dylan Renaud, Daniel Assumpcao, Rebecca Cheng, C. J. Xin, and Matthew Yeh. Integrated electro-optics on thin-film lithium niobate. *Nature Reviews Physics*, pages 1–18, 2025.

[40] Feng Chen. Photonic guiding structures in lithium niobate crystals produced by energetic ion beams. *Journal of Applied Physics*, 106(8):081101, October 2009.

[41] Rongjin Zhuang, Jinze He, Yifan Qi, and Yang Li. High- Q Thin-Film Lithium Niobate Microrings Fabricated with Wet Etching. *Advanced Materials*, 35(3):2208113, January 2023.

[42] Inna Krasnokutska, Jean-Luc J. Tambasco, Xijun Li, and Alberto Peruzzo. Ultra-low loss photonic circuits in lithium niobate on insulator. *Optics Express*, 26(2):897–904, January 2018.

[43] G. Ulliac, V. Calero, A. Ndao, F. I. Baida, and M. P. Bernal. Argon plasma inductively coupled plasma reactive ion etching study for smooth sidewall thin film lithium niobate waveguide application. *Optical Materials*, 53:1–5, March 2016.

[44] H Hui, R Ricken, and W Sohler. Etching of Lithium Niobate: From Ridge Waveguides to Photonic Crystal Structures. 2008.

[45] Yifan Qi and Yang Li. Integrated lithium niobate photonics. *Nanophotonics*, 9(6):1287–1320, 2020.

[46] Mian Zhang, Cheng Wang, Rebecca Cheng, Amirhassan Shams-Ansari, and Marko Lončar. Monolithic ultra-high-Q lithium niobate microring resonator. *Optica*, 4(12):1536, December 2017.

[47] Xinrui Zhu, Yaowen Hu, Shengyuan Lu, Hana Warner, Xudong Li, Yunxiang Song, Letícia Magalhães, Amirhassan Shams-Ansari, Andrea Cordaro, Neil Sinclair, and others. Twenty-nine million intrinsic Q-factor monolithic microresonators on thin-film lithium niobate. *Photonics Research*, 12(8):A63–A68, 2024.

[48] Yan Gao, Yi Sun, Israel Rebolledo-Salgado, Raphaël Van Laer, Victor Torres-Company, and Jochen Schröder. Tightly-confined and long z-cut lithium niobate waveguide with ultralow-loss. *Laser & Photonics Reviews*, 19(21):e00042, 2025.

[49] Yan Gao, Fuchuan Lei, Marcello Girardi, Zhichao Ye, Raphaël Van Laer, Victor Torres-Company, and Jochen Schröder. Compact lithium niobate microring resonators in the ultrahigh q/v regime. *Opt. Lett.*, 48(15):3949–3952, Aug 2023.

[50] Fan Yang, Xiansong Fang, Xinyu Chen, Lixin Zhu, Fan Zhang, Zhangyuan Chen, and Yanping Li. Monolithic thin film lithium niobate electro-optic modulator with over 110 GHz bandwidth. *Chinese Optics Letters, Vol. 20, Issue 2, pp. 022502-*, February 2022.

[51] T. Vanackere, T. Vandekerckhove, L. Bogaert, M. Billet, S. Poelman, S. Cuyvers, J. Van Kerrebrouck, A. Moerman, O. Caytan, N. Singh, S. Lemey, G. Torfs, P. Ossieur, G. Roelkens, S. Clemmen, and B. Kuyken. Heterogeneous integration of a high-speed lithium niobate modulator on silicon nitride using micro-transfer printing. *APL Photonics*, 8(8):086102, August 2023.

[52] Lisa De Jaeger, Tom Vandekerckhove, Tom Reep, Stijn Poelman, Stéphane Clemmen, and Bart Kuyken. Compact low-voltage lithium niobate racetrack modulator on a silicon nitride platform through micro-transfer printing. *Optics Letters*, 50(16):4942, August 2025.

[53] Ying Tan, Shengpu Niu, Maximilien Billet, Nishant Singh, Margot Niels, Tom Vanackere, Joris Van Kerrebrouck, Gunther Roelkens, Bart Kuyken, and Dries Van Thourhout. Micro-transfer Printed Thin Film Lithium Niobate (TFLN)-on-Silicon Ring Modulator. *ACS Photonics*, 11(5):1920–1927, May 2024.

[54] Keith Powell, Xudong Li, Daniel Assumpcao, Letícia Magalhães, Neil Sinclair, and Marko Lončar. DC-stable electro-optic modulators using thin-film lithium tantalate. *Optics Express*, 32(25):44115, December 2024.

[55] Chengli Wang, Zihan Li, Johann Riemensberger, Grigory Lihachev, Mikhail Churaev, Wil Kao, Xinru Ji, Junyin Zhang, Terence Blesin, Alisa Davydova, Yang

Chen, Kai Huang, Xi Wang, Xin Ou, and Tobias J. Kippenberg. Lithium tantalate photonic integrated circuits for volume manufacturing. *Nature*, 629(8013):784–790, May 2024.

[56] Adnan Ghumro, Jack A. Smith, Loyd J. McKnight, and Michael J. Strain. Compact, tunable microring resonator on a lithium niobate platform using etchless fabrication methods. *Optics Continuum*, 5(3):800–810, March 2026.

[57] Zejie Yu, Xiang Xi, Jingwen Ma, Hon Ki Tsang, Chang-Ling Zou, and Xiankai Sun. Photonic integrated circuits with bound states in the continuum. *Optica*, 6(10):1342–1348, October 2019. Publisher: Optica Publishing Group.

[58] R. S. Weis and T. K. Gaylord. Lithium niobate: Summary of physical properties and crystal structure. *Applied Physics A Solids and Surfaces*, 37(4):191–203, August 1985.

[59] Robert W. Boyd. *Nonlinear Optics*. Academic Press, 3rd edition, 2008.

[60] Richard Jr Osgood and Xiang Meng. *Principles of photonic integrated circuits: materials, device physics, guided wave design*. Graduate texts in physics. Springer, Cham, Switzerland, 2021.

[61] Simone Sanna and Wolf Gero Schmidt. Lithium niobate X -cut, Y -cut, and Z -cut surfaces from *ab initio* theory. *Physical Review B*, 81(21):214116, June 2010.

[62] S.P. Denbaars. Gallium-nitride-based materials for blue to ultraviolet optoelectronics devices. *Proceedings of the IEEE*, 85(11):1740–1749, November 1997.

[63] Yixin Xiong, Mansura Sadek, and Rongming Chu. Recent advances in GaN-based power devices and integration. *Semiconductor Science and Technology*, 40(3):033002, February 2025.

[64] Lixia Zhao, Chang Liu, and Kaiyou Wang. Progress of GaN-Based Optoelectronic Devices Integrated with Optical Resonances. *Small*, 18(14):2106757, 2022. _eprint: https://onlinelibrary.wiley.com/doi/pdf/10.1002/smll.202106757.

[65] Jennifer Hite, Mark Twigg, Michael Mastro, Jaime Freitas, Jerry Meyer, Igor Vurgaftman, Shawn O'Connor, Nicholas Condon, Fritz Kub, Steven Bowman, and Charles Eddy. Development of periodically oriented gallium nitride for nonlinear optics [Invited]. *Optical Materials Express*, 2(9):1203–1208, September 2012.

[66] M. Welna, R. Kudrawiec, M. Motyka, R. Kucharski, M. Zajac, M. Rudziński, J. Misiewicz, R. Doradziński, and R. Dwiliński. Transparency of GaN substrates in the mid-infrared spectral range. *Crystal Research and Technology*, 47(3):347–350, 2012. _eprint: https://onlinelibrary.wiley.com/doi/pdf/10.1002/crat.201100443.

[67] X.-C. Long, R. A. Myers, S. R. J. Brueck, R. Ramer, K. Zheng, and S. D. Hersee. GaN linear electro-optic effect. *Applied Physics Letters*, 67(10):1349–1351, September 1995.

[68] Chuanliang Wang, Ahsan Ali, and Khadga Jung Karki. Multiphoton photocurrent in wide bandgap semiconductors for nonlinear optoelectronics: Comparison of GaP, GaN/InGaN, and SiC. *Applied Physics Letters*, 124(6):062101, February 2024.

[69] Hong Chen, Houqiang Fu, Xuanqi Huang, Xiaodong Zhang, Tsung-Han Yang, Jossue A. Montes, Izak Baranowski, and Yuji Zhao. Low loss GaN waveguides at the visible spectral wavelengths for integrated photonics applications. *Optics Express*, 25(25):31758–31773, December 2017.

[70] Yanzhen Zheng, Changzheng Sun, Bing Xiong, Lai Wang, Zhibiao Hao, Jian Wang, Yanjun Han, Hongtao Li, Jiadong Yu, and Yi Luo. Integrated gallium nitride nonlinear photonics. *Laser & Photonics Reviews*, 16(1):2100071, 2022.

[71] Jack A. Smith, Henry Francis, Gabriele Navickaite, and Michael J. Strain. SiN foundry platform for high performance visible light integrated photonics. *Optical Materials Express*, 13(2):458–468, February 2023. Publisher: Optica Publishing Group.

[72] David J. Moss, Roberto Morandotti, Alexander L. Gaeta, and Michal Lipson. New CMOS-compatible platforms based on silicon nitride and Hydex for nonlinear optics. *Nature Photonics*, 7(8):597–607, August 2013.

[73] Martin H. P. Pfeiffer, Arne Kordts, Victor Brasch, Michael Zervas, Michael Geiselmann, John D. Jost, and Tobias J. Kippenberg. Photonic Damascene process for integrated high-Q microresonator based nonlinear photonics. *Optica*, 3(1):20–25, January 2016.

[74] Chao Xiang, Warren Jin, and John E. Bowers. Silicon nitride passive and active photonic integrated circuits: trends and prospects. *Photonics Research*, 10(6):A82–A96, June 2022.

[75] Wesley D. Sacher, Jared C. Mikkelsen, Ying Huang, Jason C. C. Mak, Zheng Yong, Xianshu Luo, Yu Li, Patrick Dumais, Jia Jiang, Dominic Goodwill, Eric Bernier, Patrick Guo-Qiang Lo, and Joyce K. S. Poon. Monolithically Integrated Multilayer Silicon Nitride-on-Silicon Waveguide Platforms for 3-D Photonic Circuits and Devices. *Proceedings of the IEEE*, 106(12):2232–2245, December 2018.

[76] Chao Xiang and John E. Bowers. Building 3D integrated circuits with electronics and photonics. *Nature Electronics*, 7(6):422–424, June 2024.

[77] Majid Sodagar, Reza Pourabolghasem, Ali A. Eftekhar, and Ali Adibi. High-efficiency and wideband interlayer grating couplers in multilayer $Si/SiO_2/SiN$ platform for 3D integration of optical functionalities. *Optics Express*, 22(14):16767–16777, July 2014.

[78] Jin Yao, Xuezhe Zheng, Guoliang Li, Ivan Shubin, Hiren Thacker, Ying Luo, Kannan Raj, John E. Cunningham, and Ashok V. Krishnamoorthy. Grating-coupler based low-loss optical interlayer coupling. In *8th IEEE International Conference on Group IV Photonics*, pages 383–385, September 2011. ISSN: 1949-209X.

[79] Wesley D. Sacher, Ying Huang, Guo-Qiang Lo, and Joyce K. S. Poon. Multilayer Silicon Nitride-on-Silicon Integrated Photonic Platforms and Devices. *Journal of Lightwave Technology*, 33(4):901–910, February 2015.

[80] Kuanping Shang, Shibnath Pathak, Binbin Guan, Guangyao Liu, and S. J. B. Yoo. Low-loss compact multilayer silicon nitride platform for 3D photonic integrated circuits. *Optics Express*, 23(16):21334–21342, August 2015.

[81] Kuanping Shang, Shibnath Pathak, Guangyao Liu, Shaoqi Feng, Siwei Li, Weicheng Lai, and S. J. B. Yoo. Silicon nitride tri-layer vertical Y-junction and 3D couplers with arbitrary splitting ratio for photonic integrated circuits. *Optics Express*, 25(9):10474–10483, May 2017.

[82] Jhonattan C. Ramirez, Juliana N. Schianti, Maria G. Almeida, Aristides Pavani, Roberto R. Panepucci, Hugo E. Hernandez-Figueroa, and Lucas H. Gabrielli. Low-loss modified SU-8 waveguides by direct laser writing at 405 nm. *Optical Materials Express*, 7(7):2651–2659, July 2017.

[83] Seiji Sowa, Wataru Watanabe, Takayuki Tamaki, Junji Nishii, and Kazuyoshi Itoh. Symmetric waveguides in poly(methyl methacrylate) fabricated by femtosecond laser pulses. *Optics Express*, 14(1):291–297, January 2006.

[84] M. Ferriol, A. Gentilhomme, M. Cochez, N. Oget, and J. L. Mieloszynski. Thermal degradation of poly(methyl methacrylate) (PMMA): modelling of DTG and TG curves. *Polymer Degradation and Stability*, 79(2):271–281, January 2003.

[85] Jay W. Reddy, Maya Lassiter, and Maysamreza Chamanzar. Parylene photonics: a flexible, broadband optical waveguide platform with integrated micromirrors for biointerfaces. *Microsystems & Nanoengineering*, 6(1):85, September 2020.

[86] E. Mengi and Yu-Chong Tai. Parylene etching techniques for microfluidics and biomems. In *18th IEEE International Conference on Micro Electro Mechanical Systems, 2005. MEMS 2005.*, pages 568–571, Miami Beach, FL, USA, 2005. IEEE.

[87] Maria Nordström, Dan A. Zauner, Anja Boisen, and Jörg Hübner. Monolithic single mode SU-8 waveguides for integrated optics. In *Microfluidics, BioMEMS, and Medical Microsystems IV*, volume 6112, page 43. SPIE, January 2006.

[88] Maria Nordström, Dan A. Zauner, Anja Boisen, and Jörg Hübner. Single-mode waveguides with su-8 polymer core and cladding for moems applications. *J. Lightwave Technol.*, 25(5):1284–1289, May 2007.

[89] Ross Cassells, Jack A. Smith, Changyu Hu, Sean P. Bommer, Benoit Guilhabert, Martin D. Dawson, and Michael J. Strain. Planar waveguide to vertical mode couplers covering the visible to ir spectral range. *Opt. Express*, 32(22):38128–38135, Oct 2024.

[90] Andreas Boes, Bill Corcoran, Lin Chang, John Bowers, and Arnan Mitchell. Status and Potential of Lithium Niobate on Insulator (LNOI) for Photonic Integrated Circuits. *Laser & Photonics Reviews*, 12(4):1700256, April 2018.

[91] Abu Naim R. Ahmed, Shouyuan Shi, Mathew Zablocki, Peng Yao, and Dennis W. Prather. Tunable hybrid silicon nitride and thin-film lithium niobate electro-optic microresonator. *Optics Letters*, 44(3):618, February 2019.

[92] Shilei Jin, Longtao Xu, Haihua Zhang, and Yifei Li. $LiNbO_3$ Thin-Film Modulators Using Silicon Nitride Surface Ridge Waveguides. *IEEE Photonics Technology Letters*, 28(7):736–739, April 2016.

[93] Ashutosh Rao, Aniket Patil, Payam Rabiei, Amirmahdi Honardoost, Richard DeSalvo, Arthur Paolella, and Sasan Fathpour. High-performance and linear thin-film lithium niobate Mach–Zehnder modulators on silicon up to 50 GHz. *Optics Letters*, 41(24):5700, December 2016.

[94] Abu Naim R. Ahmed, Shouyuan Shi, Andrew J. Mercante, and Dennis W. Prather. High-performance racetrack resonator in silicon nitride - thin film lithium niobate hybrid platform. *Optics Express*, 27(21):30741, October 2019.

[95] Abu Naim R. Ahmed, Sean Nelan, Shouyuan Shi, Peng Yao, Andrew Mercante, and Dennis W. Prather. Subvolt electro-optical modulator on thin-film lithium niobate and silicon nitride hybrid platform. *Optics Letters*, 45(5):1112, March 2020.

[96] Yiwen Wang, Zhihua Chen, Lutong Cai, Yunpeng Jiang, Houbin Zhu, and Hui Hu. Amorphous silicon-lithium niobate thin film strip-loaded waveguides. *Optical Materials Express*, 7(11):4018, November 2017.

[97] Liang Cao, Abdelsalam Aboketaf, Zihao Wang, and Stefan Preble. Hybrid amorphous silicon (a-Si:H)–LiNbO3 electro-optic modulator. *Optics Communications*, 330:40–44, November 2014.

[98] Shuang Li, Lutong Cai, Yiwen Wang, Yunpeng Jiang, and Hui Hu. Waveguides consisting of single-crystal lithium niobate thin film and oxidized titanium stripe. *Optics Express*, 23(19):24212, September 2015.

[99] Tiening Jin, Junchao Zhou, and Pao Tai Lin. Mid-Infrared Electro-Optical Modulation Using Monolithically Integrated Titanium Dioxide on Lithium Niobate Optical Waveguides. *Scientific Reports*, 9(1):15130, October 2019.

[100] Ashutosh Rao, Aniket Patil, Jeff Chiles, Marcin Malinowski, Spencer Novak, Kathleen Richardson, Payam Rabiei, and Sasan Fathpour. Heterogeneous microring and Mach-Zehnder modulators based on lithium niobate and chalcogenide glasses on silicon. *Optics Express*, 23(17):22746, August 2015.

[101] E. A. J. Marcatili. Dielectric Rectangular Waveguide and Directional Coupler for Integrated Optics. *Bell System Technical Journal*, 48(7):2071–2102, September 1969.

[102] Chang-Ling Zou, Jin-Ming Cui, Fang-Wen Sun, Xiao Xiong, Xu-Bo Zou, Zheng-Fu Han, and Guang-Can Guo. Guiding light through optical bound states in the continuum for ultrahigh- Q microresonators. *Laser & Photonics Reviews*, 9(1):114–119, January 2015.

[103] Zejie Yu, Yeyu Tong, Hon Ki Tsang, and Xiankai Sun. High-dimensional communication on etchless lithium niobate platform with photonic bound states in the continuum. *Nature Communications*, 11(1):2602, May 2020.

[104] J. von Neumann and E. Wigner. On some peculiar discrete eigenvalues. *Physikalische Zeitschrift*, 30:465–467, 1929.

[105] Shaimaa I. Azzam and Alexander V. Kildishev. Photonic Bound States in the Continuum: From Basics to Applications. *Advanced Optical Materials*, 9(1):2001469, 2021. _eprint: https://advanced.onlinelibrary.wiley.com/doi/pdf/10.1002/adom.202001469.

[106] Zejie Yu and Xiankai Sun. Acousto-optic modulation of photonic bound state in the continuum. *Light: Science & Applications*, 9(1):1, January 2020.

[107] Jiří Petráček, Vladimír Kuzmiak, Jiří Čtyroký, and Ivan Richter. Guiding light through quasi-TE modes embedded in the radiation continuum. *Optics Letters*, 48(13):3463, July 2023. Publisher: Optica Publishing Group.

[108] Kyunghun Han, Thomas W. LeBrun, and Vladimir A. Aksyuk. Bound-state-in-continuum guided modes in a multilayer electro-optically active photonic integrated circuit platform. *Optica*, 11(5):706, May 2024. Publisher: Optica Publishing Group.

[109] Flexcompute. Tidy3d: Fast, modern photonic simulations. `https://www.flexcompute.com/tidy3d/`. Accessed: 2026-02-12.

[110] Zhaoming Zhu and Thomas Brown. Full-vectorial finite-difference analysis of microstructured optical fibers. *Optics Express*, 10(17):853, August 2002.

[111] Allen Taflove, Susan C. Hagness, and M. Piket-May. *Computational Electromagnetics: The Finite-Difference Time-Domain Method*. Academic Press, 2004. Chapter 9, pp. 629–670.

[112] David E. Zelmon, David L. Small, and Dieter Jundt. Infrared corrected Sellmeier coefficients for congruently grown lithium niobate and 5 mol. % magnesium ox-

ide–doped lithium niobate. *JOSA B, Vol. 14, Issue 12, pp. 3319-3322*, December 1997.

[113] Amnon Yariv. *Optical Electronics*. Saunders College Publishing, 1991.

[114] Dan Yi, Wen Zhou, Yaojing Zhang, and Hon Ki Tsang. Inverse design of multi-band and wideband waveguide crossings. *Optics Letters*, 46(4):884–887, February 2021. Publisher: Optica Publishing Group.

[115] Mack Johnson, Mark G. Thompson, and Döndü Sahin. Low-loss, low-crosstalk waveguide crossing for scalable integrated silicon photonics applications. *Optics Express*, 28(9):12498–12507, April 2020. Publisher: Optica Publishing Group.

[116] Huimin Yang, Pengfei Zheng, Guohua Hu, Ruohu Zhang, Binfeng Yun, and Yiping Cui. A broadband, low-crosstalk and low polarization dependent silicon nitride waveguide crossing based on the multimode-interference. *Optics Communications*, 450:28–33, November 2019.

[117] Haijie Zuo, Shaoliang Yu, Tian Gu, and Juejun Hu. Low loss, flexible single-mode polymer photonics. *Optics Express*, 27(8):11152–11159, April 2019. Publisher: Optica Publishing Group.

[118] Lin Han, Xiaoke Ruan, Weijie Tang, and Tao Chu. Ultralow-loss waveguide crossing for photonic integrated circuits by using inverted tapers. *Optics Express*, 30(5):6738–6745, February 2022. Publisher: Optica Publishing Group.

[119] Sailong Wu, Simei Mao, Lidan Zhou, Lin Liu, Yujie Chen, Xin Mu, Lirong Cheng, Zhenmin Chen, Xin Tu, and H. Y. Fu. A compact and polarization-insensitive silicon waveguide crossing based on subwavelength grating MMI couplers. *Optics Express*, 28(19):27268–27276, September 2020. Publisher: Optica Publishing Group.

[120] Yikun Chen, Ke Zhang, Hanke Feng, Wenzhao Sun, and Cheng Wang. Design and resonator-assisted characterization of high-performance lithium niobate

waveguide crossings. *Optics Letters*, 48(9):2218–2221, May 2023. Publisher: Optica Publishing Group.

[121] Amir H. Atabaki, Sajjad Moazeni, Fabio Pavanello, Hayk Gevorgyan, Jelena Notaros, Luca Alloatti, Mark T. Wade, Chen Sun, Seth A. Kruger, Huaiyu Meng, Kenaish Al Qubaisi, Imbert Wang, Bohan Zhang, Anatol Khilo, Christopher V. Baiocco, Miloš A. Popović, Vladimir M. Stojanović, and Rajeev J. Ram. Integrating photonics with silicon nanoelectronics for the next generation of systems on a chip. *Nature*, 556(7701):349–354, April 2018.

[122] Mercedes Gimeno-Segovia, Hugo Cable, Gabriel J Mendoza, Pete Shadbolt, Joshua W Silverstone, Jacques Carolan, Mark G Thompson, Jeremy L O'Brien, and Terry Rudolph. Relative multiplexing for minimising switching in linear-optical quantum computing. *New Journal of Physics*, 19(6):063013, June 2017.

[123] William A. Zortman, Douglas C. Trotter, and Michael R. Watts. Silicon photonics manufacturing. *Optics Express*, 18(23):23598, November 2010.

[124] Jifeng Liu, Mark Beals, Andrew Pomerene, Sarah Bernardis, Rong Sun, Jing Cheng, Lionel C. Kimerling, and Jurgen Michel. Waveguide-integrated, ultralow-energy GeSi electro-absorption modulators. *Nature Photonics*, 2(7):433–437, July 2008.

[125] D. A. B. Miller, D. S. Chemla, T. C. Damen, A. C. Gossard, W. Wiegmann, T. H. Wood, and C. A. Burrus. Band-Edge Electroabsorption in Quantum Well Structures: The Quantum-Confined Stark Effect. *Physical Review Letters*, 53(22):2173–2176, November 1984.

[126] Yonghao Cui, Ke Liu, Duncan L. MacFarlane, and Jeong-Bong Lee. Thermo-optically tunable silicon photonic crystal light modulator. *Optics Letters*, 35(21):3613, November 2010.

[127] Yiwei Xie, Yaocheng Shi, Liu Liu, Jianwei Wang, Rubana Priti, Guowu Zhang, Odile Liboiron-Ladouceur, and Daoxin Dai. Thermally-Reconfigurable Silicon

Photonic Devices and Circuits. *IEEE Journal of Selected Topics in Quantum Electronics*, 26(5):1–20, September 2020.

[128] K. Hassan, J.-C. Weeber, L. Markey, A. Dereux, A. Pitilakis, O. Tsilipakos, and E. E. Kriezis. Thermo-optic plasmo-photonic mode interference switches based on dielectric loaded waveguides. *Applied Physics Letters*, 99(24):241110, December 2011.

[129] D. Kalavrouziotis, S. Papaioannou, G. Giannoulis, D. Apostolopoulos, K. Hassan, L. Markey, J.-C. Weeber, A. Dereux, A. Kumar, S. I. Bozhevolnyi, M. Baus, M. Karl, T. Tekin, O. Tsilipakos, A. Pitilakis, E. E. Kriezis, H. Avramopoulos, K. Vyrsokinos, and N. Pleros. 048Tb/s (12x40Gb/s) WDM transmission and high-quality thermo-optic switching in dielectric loaded plasmonics. *Optics Express*, 20(7):7655, March 2012.

[130] Zhibo Li, Jack A. Smith, Mark Scullion, Nils Kolja Wessling, Loyd J. McKnight, and Martin D. Dawson. Photonic integration of lithium niobate micro-ring resonators onto silicon nitride waveguide chips by transfer-printing. *Optical Materials Express*, 12(11):4375, November 2022.

[131] Li Chen, Michael G. Wood, and Ronald M. Reano. 125 pm/V hybrid silicon and lithium niobate optical microring resonator with integrated electrodes. *Optics Express*, 21(22):27003, November 2013.

[132] Li Chen, Qiang Xu, Michael G. Wood, and Ronald M. Reano. Hybrid silicon and lithium niobate electro-optical ring modulator. *Optica*, 1(2):112, August 2014.

[133] Andrew J. Mercante, Shouyuan Shi, Peng Yao, Linli Xie, Robert M. Weikle, and Dennis W. Prather. Thin film lithium niobate electro-optic modulator with terahertz operating bandwidth. *Optics Express*, 26(11):14810, May 2018.

[134] Zejie Yu, Xiang Xi, Jingwen Ma, Hon Ki Tsang, Chang-Ling Zou, and Xiankai Sun. Photonic integrated circuits with bound states in the continuum: erratum. *Optica*, 9(7):683, July 2022.

[135] Leong Yew Wing, Zhang ShiYun, Christopher Pang, Mohammad Hazren, Sunil Arya Kumar, and Wong Chee Chung. Optimization studies of lift-off methods and its application in electrochemical biosensors. In *2014 IEEE 16th Electronics Packaging Technology Conference (EPTC)*, pages 768–773, Singapore, December 2014. IEEE.

[136] William M. Abbott, Christopher P. Murray, Chuan Zhong, Christopher Smith, Cormac McGuinness, Ehsan Rezvani, Clive Downing, Dermot Daly, Amanda K. Petford-Long, Frank Bello, David McCloskey, and John F. Donegan. Less is More: Improved Thermal Stability and Plasmonic Response in Au Films via the Use of SubNanometer Ti Adhesion Layers. *ACS Applied Materials & Interfaces*, 11(7):7607–7614, February 2019.

[137] Jeffrey Holzgrafe, Eric Puma, Rebecca Cheng, Hana Warner, Amirhassan Shams-Ansari, Raji Shankar, and Marko Lončar. Relaxation of the electro-optic response in thin-film lithium niobate modulators. *Opt. Express*, 32(3):3619–3631, Jan 2024.

[138] Mengyue Xu, Mingbo He, Hongguang Zhang, Jian Jian, Ying Pan, Xiaoyue Liu, Lifeng Chen, Xiangyu Meng, Hui Chen, Zhaohui Li, Xi Xiao, Shaohua Yu, Siyuan Yu, and Xinlun Cai. High-performance coherent optical modulators based on thin-film lithium niobate platform. *Nature Communications*, 11(1):3911, August 2020. Publisher: Nature Publishing Group.

[139] Viphretuo Mere, Forrest Valdez, Xiaoxi Wang, and Shayan Mookherjea. A modular fabrication process for thin-film lithium niobate modulators with silicon photonics. *Journal of Physics: Photonics*, 4(2):024001, April 2022.

[140] Alessandro Prencipe and Katia Gallo. Electro- and Thermo-Optics Response of X-Cut Thin Film $LiNbO_3$ Waveguides. *IEEE Journal of Quantum Electronics*, 59(3):1–8, June 2023.

[141] Shihao Sun, Mingbo He, Mengyue Xu, Shengqian Gao, Ziyan Chen, Xian Zhang, Ziliang Ruan, Xiong Wu, Lidan Zhou, Lin Liu, Chao Lu, Changjian Guo, Liu Liu, Siyuan Yu, and Xinlun Cai. Bias-drift-free Mach–Zehnder modulators based

on a heterogeneous silicon and lithium niobate platform. *Photonics Research*, 8(12):1958, December 2020.

[142] Mengke Wang, Junhui Li, Hao Yao, Xuepeng Li, Jieyun Wu, Kin Seng Chiang, and Kaixin Chen. Thin-film lithium-niobate modulator with a combined passive bias and thermo-optic bias. *Optics Express*, 30(22):39706, October 2022.

[143] Nicholas C. Harris, Yangjin Ma, Jacob Mower, Tom Baehr-Jones, Dirk Englund, Michael Hochberg, and Christophe Galland. Efficient, compact and low loss thermo-optic phase shifter in silicon. *Optics Express*, 22(9):10487, May 2014.

[144] Po Dong, Young-Kai Chen, Guang-Hua Duan, and David T. Neilson. Silicon photonic devices and integrated circuits. *Nanophotonics*, 3(4-5):215–228, August 2014. Publisher: De Gruyter.

[145] Seunghyeb Ban, Hoon Yi, Jaejin Park, Yunuo Huang, Ki Jun Yu, and Woon-Hong Yeo. Advances in Photonic Materials and Integrated Devices for Smart and Digital Healthcare: Bridging the Gap Between Materials and Systems. *Advanced Materials*, 37(49):2416899, 2025. _eprint: https://advanced.onlinelibrary.wiley.com/doi/pdf/10.1002/adma.202416899.

[146] Renjie Li, Yuanhao Gong, Hai Huang, Yuze Zhou, Sixuan Mao, Zhijian Wei, and Zhaoyu Zhang. Photonics for Neuromorphic Computing: Fundamentals, Devices, and Opportunities. *Advanced Materials*, 37(2):2312825, 2025. _eprint: https://advanced.onlinelibrary.wiley.com/doi/pdf/10.1002/adma.202312825.

[147] Zian Xiao, Weixin Liu, Siyu Xu, Jingkai Zhou, Zhihao Ren, and Chengkuo Lee. Recent Progress in Silicon-Based Photonic Integrated Circuits and Emerging Applications. *Advanced Optical Materials*, 11(20):2301028, 2023. _eprint: https://advanced.onlinelibrary.wiley.com/doi/pdf/10.1002/adom.202301028.

[148] Jianwei Wang, Fabio Sciarrino, Anthony Laing, and Mark G. Thompson. Integrated photonic quantum technologies. *Nature Photonics*, 14(5):273–284, May 2020. Publisher: Nature Publishing Group.

[149] Andreas Boes, Michael Strain, Lin Chang, and Nima Nader. Hybrid and heterogeneous integration in photonics: From physics to device applications. *Applied Physics Letters*, 127(13), September 2025. Publisher: AIP Publishing.

[150] Matthew W. Puckett, Kaikai Liu, Nitesh Chauhan, Qiancheng Zhao, Naijun Jin, Haotian Cheng, Jianfeng Wu, Ryan O. Behunin, Peter T. Rakich, Karl D. Nelson, and Daniel J. Blumenthal. 422 Million intrinsic quality factor planar integrated all-waveguide resonator with sub-MHz linewidth. *Nature Communications*, 12(1):934, February 2021. Publisher: Nature Publishing Group.

[151] Junqiu Liu, Guanhao Huang, Rui Ning Wang, Jijun He, Arslan S. Raja, Tianyi Liu, Nils J. Engelsen, and Tobias J. Kippenberg. High-yield, wafer-scale fabrication of ultralow-loss, dispersion-engineered silicon nitride photonic circuits. *Nature Communications*, 12(1):2236, April 2021. Publisher: Nature Publishing Group.

[152] Goran Z. Mashanovich, Milan M. Milošević, Milos Nedeljkovic, Nathan Owens, Boqian Xiong, Ee Jin Teo, and Youfang Hu. Low loss silicon waveguides for the mid-infrared. *Optics Express*, 19(8):7112–7119, April 2011. Publisher: Optica Publishing Group.

[153] Po Dong, Wei Qian, Shirong Liao, Hong Liang, Cheng-Chih Kung, Ning-Ning Feng, Roshanak Shafiiha, Joan Fong, Dazeng Feng, Ashok V. Krishnamoorthy, and Mehdi Asghari. Low loss shallow-ridge silicon waveguides. *Optics Express*, 18(14):14474–14479, July 2010. Publisher: Optica Publishing Group.

[154] G. Roelkens, L. Liu, D. Liang, R. Jones, A. Fang, B. Koch, and J. Bowers. III-V/silicon photonics for on-chip and intra-chip optical interconnects. *Laser & Photonics Reviews*, 4(6):751–779, 2010. _eprint: https://onlinelibrary.wiley.com/doi/pdf/10.1002/lpor.200900033.

[155] Hyundai Park, Alexander W. Fang, Richard Jones, Oded Cohen, Omri Raday, Matthew N. Sysak, Mario J. Paniccia, and John E. Bowers. A hybrid AlGaInAs-

silicon evanescent waveguide photodetector. *Optics Express*, 15(10):6044–6052, May 2007. Publisher: Optica Publishing Group.

[156] Alexander W. Bruch, Chi Xiong, Benjamin Leung, Menno Poot, Jung Han, and Hong X. Tang. Broadband nanophotonic waveguides and resonators based on epitaxial GaN thin films. *Applied Physics Letters*, 107(14):141113, October 2015.

[157] H Amano, Y Baines, E Beam, Matteo Borga, T Bouchet, Paul R Chalker, M Charles, Kevin J Chen, Nadim Chowdhury, Rongming Chu, Carlo De Santi, Maria Merlyne De Souza, Stefaan Decoutere, L Di Cioccio, Bernd Eckardt, Takashi Egawa, P Fay, Joseph J Freedsman, L Guido, Oliver Häberlen, Geoff Haynes, Thomas Heckel, Dilini Hemakumara, Peter Houston, Jie Hu, Mengyuan Hua, Qingyun Huang, Alex Huang, Sheng Jiang, H Kawai, Dan Kinzer, Martin Kuball, Ashwani Kumar, Kean Boon Lee, Xu Li, Denis Marcon, Martin März, R McCarthy, Gaudenzio Meneghesso, Matteo Meneghini, E Morvan, A Nakajima, E M S Narayanan, Stephen Oliver, Tomás Palacios, Daniel Piedra, M Plissonnier, R Reddy, Min Sun, Iain Thayne, A Torres, Nicola Trivellin, V Unni, Michael J Uren, Marleen Van Hove, David J Wallis, J Wang, J Xie, S Yagi, Shu Yang, C Youtsey, Ruiyang Yu, Enrico Zanoni, Stefan Zeltner, and Yuhao Zhang. The 2018 GaN power electronics roadmap. *Journal of Physics D: Applied Physics*, 51(16):163001, March 2018.

[158] Benoit Guilhabert, Antonio Hurtado, Dimitars Jevtics, Qian Gao, Hark Hoe Tan, Chennupati Jagadish, and Martin D. Dawson. Transfer Printing of Semiconductor Nanowires with Lasing Emission for Controllable Nanophotonic Device Fabrication. *ACS Nano*, 10(4):3951–3958, April 2016.

[159] Sean P. Bommer, Christopher Panuski, Benoit Guilhabert, Zhongyi Xia, Jack A. Smith, Martin D. Dawson, Dirk Englund, and Michael J. Strain. Transfer printing micro-assembly of silicon photonic crystal cavity arrays: beating the fabrication tolerance limit. *Nature Communications*, 16(1):5994, July 2025.

[160] Benoit Guilhabert, Sean P. Bommer, Nils K. Wessling, Dimitars Jevtics, Jack A. Smith, Zhongyi Xia, Saptarsi Ghosh, Menno Kappers, Ian M. Watson, Rachel A. Oliver, Martin D. Dawson, and Michael J. Strain. Advanced transfer printing with in-situ optical monitoring for the integration of micron-scale devices. *IEEE Journal of Selected Topics in Quantum Electronics*, pages 1–12, 2022.

[161] Matthew A. Meitl, Zheng-Tao Zhu, Vipan Kumar, Keon Jae Lee, Xue Feng, Yonggang Y. Huang, Ilesanmi Adesida, Ralph G. Nuzzo, and John A. Rogers. Transfer printing by kinetic control of adhesion to an elastomeric stamp. *Nature Materials*, 5(1):33–38, January 2006. Publisher: Nature Publishing Group.

[162] Xue Feng, Matthew A. Meitl, Audrey M. Bowen, Yonggang Huang, Ralph G. Nuzzo, and John A. Rogers. Competing Fracture in Kinetically Controlled Transfer Printing. *Langmuir*, 23(25):12555–12560, December 2007. Publisher: American Chemical Society.

[163] Andrew Carlson, Audrey M. Bowen, Yonggang Huang, Ralph G. Nuzzo, and John A. Rogers. Transfer Printing Techniques for Materials Assembly and Micro/Nanodevice Fabrication. *Advanced Materials*, 24(39):5284–5318, 2012. _eprint: https://advanced.onlinelibrary.wiley.com/doi/pdf/10.1002/adma.201201386.

[164] D. Celo, R. Vandusen, T. Smy, J. Albert, N. G. Tarr, and P. D. Waldron. Low temperature plasma etching for Si3N4 waveguide applications. *Journal of Vacuum Science & Technology A*, 26(2):253–258, January 2008.

[165] Nils Kolja Wessling, Saptarsi Ghosh, Benoit Guilhabert, Menno Kappers, Alexander M. Hinz, Miles Toon, Rachel A. Oliver, Martin D. Dawson, and Michael J. Strain. Fabrication and transfer printing based integration of free-standing GaN membrane micro-lenses onto semiconductor chips. *Optical Materials Express*, 12(12):4606, December 2022.

[166] Zeinab Shaban, Zhi Li, Brendan Roycroft, Mehrdad Saei, Tanmay Mondal, and Brian Corbett. Transfer Printing of Roughened GaN-Based

Light-Emitting Diodes into Reflective Trenches for Visible Light Communication. *Advanced Photonics Research*, 3(8):2100312, 2022. _eprint: https://advanced.onlinelibrary.wiley.com/doi/pdf/10.1002/adpr.202100312.

[167] J A Smith. Hybrid integration of chipscale photonic devices using accurate transfer printing methods. 2022.

[168] A J Trindade, B Guilhabert, E Y Xie, R Ferreira, J J D McKendry, D Zhu, N Laurand, E Gu, D J Wallis, I M Watson, C J Humphreys, and M D Dawson. Heterogeneous integration of gallium nitride light-emitting diodes on diamond and silica by transfer printing. 2015.

[169] Yu Xia, Yuhao Huang, Yuemin Li, Jie Wang, Yunqi Fu, Yaoran Huang, Hongjie Liang, Hao Fang, Zheng Li, Mingfei Liu, Yitian Tong, Di Yu, and Chao Xiang. Scalable 3D silicon nitride photonic interposer for high-density optical interconnects, 2026. Version Number: 1.

[170] Nicolás Sherwood-Droz and Michal Lipson. Scalable 3D dense integration of photonics on bulk silicon. *Optics Express*, 19(18):17758–17765, August 2011.

[171] Aleksandr Biberman, Kyle Preston, Gilbert Hendry, Nicolás Sherwood-Droz, Johnnie Chan, Jacob S. Levy, Michal Lipson, and Keren Bergman. Photonic network-on-chip architectures using multilayer deposited silicon materials for high-performance chip multiprocessors. *J. Emerg. Technol. Comput. Syst.*, 7(2):7:1–7:25, July 2011.

[172] Takaaki Ishigure, Sho Yoshida, Kazuki Yasuhara, and Daisuke Suganuma. Low-loss single-modelow polymer optical waveguide at 1550-nm wavelength compatible with silicon photonics. In *2015 IEEE 65th Electronic Components and Technology Conference (ECTC)*, pages 768–774, May 2015. ISSN: 2377-5726.

[173] E. a. J. Marcatili. Bends in Optical Dielectric Guides. *Bell System Technical Journal*, 48(7):2103–2132, 1969. _eprint: https://onlinelibrary.wiley.com/doi/pdf/10.1002/j.1538-7305.1969.tb01167.x.

[174] Xu Liu, Lin Ma, Yijun Yu, Qiancheng Yu, Jinhua Wu, and Zuyuan He. Hybrid Polymer Waveguide With Large Refractive Index Contrast for High-Density Optical Interconnects. *IEEE Photonics Technology Letters*, 37(3):125–128, February 2025.

[175] Sean Molesky, Zin Lin, Alexander Y. Piggott, Weiliang Jin, Jelena Vucković, and Alejandro W. Rodriguez. Inverse design in nanophotonics. *Nature Photonics*, 12(11):659–670, November 2018.

[176] Louise Schul, Sydney Mason, Sungjun Eun, Geun Ho Ahn, and Jelena Vučković. Inverse design for scalable photonic systems. *Nature Reviews Materials*, pages 1–11, April 2026.

[177] Julian L. Pita Ruiz, Narges Dalvand, and Michaël Ménard. Integrated silicon nitride devices via inverse design. *Nature Communications*, 16(1):9307, October 2025.

[178] Alexander Y. Piggott, Eric Y. Ma, Logan Su, Geun Ho Ahn, Neil V. Sapra, Dries Vercruysse, Andrew M. Netherton, Akhilesh S. P. Khope, John E. Bowers, and Jelena Vučković. Inverse-Designed Photonics for Semiconductor Foundries. *ACS Photonics*, 7(3):569–575, March 2020.

[179] Yuting Zhou, Feiyu Jiao, Pei Zeng, Yansong Du, Yuxuan Liu, Simeng Li, Chonghao Zhang, Jingtong Yao, Yufeng Wang, Jian Song, and Xun Guan. Inverse Designed SU8-on-Insulator Platform for Polymer Waveguide Photonics. *IEEE Photonics Technology Letters*, 37(21):1217–1220, November 2025.

[180] Bo Yang, Liu Yang, Rui Hu, Zhen Sheng, Daoxin Dai, Qingkun Liu, and Sailing He. Fabrication and Characterization of Small Optical Ridge Waveguides Based on SU-8 Polymer. *Journal of Lightwave Technology, Vol. 27, Issue 18, pp. 4091-4096*, September 2009.

[181] Ross Cassells, Jack A. Smith, Changyu Hu, Sean P. Bommer, Benoit Guilhabert, Martin D. Dawson, and Michael J. Strain. Planar waveguide to vertical mode

couplers covering the visible to IR spectral range. *Optics Express*, 32(22):38128–38135, October 2024.

[182] J.s. Jensen and O. Sigmund. Topology optimization for nano-photonics. *Laser & Photonics Reviews*, 5(2):308–321, 2011. _eprint: https://onlinelibrary.wiley.com/doi/pdf/10.1002/lpor.201000014.

[183] Rasmus E. Christiansen and Ole Sigmund. Inverse design in photonics by topology optimization: tutorial. *JOSA B*, 38(2):496–509, February 2021.

[184] Fengwen Wang, Boyan Stefanov Lazarov, and Ole Sigmund. On projection methods, convergence and robust formulations in topology optimization. *Structural and Multidisciplinary Optimization*, 43(6):767–784, June 2011.

[185] Mohamed A. Swillam, Mohamed H. Bakr, and Xun Li. Accurate sensitivity analysis of photonic devices that exploit the finite-difference time-domain central adjoint variable method. *Applied Optics*, 46(9):1492–1499, March 2007.

[186] Christopher M. Lalau-Keraly, Samarth Bhargava, Owen D. Miller, and Eli Yablonovitch. Adjoint shape optimization applied to electromagnetic design. *Optics Express*, 21(18):21693–21701, September 2013.